UNCLASSIFIED
SECURITY CLASSIFICATION OF THIS PAGE (When Data Entered)

DTIC FILE COPY

①

AD-A196 297

REPORT DOCUMENTATION PAGE

READ INSTRUCTIONS BEFORE COMPLETING FORM

1. REPORT NUMBER AFIT/CI/NR 88- 140	2. GOVT ACCESSION NO.
	3. RECIPIENT'S CATALOG NUMBER
TITLE (and Subtitle) THE ASPECT RATIO DEPENDENCE OF THE ATTRACTOR DIMENSION IN TAYLOR-COUETTE FLOW	5. TYPE OF REPORT & PERIOD COVERED PHD ~~MS~~ THESIS
	6. PERFORMING ORG. REPORT NUMBER
AUTHOR(s) DONALD ALLEN HIRST	8. CONTRACT OR GRANT NUMBER(s)
PERFORMING ORGANIZATION NAME AND ADDRESS AFIT STUDENT AT: UNIVERSITY OF TEXAS - AUSTIN	10. PROGRAM ELEMENT, PROJECT, TASK AREA & WORK UNIT NUMBERS
1. CONTROLLING OFFICE NAME AND ADDRESS	12. REPORT DATE 1988
	13. NUMBER OF PAGES 195
14. MONITORING AGENCY NAME & ADDRESS(if different from Controlling Office) AFIT/NR Wright-Patterson AFB OH 45433-6583	15. SECURITY CLASS. (of this report) UNCLASSIFIED
	15a. DECLASSIFICATION/DOWNGRADING SCHEDULE

16. DISTRIBUTION STATEMENT (of this Report)

DISTRIBUTED UNLIMITED: APPROVED FOR PUBLIC RELEASE

DTIC
ELECTE
AUG 0 3 1988
S D
D

17. DISTRIBUTION STATEMENT (of the abstract entered in Block 20, if different from Report)

SAME AS REPORT

18. SUPPLEMENTARY NOTES

Approved for Public Release: IAW AFR 190-1
LYNN E. WOLAVER Lynn Wolaver 21 July 88
Dean for Research and Professional Development
Air Force Institute of Technology
Wright-Patterson AFB OH 45433-6583

19. KEY WORDS (Continue on reverse side if necessary and identify by block number)

20. ABSTRACT (Continue on reverse side if necessary and identify by block number)

ATTACHED

88

DD FORM 1 JAN 73 1473 EDITION OF 1 NOV 65 IS OBSOLETE

UNCLASSIFIED
SECURITY CLASSIFICATION OF THIS PAGE (When Data Entered)

THE ASPECT RATIO DEPENDENCE OF THE ATTRACTOR DIMENSION IN TAYLOR-COUETTE FLOW

Donald Allen Hirst, Ph. D.
Captain, United States Air Force
The University of Texas at Austin, 1987
195 pages
Supervising Professor: Harry L. Swinney

An investigation of the aspect ratio dependence of the attractor dimension in flow between concentric cylinders (Taylor-Couette flow) was performed with the inner cylinder rotating and the outer cylinder at rest. Phase space attractors were reconstructed from experimental velocity data by time delay methods and the attractor dimension calculated by both the Grassberger-Procaccia and Badii-Politi algorithms. The aspect ratio was varied between 19.9 and 34.48 and the inner cylinder Reynolds numbers ranged between $R/R_c = 11$ and $R/R_c = 15$, where R_c is the critical Reynolds number for the primary instability. The variation of the dimension with Reynolds number was similar to that reported by Dr. A. Brandstater. No aspect ratio dependence of the attractor dimension was found in this study in the parameter space explored.

A second area explored was the bifurcation from Couette flow to secondary flow for counter-rotating cylinders. The bifurcation boundaries were located to an accuracy of 0.3% for outer cylinder Reynolds numbers ranging from 0 to -250. The locations of the codimension-2 points and the wavespeeds and axial wavelengths measured at the transition boundaries compared well with a recent linear stability analysis of Golubitsky and Langford. No hysteresis was found in the primary bifurcation boundary, but hysteresis of at least 3% of the outer cylinder Reynolds number was found in the secondary bifurcation boundary at the first codimension-2 point. No new states arising from mode competition were observed around the codimension-2 points.

THE ASPECT RATIO DEPENDENCE OF THE ATTRACTOR DIMENSION IN TAYLOR-COUETTE FLOW

by

Donald Allen Hirst, B.S., M.S.

DISSERTATION
Presented to the Faculty of the Graduate School of
The University of Texas at Austin
in Partial Fulfillment
of the Requirements
for the Degree of

DOCTOR OF PHILOSOPHY

THE UNIVERSITY OF TEXAS AT AUSTIN
December 1987

ACKNOWLEDGEMENTS

I would first and foremost like to thank Dr. Harry Swinney for accepting me as a student and for his time, patience and guidance in my pursuit of this research. Next I owe a debt which I hope to repay in a future paper to Dr. Randy Tagg for helping with the data collection, experimental design and other innumerable times he came to my assistance. To Dr. Eric Kostelich I owe thanks for help in data analysis and in preparing the dimension algorithms used in this research. I thank Andy Fraser for his help in using his mutual information programs and I wish him luck in shortly finishing his research.

I would like to thank Les Deavers and the crew in the physics machine shop for their tireless efforts to interpret my drawings and convert them into my desires (or at least something that works). To the rest of the members of the Center for Nonlinear Dynamics and the Physics department I would like to say that I enjoyed studying and learning with you. I would like to thank my wife Sharon for her patience during the time we spent apart while I worked in the lab late at night and on weekends, in putting up with moods of depression and the other sacrifices she made. To her I dedicate this work.

Table of Contents

Introduction

The transition to turbulence in fluid flow is a poorly understood physical phenomena. The governing differential equations for fluid flow are intractable for all but the simplest laminar flows and most flows of any practical importance are extremely complex. A simple fluid system which exhibits a range of complexity of flows in the transition to turbulence is the Taylor-Couette system. It has the advantage that the first laminar state, Couette flow, may be solved for exactly. As the driving terms (Reynolds numbers) are changed, the system shows a wide variety of states which exhibit characteristics of nonlinear systems (Anderick, et.al.,1986). The route to weak turbulence for the inner cylinder Reynolds number is well characterized for a small region of parameter space and it has been shown that such weak turbulence is chaotic; that is, the flow is aperiodic but deterministic with only a few degrees of freedom (Brandstater, Swinney, 1986). So, Taylor-Couette flow shows a variety of behaviors which may contain important clues to the understanding of turbulent flow.

In particular, the research for this dissertation was concentrated in two areas. The first was an experimental study of the states of near the primary bifurcation for counter rotating cylinders. The investigation was limited to the primary bifurcation in Taylor-Couette flow with inner cylinder Reynolds number. This study involved obtaining quantitative information on the transition for comparison with the predictions of linear stability theory. Measurements were made of the position of the primary bifurcation boundary and of various quantities such as axial wavelength and wavespeed. The results could indicate the accuracy of the approximations made by the linear theory as well as provide quantities for comparison with nonlinear theory when it becomes available.

The second area of study was the aspect ratio dependence of the attractor dimension in Taylor-Couette flow. The attractor dimension represents in some sense the number of degrees of freedom necessary to describe the flow. This does not mean that this represents the number of linear expansion functions necessary to accurately model the flow which are orders of magnitudes greater than the attractor dimension. This means the system may be adequately defined by a motion in phase space confined to a manifold having this dimension. The aspect ratio is a geometric quantity, not a dynamic one such as the Reynolds number. The question to be addressed by this research was whether the size of the system restricts the number of degrees of freedom available to the system.

The dissertation takes on this two part structure. The first chapter of this dissertation discusses stability and bifurcations in Taylor-Couette flow. After an introduction, the Navier-Stokes equations are introduced and the Taylor-Couette boundary conditions are discussed. Following this is the linear stability theory for Couette flow for symmetric and non-axisymmetric perturbations. Simple bifurcation theory is then introduced with an eye toward the kind of phenomena which might be observed from the structure of the bifurcation. Finally, a short discussion of the connection between bifurcations and the theory of equilibrium phase transition is presented to show the similarities in the descriptions of the behavior.

The second chapter introduces the theory of nonlinear dynamics. In this chapter are discussed such topics as fractal dimension, Lyapunov exponents, sensitivity to initial conditions and other ways of quantifying the behavior of a dynamical system. Included are some examples of simple ordinary differential equations which illustrate the importance of dissipative, nonlinear and forcing terms on the dynamics of the system. Next is a discussion of the transition to turbulence in the Taylor-Couette system with increasing inner cylinder Reynolds number. Following this is an examination of the actual computational methods necessary to obtain the measures of the dynamical systems from experimental data and the limitations on these methods. The chapter closes with a discussion of various theoretical estimates of the aspect ratio dependence of the number of degrees of freedom (attractor dimension) in fluid flow and in the Taylor-Couette system in particular.

The experimental methods and techniques used in the research performed for this dissertation are the subject of the third chapter. Two different experimental setups were used. The first set up discussed is the Gorman system which was used in the bifurcation study. The primary method of collecting data was visual. The second set up used was the Hirst system. This system was designed and built specifically for the aspect ratio dependence study. The primary data collection method was laser Doppler velocimetry. The experimental procedures for both systems are also described in this chapter. The chapter ends with a discussion of viscosity measurement.

Chapter 4 examines the results of the bifurcation experiment. The introduction sets the background and motivates the experiment. The rest of the chapter discusses the results and compares them to the predictions of Golubitsky and Langford's linear theory and to previous experimental results. The location of the primary bifurcation is shown to be close to that obtained by earlier experimenters though the present experiment is more precise. The measurements of axial wavelength, wave speed and the location of the codimension 2 points are shown to be close to the theoretical predictions. The primary bifurcation appeared to be supercritical for counter rotating cylinders between outer cylinder Reynolds numbers of 0 and -300. Additionally the secondary bifurcation boundary between Taylor vortex flow and spiral vortex flow coming off the first codimension 2 point is shown to have hysteresis of several Reynolds numbers.

The results of the aspect ratio dependence study is the subject of chapter 5. It examines the experimental data (time series from a laser Doppler velocimetry measurement of the radial velocity) and discusses the various measures which quantify the result. It is shown that for large enough aspect ratio (>25) the flow approaches independence of the aspect ratio. Finally, the results of the dimension calculations are discussed and it is shown that there is no aspect ratio dependence of the dimension in Taylor-Couette flow in the parameter space explored.

The dissertation ends with chapter 6 which summarizes the results of this study and presents the conclusions and directions for future research.

1. Stability and Bifurcations in Taylor-Couette Flow

1.1 Introduction

Fluid systems show a wide variety of complex behavior, particularly for turbulent flow. Most of the description of this behavior rests on modelling the observed behavior rather than deriving it from first principles. The equations which govern the fluid flow are known, i.e., the Navier-Stokes equations, nevertheless, these equations remain intractable for all but the very simplest flows.

There is a fundamental connection between the complexity and seeming randomness of turbulent fluid flows and the non-linearity of the Navier-Stokes equations. It is this non-linearity which mixes what would be called the linear (Fourier) modes of the system and thus allows this complex motion to take place. This mixing of modes is inconsistent with the Landau hypothesis of the transition to turbulence. That is, the complexity of the fluid motion cannot result from an increasing population of incommensurate frequencies, as the Reynolds number increases. The nonlinear coupling is so strong as to alter the structure of the motion in phase space. So, a continuum of frequencies are populated with the result that the motion is aperiodic when the Reynolds number is above some critical value. The non-linearity has the additional role of keeping the motion bounded. This happens because excess energy at one frequency is transferred by the nonlinearity to all the other frequencies since the nonlinearity tends to populate all the frequencies.

The Navier-Stokes equations are not only nonlinear but contain a dissipative term. The role of the dissipation is to damp the tendency for modes to become unstable. It allows the complex motion generated by the non-linearity to be stable since it provides a sink for the driving energy. This is different from the effect of the nonlinearity. The nonlinearity causes the various frequencies to share energy; the dissipation causes the energy to no longer be available to the various frequencies. The dissipation delays the onset of transitions of the various states. It does this by damping out other degrees of freedom, making the stable state low dimensional.

It is the number of degrees of freedom in the system that is of interest in this investigation. The question is what happens to the number of degrees of freedom as the system size is changed. The system chosen to pursue this research was the Taylor-Couette system. Recent studies by Brandstater and coworkers have shown that the transition to weak turbulence in Taylor-Couette flow leads through periodic flow and quasiperiodic flow to a low dimensional chaotic flow as the inner cylinder Reynolds number is increased (Brandstater, 1984, Brandstater et al., 1983). If this flow were stochastic instead of chaotic, then increasing the aspect ratio would increase the number of modes proportionally. What would happen in chaotic flow was not known prior to the research performed for this dissertation.

1.2 The Navier-Stokes Equations

Fluid flow for an incompressible, Newtonian fluid is governed by the Navier-Stokes equation:

$$\frac{\partial v}{\partial t} + (v \cdot \nabla)\, v = -\frac{1}{\rho}\nabla p + \nu \nabla^2 v + \frac{1}{\rho} F \qquad (1.1)$$

along with the continuity equation and the appropriate boundary conditions. Here v is the velocity field, p is the pressure, ρ is the fluid density, ν is the kinematic viscosity and **F** is some external force field. This is a non-linear, partial differential equation with dissipation. It is also deterministic. This is important to note because turbulence, which this equation should be able to model, is usually treated as some type of stochastic phenomenon. It is now clear that the complexity of turbulence can be modelled by the dynamics of equations like the Navier-Stokes equations. The fluid motion is deterministic despite the apparent complexity.

This study was focused on the transition to turbulence, that is, the first few steps. The flow regime of interest was far away from the regime of highly complex motion associated with developed turbulence. Therefore, this discussion starts with laminar flow in the Taylor-Couette apparatus. This flow is known as Couette flow.

A diagram of the boundaries of the flow for the Taylor-Couette apparatus is given in Figure 1.1. The boundary conditions are no-slip boundary conditions so the fluid velocity at the walls is the velocity of the walls. The apparatus is composed

Figure 1.1 Taylor-Couette Flow Boundary Conditions

The diagram illustrates the boundaries for the fluid in Taylor-Couette flow. The inner cylinder radius is "a". The outer cylinder radius is "b". The length is "L". The aspect ratio is given by L/(b-a). The radius ratio is a/b. The boundary conditions themselves are no-slip conditions at the walls of the cylinder and at the ends.

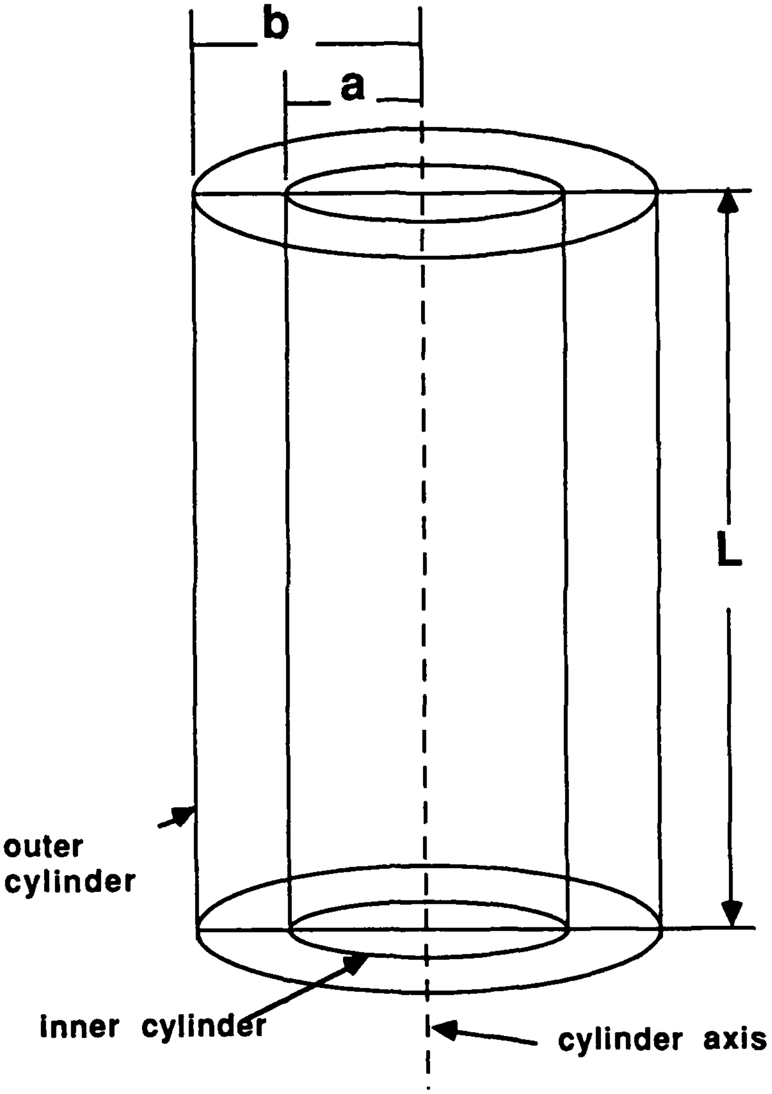

Figure 1.1 Taylor-Couette Apparatus

of inner and outer concentric cylinders which can turn independently in the most general case. Needless to say the fluid velocity at these surfaces is the same as the cylinders. The boundaries at the ends of the fluid between the cylinders cause some interesting experimental and theoretical problems. Experimentally the fluid at the ends moves with the same angular velocity as the end boundaries. This velocity depends on whether the ends are stationary or are attached to and move with the same speed as the inner or outer cylinder. Now the inner and outer cylinders are usually rotated at different speeds, resulting in a shear in the fluid velocity in the radial direction. But at the ends there can be no shear. Away from the ends in Couette flow, the radial pressure gradient is balanced by the centripetal force:

$$\frac{V_\theta^2}{r} = \frac{\partial P}{\partial r} \qquad (1.2)$$

V_θ is a function of r only, as may be seen in the next section (equation 1.4). It follows that the pressure will be a function of r (using equation 1.4, equation 1.2 may be immediately integrated). If the ends are solid then the no-slip boundary conditions give a velocity at the ends which is a constant. Clearly the forces no longer balance at the ends and there is a radial flow, inward for stationary boundaries. This flow is known as Ekman pumping. It fortunately has only a small effect on the flow though, as will be mentioned latter on, it can be very important in the selection of a stable flow state.

The ends also have a symmetry effect. If the flow has some periodicity along the axial direction, some integer wavelength of the flow must fit in the distance between the ends. This limits the available wavelengths in the axial directions to discrete values. This then will affect which flows will be stable. This is of particular importance in the flows in the onset to turbulence.

Theoretically, the ends are treated two ways: (1) the boundary conditions used are periodic, which means the shear extends across the ends but the allowable wavelengths are discrete or (2) an infinite cylinder is used, which means the ends are ignored. The first choice is more common since the Ekman pumping, as noted above, is usually weak but the wavelength selection is usually strong.

Having dealt with boundary conditions one can try to obtain a solution for the fluid flow by using the cylindrical symmetry of the Couette apparatus. The end boundaries may be treated as in (2) above; that is, the cylinder will be assumed of infinite length. With no-slip boundary conditions, the initial flow upon rotating the cylinders is expected to be directed azimuthally, perhaps with a radial dependence if the cylinders are rotated differentially. If a fluid flow of the suggested form is assumed, that is:

$$V = v(r)\ \hat{\theta} \qquad (1.3)$$

and substituted into the Navier-Stokes equation and the equation of continuity, the solution obtained is:

$$V = (Ar + \frac{B}{r})\ \hat{\theta} \qquad (1.4)$$

where $A = -\Omega_1(\eta^2 - \mu)/(1 - \eta^2)$ and $B = \Omega_1 a^2\ (1 - \mu)/(1 - \eta^2)$; Ω_1 is the inner cylinder rotational frequency, a is the inner cylinder radius, η is the ratio of the inner and outer cylinder radii and μ is the ratio of the outer to inner cylinder rotational frequencies. This initial flow, known as Couette flow, is a featureless flow. The velocity field is directed azimuthally and shows only a radial dependence (Currie, 1974, p. 229).

Now, what is seen experimentally? Assume first for simplicity that the outer cylinder is stationary and allow the inner cylinder to rotate. As the inner cylinder starts the fluid is in Couette flow. Any motion radially is damped by the fluid viscosity. As the inner cylinder is further accelerated, a velocity is reached at which the centrifugal acceleration of the fluid can overcome the viscous damping and this results in an instability. The resulting flow is shown in figure 1.2 and is known as Taylor vortex flow. The flow consists of vortices, stacked along the cylinders with every other vortex having the same flow pattern. These vortices are paired and it is convenient to define an axial wavelength as the vertical extent of two vortices, as

Figure 1.2 Taylor Vortex Flow

The diagram at left illustrates Taylor vortex flow. The circulation shown in the small circles is superimposed upon the azimuthal Couette flow which at least an order of magnitude larger. The wavelength, λ, is defined as shown to be the sum of the diameter of two of the vortices. It is this pair structure which is periodic axially in the flow.

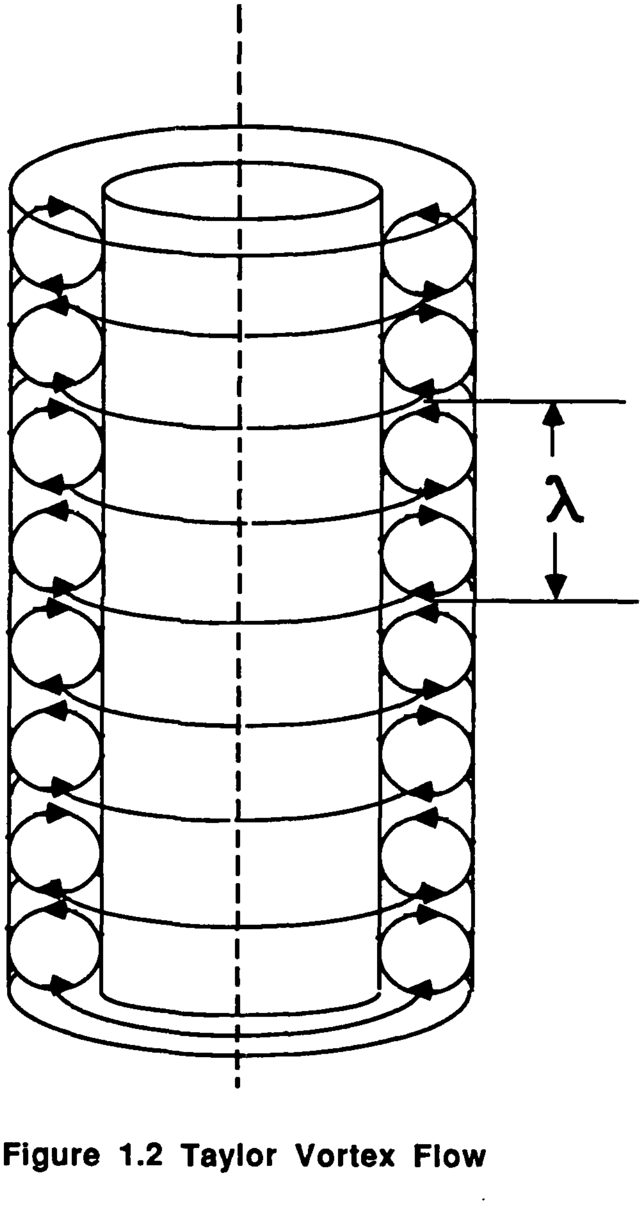

Figure 1.2 Taylor Vortex Flow

shown. A normalized axial wavelength is defined by dividing the axial wavelength by the gap between the cylinders.

Note that this is the first step in the transition to turbulence in the Taylor-Couette system. The transition is from a steady-state featureless flow (Couette flow) which (ignoring the Ekman pumping) has rotational invariance about the cylinder axis for any angle of rotation and is translationally invariant along the axis for any translation. The transition is to a steady-state flow (Taylor vortex flow) which has the same rotational symmetry as Couette flow but now has a periodic translational invariance of a wavelength. The transition has demonstrated symmetry breaking. The symmetry of the flows has a profound effect on the stability of the available flow states in the Taylor-Couette system (Golubitsky, Stewart, preprint, Chossat, Iooss, 1985, Demay, Iooss, 1984, Langford, et. al., to be published).

1.3 Linear Stability Theory

As shown above the exact solution to the Navier-Stokes equation for Couette flow (assuming an infinitely long cylinder) is known and easy to derive. Mathematically it is possible to predict the transition to Taylor flow though there is no analytical solution to the Navier-Stokes equation for Taylor flow. One may look at the stability of Couette flow to infinitesimal perturbations in the flow. It is easiest to follow Taylor's example and try axisymmetric perturbations. The following are substituted into the Navier-Stokes equations and the equation of continuity:

$$V_x = u(r,z,t); \quad V_y = V + v(r,z,t); \quad V_z = w(r,z,t) \qquad (1.5)$$

where u,v,w are small compared with V, the Couette velocity, and are assumed azimuthally symmetric (no θ dependence). One may linearize the equation by keeping only terms linear in u,v,w. Now, assuming no-slip boundary conditions (that is, all velocity components are zero at the boundaries) and that the perturbations have the following form:

$$\begin{aligned} u &= u_1(r) \cos \lambda z e^{\sigma t} \\ v &= v_1(r) \cos \lambda z e^{\sigma t} \\ w &= w_1(r) \sin \lambda z e^{\sigma t} \end{aligned} \tag{1.6}$$

the velocities (equation 1.5) may be substituted into the Navier-Stokes equation. The resulting ordinary differential equations for the radial dependence may be solved by using Fourier-Bessel expansions. The wavelength is chosen by setting $\sigma = 0$ in the equations thus obtained and finding the wavelength such that the inner cylinder Reynolds number is a minimum. This follows the assumption that the first stable state will be the fastest growing and will dominate the flow, at least near onset. Also the form of the resulting flow can be deduced to be vortices stacked one on the other, like donuts stacked along the inner cylinder (Taylor, 1923).

Taylor's predictions agree well with experiment provided the outer cylinder Reynolds number is not too negative. In this region of parameter space the flow pattern seen is Taylor vortices, and the critical Reynolds numbers for onset and the wavelength agree well with experiment. If the outer cylinder Reynolds number is too negative ($(\Omega_1 / \Omega_2) < -0.78$ for a radius ratio close to 1) then experimentally the flow is seen to be spirals, violating Taylor's assumption of azimuthal symmetry (Krueger, Gross, Di Prima, 1966).

The same procedure can be followed for non-axisymmetric perturbations. The perturbation is now assumed to be of the form:

$$u = u_1(r) \exp i(m\theta + \lambda z)\, e^{\sigma t} \tag{1.7}$$

and so forth for the other velocity fields. Unlike in the purely axisymmetric case, σ may be complex. Once again the Couette flow field plus these perturbations are substituted into the Navier-Stokes equation. There results an infinite set of equations; two for m = 0 and four for each integer value of m > 0, the degeneracies being due to the cylindrical symmetry. Fortunately, only the first several values of m need be examined. Computationally these are treated as equations for the eigenvalues σ in terms of the parameters m and λ. Needless to say, since σ can be complex, time dependent behavior is now possible. Couette flow will become unstable to the perturbation labeled by m and λ when the associated eigenvalues cross the imaginary axis.

Now consider experimentally how the stability diagram is obtained. Usually a preselected value of the outer cylinder Reynolds number is obtained, with the system still in Couette flow. Then the inner cylinder Reynolds number is increased until a transition is observed. Computationally, one chooses an outer cylinder Reynolds number at which one wishes to know the inner cylinder Reynolds number for the transition from Couette flow. The inner cylinder Reynolds number is then increased until the real part of σ goes through zero. Now σ is a function of λ and m. Those parameters associated with the smallest value of the inner cylinder Reynolds number at which Couette flow becomes unstable are assumed to be those belonging to the new stable state. This follows the usual perturbation theory practice of assuming the first eigenvalue to cross the real axis will also be the fastest growing. If it is desired to obtain the bifurcation boundary, the above given process is continued for a series of outer cylinder Reynolds numbers (Krueger, Gross, Di Prima, 1966, Di Prima, Grannick, 1971).

As may be observed, the above analysis only gives the form of the perturbation to which the system becomes unstable. In the case of these non-axisymmetric modes, there are several modes which can become unstable simultaneously. It is possible to take combinations of these to form states of a variety of symmetries. Two experimentally observed states corresponding to m=1 are spirals and wavy vortex flow. Linear theory will not reveal which of these states is actually the one to which the transition is made. A non-linear analysis is then necessary (Krueger, Gross, Di Prima, 1966). Nevertheless, out of the linear analysis one can obtain the axial wavelength, azimuthal wavenumber and azimuthal frequency which can be compared to experimental results. In addition to these quantitative methods, bifurcation theory may also aid in understanding the transition phenomena.

1.4 Bifurcation theory

Bifurcation theory deals with the qualitative changes in the state of a system as it makes a transition. It provides a way of obtaining some of the qualitative behavior of the system from the governing differential equations. One may have a set of ordinary differential equations describing the physical system:

$$\frac{dx_i}{dt} = f(x_i,\lambda_i) \qquad (1.8)$$

where the x_i are state variables and the λ_i are bifurcation parameters. Examples of the λ_i might be the inner and outer Reynolds numbers for Taylor-Couette flow. The x_i could be the mean radial velocity at some particular location in the flow or some similar quantity. Setting the derivative to 0 gives a set of equations for the steady states (not necessarily stable) of the system. A graph of $f(x_i,\lambda_i) = 0$ for all the values of $\{x_i\}$ and $\{\lambda_i\}$ is called a bifurcation diagram. This diagram shows the steady states of the system in the x_i,λ_i space. There may be branching or intersecting of these states. The locations of these intersections are the values of $\{x_i\}$ and $\{\lambda_i\}$ where the Jacobian of $f_\lambda(x_i)$ vanishes and this defines the bifurcation point (I have rewritten $f(x_i,\lambda_i)$ to emphasis that the λ_i are parameters) (Guckenheimer, Holmes, 1983).

Let me now limit my discussion to a hypothetical system with one state variable and one bifurcation parameter. In figure 1.3(a) is a bifurcation diagram for the equation:

$$f_\lambda(x) = \lambda x - x^3 \qquad (1.9)$$

This type of bifurcation is generally known as a pitchfork bifurcation, for obvious reasons. It is also an example of a supercritical bifurcation since new states (the outer "prongs" of the pitchfork) occur for values of the bifurcation parameter larger than the critical value. The horizontal axis corresponds to the bifurcation parameter and the vertical axis to the state variable. The flow is stable for all values of $\lambda < 0$ with $x = 0$. For $\lambda > 0$, there are three states. The original state with $x = 0$ is unstable. The two stable states have values $x = \pm\sqrt{\lambda}$. The point $\lambda = 0$ is the bifurcation point. This equation and its bifurcation diagram could model the

Figure 1.3 Pitchfork Bifurcation

Shown are several examples of the pitchfork bifurcation. Stable states are represented by a solid line and unstable states are represented by a dashed line. (a).This is an example of a perfect supercritical pitchfork bifurcation. It is symmetric about x=0 and both secondary stable states are continuous with the primary state. The primary state becomes unstable after the bifurcation point is passed. (b).This is an example of an imperfect supercritical bifurcation. The symmetry obvious in (a) has been broken and is representative of some broken symmetry in the flow. The lower state can no longer be reached by an infinitesimal perturbation. (c) This imperfect subcritical bifurcation shows a discontinuous change to the stable secondary state. (d).This is an enlarged portion of (c) to show the hysteresis in the state as the parameter λ is first increased through the bifurcation and then decreased. It should be noted that the subcritical bifurcation may be perfect as well as imperfect and so there is the possibility of three simultaneously stable states along with the hysteresis.

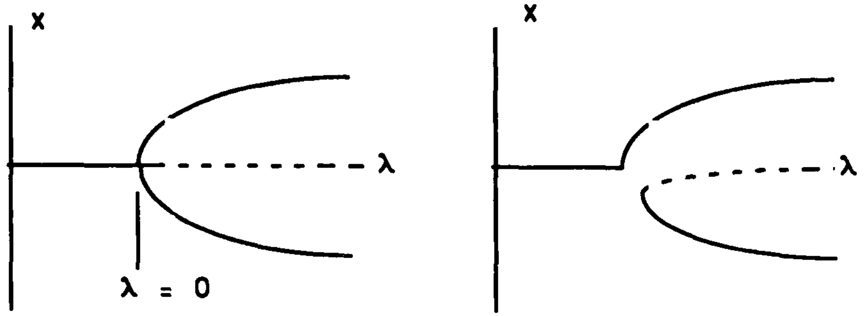

(a) Perfect Pitchfork Bifurcation

(b) Imperfect Pitchfork Bifurcation

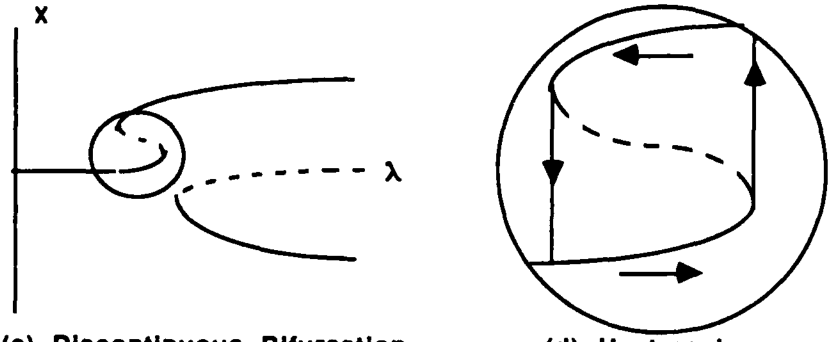

(c) Discontinuous Bifurcation

(d) Hysteresis

Figure 1.3 Pitchfork Bifurcations

transition from Couette flow to Taylor vortex flow, for instance. The second of the two stable states in Taylor vortex flow would correspond to the flow pattern being shifted by half a wavelength. This symmetry of the apparatus along the axis is reflected in the symmetry of the bifurcation diagram.

The symmetry of the bifurcation diagram can be broken if the symmetry of the apparatus is broken. In actuality this is what happens. In the discussion on Couette flow above, the weak effect of Ekman pumping was mentioned. This produces two large, weakly flowing vortices with their boundary axially equidistant from the ends. This flow breaks the symmetry of the Taylor vortex flow and only one state is seen in practice, if the transition boundary is quasi-statically crossed. The bifurcation diagram for such a flow is shown in figure 1.3(b). The lower branch is not continuous with the stable Couette flow. To reach this state, the flow must undergo a finite perturbation. This bifurcation diagram is not the only possibility.

Yet another bifurcation diagram which shows a different result of symmetry breaking is shown in figure 1.3(c). One of the stable Taylor vortex branches is connected to the Couette flow via a path which is unstable. The path, opening to the left, is subcritical. Notice that a portion of the stable Taylor vortex flow has the same value of the bifurcation parameter, λ, as the stable Couette flow. Figure 1.3(d) has a portion of 1.3(c) enlarged around the bifurcation point. On this, the path of the system takes for increasing bifurcation parameter and for decreasing bifurcation parameter are drawn. This plainly shows hysteresis in the bifurcation; that is, which state is stable for this limited value of λ depends of the path taken to that value of λ.

Other types of bifurcations exist. The most important of these for the purposes of this dissertation is the Hopf bifurcation. A Hopf bifurcation involves a transition from a stable, steady, time-independent state to a stable, steady, time-periodic state. In the linear stability analysis given above for the transition to Taylor flow, the perturbed velocities had a time dependent part. The eigenvalues of the equations obtained after substituting in the expressions for the perturbations are the σ's multiplying the time in the exponentials. For steady flow the real part of the σ's are negative. Upon the transition to a new state the real part becomes positive. If the imaginary part is zero, another steady flow results. If the imaginary part is non-zero, a time-periodic flow occurs. In the first case, Couette flow becomes

Taylor vortex flow; in the second case, Couette flow becomes a time periodic flow (shown in chapter 4 to be spiral vortex flow).

The point of this discussion of bifurcations is to point out the kind of behavior to look for in a transition. The simple models suggest types of behavior such as hysteresis, multiple stable states, time periodic states and the like. Often a problem in a large state space can be reduced to a problem in a smaller space by center manifold theory, which basically retains only those coordinates which contain the essential dynamics of the problem. Looking at the dynamics in this smaller state space with its correspondingly simpler bifurcation diagram can yield a qualitative description of the bifurcation (Hirsch, Smale, 1974).

The example given above is an example of a codimension one bifurcation. "The codimension of a bifurcation will be the smallest dimension of a parameter space which contains the bifurcation in a persistent way " (Guckenheimer, Holmes, p. 123). Now, in a study of Taylor-Couette flow there could be a very high degree of codimension. The available parameters are the aspect ratio, the radius ratio, and the inner and outer cylinder Reynolds numbers, at the very least. Of these, however, the last two are the parameters that can easily be continuously changed. So, this experimental study will look at phenomena of either codimension one or two.

Now, what does the definition mean by saying "the dimension of a parameter space which contains the bifurcation in a consistent way"? Consider first the transition from Couette flow to Taylor vortex flow. This is a codimension one phenomenon. If the outer cylinder Reynolds number, the aspect ratio or radius ratio are changed slightly, the transition from Couette flow to Taylor flow will be found for some continuous range of these parameters. Another way of saying this is that the bifurcation is insensitive to small perturbations in the parameters or is "structurally stable".

Now, for small enough (sufficiently negative) outer cylinder Reynolds number the primary transition is from Couette flow to a non-axisymmetric state. A portion of the research for this dissertation studied the vicinity of the point on the transition boundary where the secondary flow changes from Taylor flow to non-axisymmetric flow. The change in transition appears as a point in parameter space (i.e., on a graph of the stable flow states where the axes are the parameters, such as the inner and outer cylinder Reynolds numbers). It is easy to see that if the outer cylinder Reynolds number, the aspect ratio or the radius ratio are changed slightly, this point cannot be found by only changing the inner cylinder Reynolds number. However, if both the outer and inner cylinder Reynolds numbers can be adjusted, then that point can be found. The bifurcation associated with passage through this point is of codimension two.

The fact that this point is of codimension two is important because there are more phenomena associated with a codimension two bifurcation than a codimension one bifurcation. It is also important to note that such phenomena may occur locally about the point and not just at the codimension two point. In particular there is the possibility of unexpected states arising from the competition of the nearby stable states (Golubitsky, private communication). So, in searching about the codimension two point for transition boundaries and for various behaviors, it is necessary to be aware of the influence of the codimension two point.

1.5 Analogy with equilibrium phase transitions

A comparison can be drawn between the bifurcations and phase transitions at critical points in equilibrium thermodynamics. This is not to say the underlying mechanisms are the same but that there are similarities in the growth of new states with respect to the bifurcation parameters. Both cases deal with symmetry breaking transitions. There is the appearance of a macroscopic parameter, the order parameter, in the less symmetric phase (Reichl, 1980). It will be interesting to explore the analogy. First a review of the Landau theory will be given and then it will be compared to the results of some experimental studies.

Landau (or Ginzberg-Landau) theory starts out by assuming a form for the thermodynamic potential of the system. In a true equilibrium situation this might be the free energy or some similar quantity. What it is for a system like the Taylor-Couette system which is far from equilibrium is not clear but it will be assumed that such a quantity can be defined. It should be pointed out that this assumption only seems to be possible near the primary instability and that for higher instabilities it is not valid. However, the interest here is in the primary bifurcation. The potential will be assumed to be of the form:

$$\Phi = \Phi_0 + \frac{1}{2}\Phi_2 x^2 + \frac{1}{4}\Phi_4 x^4 + \ldots \qquad (1.10)$$

where Φ is the thermodynamic potential, Φ_i are the coefficients in the expansion and x is the order parameter. The fact that there are no odd terms is a reflection of a symmetry in the physical system. This quantity must be a minimum of the system and so it must minimized above and below the transition point. The solutions are:

$$x = 0, \pm\sqrt{-\Phi_2/\Phi_4} \qquad (1.11)$$

By requiring that the minima are global minima and demanding continuity of the free energy as a function of ε:

$$-\Phi_2/\Phi_4 \propto \left|\varepsilon - \varepsilon_c\right| \qquad (1.12)$$

And so:

$$x = x_0\ \varepsilon^{0.5} \qquad (1.13)$$

The power of ε is known as the critical exponent. It is interesting to note that for equilibrium phase transitions the Ginzberg-Landau theory gives the wrong value of the exponent as the bifurcation point is approached since it is a mean field theory (it ignores short range order) (Reichl, 1980).

Several experimental studies have been conducted to compare the behavior of some quantity defined as the order parameter with the distance from the bifurcation. In one, the transition from Couette to Taylor vortex flow was studied for a stationary outer cylinder (Berland, Jossang, Feder, 1986). The order parameter was chosen to be the first harmonic of the radial velocity of the flow field and was measure by reference beam Laser Doppler Velocimetry (LDV) as a function of the inner cylinder Taylor number (the Taylor number is proportional to the square of the Reynolds number). The distance from the bifurcation, ε, was defined as:

$$\varepsilon = \frac{T-T_c}{T_c} \qquad (1.14)$$

where T_C was the Taylor number at the bifurcation. The critical exponent was determined to be 0.51± 0.03. (Berland, Jossang, Feder, 1986).

Another study of interest was that done by Aitta, Ahlers and Cannell on the bifurcations in a small aspect ratio system (Aitta, Ahlers, Cannell, 1985). In particular, they established in the system a pair of equal sized vortices. Beyond a certain Reynolds number, R_C, one vortex would start growing in diameter at the expense of the other one. This was observed to be an imperfect bifurcation as in figure 3(c) which was apparently due to physical imperfections in the apparatus. Now, as the aspect ratio of the system was varied from 1.129 to 1.281 the bifurcation changed from supercritical to subcritical. The order parameter here was:

$$X = \frac{\int_0^L v_z \, dz}{\int_0^L |v_z| \, dz} \qquad (1.15)$$

where L was the length of the fluid along the axial direction and z was the distance along the axial direction. This would be similar to a first order phase transition and the point at which the bifurcation changed from supercritical to subcritical similar to a tricritical point in equilibrium thermodynamics. In Landau theory the breaking of symmetry which causes the imperfect bifurcation can be modelled by a linear term in the free energy:

$$\Phi = \Phi_0 + \Phi_1 X + \frac{1}{2}\Phi_2 X^2 + \frac{1}{4}\Phi_4 X^4 + \frac{1}{6}\Phi_6 X^6 + .. \qquad (1.16)$$

However, in the theory for the ordinary critical point there is a restriction that $\Phi_4 > 0$ for stability. Here that restriction is removed and it is required that $\Phi_6 > 0$ for stability. While the first order term breaks the symmetry, it is the fourth order term that causes the transition to change from second order to first order. The tricritical point occurs when the fourth order term passes through zero. Experimentally, changing the fourth order corresponds to changing the aspect ratio over the indicated range of values. Such a description is able to model the observed behavior within the experimental error.

The rationale for reviewing these experimental results is to point out that the Landau equations seem to model the growth of states of the Taylor-Couette primary bifurcations. Now, the mean field approach, of which the Landau theory is an example, ignores the importance of short range order. In equilibrium thermodynamics this is wrong and mean field theory gives the wrong values for the exponents (Stanley, 1971). Two experiments in Taylor-Couette flow were described above in which the Landau theory gives the correct exponents and seems to model the bifurcations. A theoretical analysis of the transition to rolls in Benard convection implied that for hydrodynamics systems the correction to the free energy (or amplitude) term due to the short range fluctuations was of the order of 10^{-9} times the free energy (Swift, Hohenberg, 1977). Thus, the effect should never be seen and Landau theory should be valid in a practical sense for transitions in fluid systems.

Another phenomenon which the transition in a Taylor-Couette system shares with equilibrium phase transitions is the appearance of critical slowing down. In a thermodynamic system an approach to a critical point results in critical slowing down of the fluctuations. The slowing down is not of the speed of the fluctuations but the rate at which they die down as the system relaxes. This is simply a result of linear response theory. There is a limit to the critical slowing down, however. This occurs when the fluctuations become as large as the system. Then the fluctuations can get no larger and neither can the critical slowing down. Thus, for a system which exhibits critical slowing down it can be shown that the critical slowing down goes as L^4 where L is the characteristic length of the system (Reichl, 1980). If one dimension of the system is considerably larger than the other dimensions then the critical slowing down will go as L^2 since the time limiting fluctuations will occur in essentially one direction. This is exactly the functional relation with respect to the length of the Taylor-Couette system derived by Snyder from dimensional analysis for the time for axial perturbations to travel from one end of the cylinder to the other.

2. Dynamical Systems and Chaos

2.1 Introduction

As stated in the first chapter, fluid flow in the Taylor-Couette system may be described by the solution(s) to the Navier-Stokes equation, the continuity equations and the Taylor-Couette boundary conditions. This set of equations, together with the boundary conditions, constitutes a dynamical system. A dynamical system gives the time evolution of the system. Dynamical systems theory develops some quantitative measures which may be applied to the evolution and so help to characterize the behavior of the system. The purpose of this chapter is to discuss dynamical systems to the extent necessary to understand these measures and their application to real world problems. The final section discusses attempts to determine upper bounds for the density of degrees of freedom in dynamical (fluid) systems which might provide an estimate of the dependence of the degrees of freedom (attractor dimension) with aspect ratio.

2.2 Dynamical systems

Dynamical systems theory contains a number of concepts that are most easily demonstrated by examples. First, however, a rather formal definition of a dynamical system will be given and then some examples will follow which illustrate both the definition and some terminology. According to Hirsch and Smale, the dynamical system is the map $\varphi_t:\pi\to\pi$, which satisfies:

1. $\varphi_0:\pi\to\pi$ is the identity and
2. the composition $\varphi_r \circ \varphi_s = \varphi_{r+s}$ for each r,s in R (Hirsch,Smale, 1974).

Here s,r are simply values of time, π is the phase space of the system where the system is defined and the range of $\varphi_t(x \in \pi)$ is a solution curve or trajectory for all t and a given initial condition x_0. The map mentioned in the definition need not be a differential equation, i.e., it could be a discrete map.

The simplest example of a dynamical system is the harmonic oscillator. The differential equation is:

$$\frac{d^2x}{dt^2} = -kx \tag{2.1}$$

Typically, this is written as a system of first order equations:

$$\frac{dx}{dt} = y$$

$$\frac{dy}{dt} = -kx \tag{2.2}$$

The solution with the initial conditions $x(t_0) = x_0$ and $y(t_0) = 0$ is just $x = x_0 \cos k(t-t_0)$. The solution curves or trajectories to this equation are ellipses in the phase space, $\{x,y\}$, as shown in figure 2.1(a). For a differential equation the map is known as a <u>flow</u> and in this particular case the flow is: $\varphi_t(x_i) = x_i \cos k(t-\tau)$ for all initial conditions x_i and τ. Another way of looking at this is to say the flow consists of the set of all the trajectories.

If one is looking at time-dependent systems, the question of stability arises: basically, what happens to the motion if it is perturbed? The motion may be neutrally stable, asymptotically stable or unstable. The simple harmonic oscillator system is neutrally stable in that, if the trajectory is perturbed, the new trajectory remains close to the original trajectory. This follows from the fact that the simple harmonic oscillator equation of motion contains no dissipative terms. If after perturbation the motion of the system approached the original trajectory asymptotically as time increased, then the system would be said to be asymptotically stable. The motion would be said to be unstable if it were neither stable or asymptotically stable.

One more important concept is that of periodic trajectories. A trajectory is said to be periodic with period T if the trajectory repeats itself every T seconds. More formally, a trajectory is periodic with period T if: $\varphi_t(x_0 \ \varepsilon \ \pi) = \varphi_{t+T}(x_0 \ \varepsilon \ \pi)$. There may be harmonics of the fundamental frequency but the trajectory will still be

Figure 2.1(a) Phase space for the simple harmonic oscillator. Here are plotted several representative trajectories. A perturbation of trajectory a to trajectory b does not result in a qualitative change in the behavior of the system. (b) Phase space of a pendulum. This is an example for a nonlinear oscillator. The saddle points are labelled "u" and the separatrices are the trajectories passing through the saddle points. Notice the increase in curvature as the trajectory approaches the saddle point; this results in a population of the odd harmonics of the frequency of oscillation.

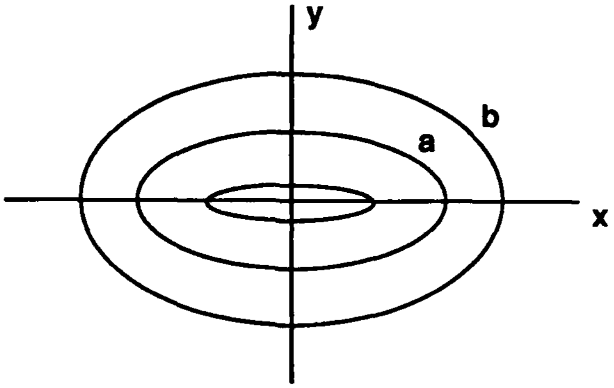

Figure 2.1(a) Phase space for simple harmonic oscillator

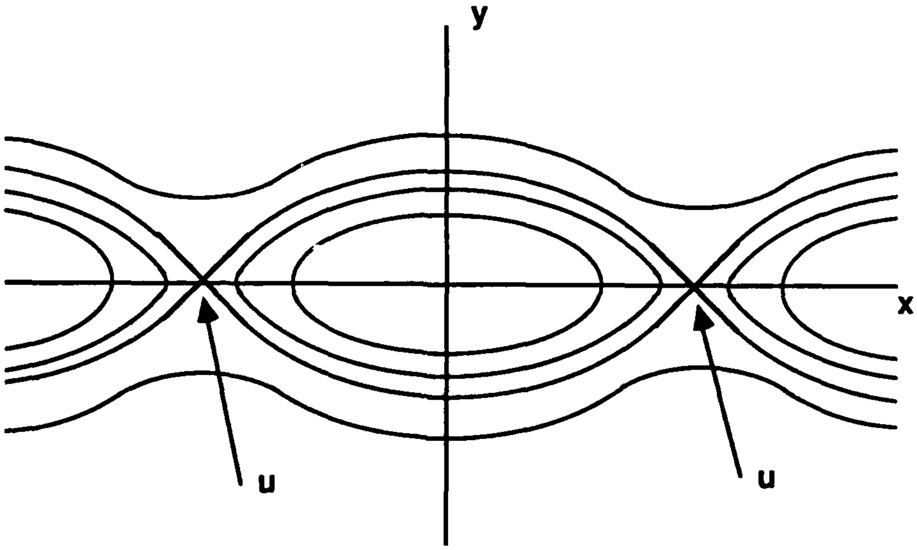

Figure 2.1(b) Phase space for nonlinear oscillator

periodic. The harmonics only serve to distort the trajectory from an ellipse. If there were two frequencies associated with the motion and the second was not commensurate with the first, the trajectory would be quasi-periodic. In general, for n incommensurate frequencies, the motion is n-periodic. The motion of the simple harmonic oscillator has only one frequency, $k^{-1/2}$, corresponding to the inverse of the orbital period.

If the equation is nonlinear, the trajectories can be more complex. For an example of a nonlinear equation, one may use the simple pendulum. For small amplitudes of displacement the equation of motion can be approximated by that of the simple harmonic oscillator. For larger amplitudes the correct equation is:

$$\frac{dx}{dt} = y$$

$$\frac{dy}{dt} = -k \sin x \qquad (2.3)$$

Similar to the simple harmonic oscillator, this system has a two dimensional phase space as shown in figure 2.1(b). However, this system has a new feature due to the nonlinearity. The points marked "u" are <u>saddle points</u>; that is, the trajectories through these points are stable along one direction and are unstable if they are perpendicular to that direction. The trajectories that pass through the saddle points are separatrices; they separate two different kinds of motion. Inside the separatrices the motion oscillates back and forth about the equilibrium position. Outside the separatrices, the motion is continually in one direction. That is, the pendulum "goes over the top". As the trajectories get closer to the saddle point, they get more distorted near the x-axis. Since this occurs at odd multiples of π of the orbit, the odd harmonics are excited. If a spectrum were obtained of the periodic motion, one would find odd harmonics of the frequency corresponding to the periodic motion. Still the frequency components are sharp. The nonlinearity brings the saddle points into existence and causes the population of the odd harmonics.

Now, continuing in this way, one may add a damping term. The equation is:

$$\frac{dx}{dt} = y$$

$$\frac{dy}{dt} = -k \sin x - By \qquad (2.4)$$

If the system is now started with some amplitude, the amplitude decays exponentially at the rate B until the system comes to rest at x = y = 0. The point x = y = 0 is called a fixed point and is a stationary point of the dynamical system (figure 2.2(a)). It is asymptotically stable since any small perturbation from the fixed point will eventually be damped and the system will return to it. It is also an example of an attractor. An attractor is simply the limit set of the trajectory as time goes to infinity. The basin of the attractor is the region of the phase space in which any initial condition yields a trajectory with the attractor as a limit set. In the case of the damped pendulum, the basin is the entire phase space.

The damped pendulum may be made more interesting by adding a forcing term. Some useful concepts can be introduced with a minimum of complexity if first the linear forced, damped oscillator is considered. The equation of interest is:

$$\frac{dx}{dt} = y$$

$$\frac{dy}{dt} = -kx - By + G \sin \omega t \qquad (2.5)$$

The magnitude of the forcing is G and the forcing frequency is ω. There are still two dynamical variables: x and y. However, there are now three parameters: B,G, and ω. The qualitative description of the motion depends on how strongly it is driven with respect to the dissipation. Typical behavior is shown in figure 2.2(b) in a projection of the phase space into the x-y plane. There is an attractor but now it is a loop instead of a point. This is known as a limit cycle. Like the simple harmonic oscillator, there is only one frequency. However, now the frequency is the driving frequency of the forcing term (it is assumed the system has been running long

Figure 2.2(a) Phase space for the damped oscillator. This simple figure shows the trajectory of a system decaying to the focus. A forced, damped system in which the driving force cannot overcome the damping would look the same. (b) Phase space of a forced, damped oscillator. In this system the forcing and the dissipation are balanced. The stable state is the limit cycle to which all trajectories approach as time increases. For initial conditions inside the limit cycle the forcing overcomes the damping and drives the system outward. For initial conditions outside of the limit cycle the damping overcomes the forcing and the system decays inward. Actually, increasing the forcing in the system represented by figure 2.2(a) will cause the system to reach figure 2.2(b) and so the two figures represent the state of a system on opposite sides of a bifurcation point.

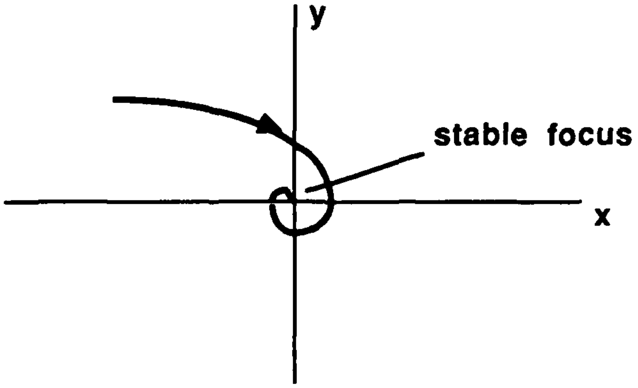

Figure 2.2(a) Phase space for damped oscillator

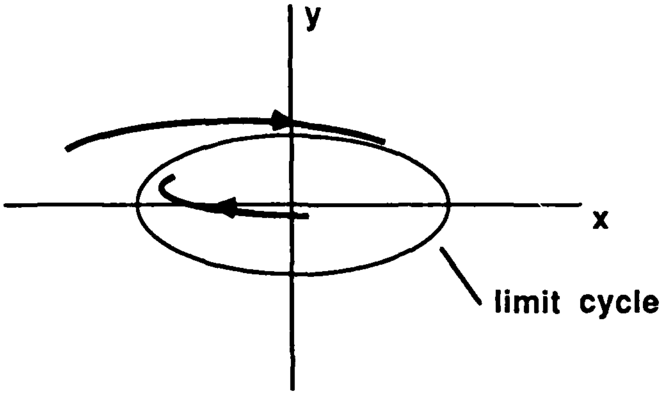

Figure 2.2(b) Phase space for forced,damped oscillator

enough for transients to die out). The domain of attraction is still the entire phase space with points interior to the limit cycle giving rise to trajectories approaching the attractor by spiraling outward. (Thompson, Stewart, 1986).

A more complex example is the forced Duffing oscillator. The equation for this oscillator is:

$$\ddot{x} + B\dot{x} + kx + x^3 = G \cos\omega t \tag{2.6}$$

It is possible to rewrite this equation in a form which is almost canonical for dynamical systems, i.e., in terms of first derivatives of the dynamical variables with respect to time. Thus:

$$\begin{aligned} \dot{x} &= y \\ \dot{y} &= -By - kx - x^3 + z \\ \dot{z} &= -G\omega \sin \omega t \end{aligned} \tag{2.7}$$

This is basically the damped, driven oscillator with an added nonlinear term: $-x^3$. This added term can affect the behavior of the system dramatically. The structure of the phase space depends on the values of the driving force, the damping and the nonlinearity. For weak nonlinearity and weak damping the phase space will resemble those examples discussed above. However, as the driving force and the nonlinearity become large, several new features occur in the phase space, most of them typical of non-linear damped, driven systems.

For example, several different stable attractors may exist in the phase space with their own non-overlapping basins of attraction. The long time motion of the system then depends not only on the parameters B and G but also on which basin the initial conditions were located. It is profitable in these complex systems to plot the stable states in the parameter space of B and G (by states are meant motion on an attractor which has been uniquely labelled by some characteristics of the motion such as frequency, wavelength, etc.). Simultaneously stable states overlap in such a plot. The routes to these simultaneously stable states varies and a path in parameter space may show hysteresis. For instance, increasing the driving force, G, of the above oscillator may drive the system discontinuously from a limit cycle with amplitude A at G_1 to a limit cycle with amplitude A' where A'<<A. On lowering G the amplitude may again change discontinuously from a small amplitude state to a large amplitude state but at G_2 instead of G_1. This was seen in the last chapter in the discussion of bifurcation theory. Figure 1.3(d) shows this kind of hysteresis. There the parameter was called λ and the parameter space was simply a line. (Guckenheimer, Holmes, 1983). Another new feature, important for turbulent motion, is the appearance of chaotic attractors for certain ranges of the parameters. A discussion of chaotic attractors and chaos are the topics of the next section.

2.3 Chaos

First, it will be necessary to come up with a working definition of chaos. There is no formal, accepted definition of the word in the sense used here (Bai-Lin, 1984). Here, at least, an attractor will be said to be chaotic if it has the following properties:

1. The motion is formally deterministic.
2. The motion is bounded in phase space.
3. The motion is sensitive to initial conditions.

The first property means that the equations of motion of the system are deterministic as opposed to stochastic. That is, if the equations of motion could be solved exactly, the motion of the system would be known exactly for all time. The second property means that the motion is limited to some finite region of phase space.

The third property is a little more involved. It means that the trajectories for two initial points, each corresponding to a distinct trajectory and arbitrarily close together, separate exponentially fast on the average for infinitesimal separations. Thus, after a finite time, the trajectories could find themselves on opposite sides of the attractor. This property leads to a degree of indeterminism of chaotic systems in a practical sense. This comes from the observation that any specification of the initial conditions, experimentally or computationally, will have errors. Initial conditions can be defined arbitrarily close together and yet will spread. The Lyapunov exponents provide a measure of the spreading . The exponents are basically the rate of spreading of neighboring trajectories on the attractor in a given direction

(Brandstater, 1984). If the Lyapunov exponents are negative then there obviously is no spreading since the separation decreases monotonically with time. Chaotic motion is characterized by one or more positive Lyapunov exponents. A discussion of the computation of Lyapunov exponents from experimental data appears in section 2.5.4.

For the trajectories to spread yet remain bounded, the attractor must have a highly complex topology. Unlike the attractor for periodic flow (limit cycle) or quasiperiodic flow (torus), a chaotic attractor is not smooth in some regions in directions perpendicular to the trajectories on the attractor. The trajectories in these regions lie in sheets which are generated by folding. The set of sheets are like a Cantor set. This is more easily seen in what is known as a Poincaré section of the attractor. A Poincaré section (or map) is created by cutting the trajectory in a d-dimensional phase space by a (d-1)-dimensional hyperplane (Schuster, 1984). The section will show the leaves generated by the folding (see figure 2.3). If a small section of the Poincaré map is blown up where folding occurs, folding will still be seen. This process can be continued forever (or at least to the resolution of the computer precision or the experiment).

It will be noticed that the Poincaré section does not fill the plane. Likewise the chaotic attractor will not fill the space in which it is embedded. So, the attractor has a dimension less than that of the embedding space. For the separation of the trajectories to be exponential and yet remain bounded, the folding on the attractor must continue down to arbitrarily small length scales. This complex structure has a non-integer dimension. Chaotic attractors are examples of objects with non-integer dimension. Such objects are said to be fractals.

The fractal dimension is only an extension of the common notion of dimension. A line is considered one dimensional. The boundary of a circle is also one dimensional but can only exist embedded in two dimensions. What definition would fit both circumstances? Suppose the line is covered with N "boxes" (line segments) of size ε and the circle boundary with squares of side ε. If the length of the boxes are divided in half, how many boxes are now required to cover the line and the circle? The answer is 2N. The number of boxes scales linearly with the inverse of the length of a "side" and so both the line and circle boundary are said to

Figure 2.3 Chaotic attractor and Poincaré section for the forced Duffing oscillator. The parameters are: $B = 0.15$, $G = 0.30$, $k = -1.0$, $\omega = 1.0$. (a). Chaotic attractor. (b). Poincaré section of the chaotic attractor. The section is taken as indicated by the straight line in figure(a) and is perpendicular to the page. Notice the folding in each leaf. This structure theoretically continues indefinitely. Notice also the large open regions between layers of folds. This property of a fractal structure is called lacunarity (Mandelbrot,1983, p. 310). This lacunarity is responsible for some inaccuracy in the dimension calculations as discussed in the section on the Grassberger-Procaccia dimension.

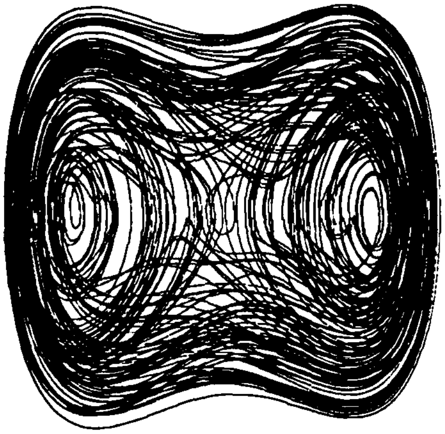

(a) Duffing attractor

(b) Poincare section

be one dimensional. If the circle itself were covered with boxes halving the side of a box would mean that four times as many boxes were needed. The number of boxes scales as the square of the inverse of the length of a box side and the circle is said to be two dimensional. This may be generalized as:

$$d_c = \lim_{\varepsilon \to 0} \frac{\log N(\varepsilon)}{\log(1/\varepsilon)} \tag{2.8}$$

where, if the set is embedded in p-dimensions, $N(\varepsilon)$ is the minimum number of p-dimensional cubes of side ε needed to cover the set. In the literature d_c is known as the capacity and is one of several types of dimension. A discussion of several of these types of dimension is included in a latter section. As an example of a fractal set, one may take the Cantor 1/3 set. That is, one takes a unit line segment and removes the middle third. Now the middles of the outer two segments are removed and this process is continued ad infinitum. The remaining set is the Cantor set. To find the dimension, the set is covered by boxes (line segments). One now uses smaller and smaller boxes and counts the number of boxes necessary to cover the set. At each stage the box size is reduced by 1/3 the previous value. The box size, ε, scales $(1/3)^n$ and the number of boxes necessary to cover the set goes as 2^n, so letting n go to infinity (which in this case is the same as letting ε go to zero), the dimension is seen to be log2 / log3.

One manifestation of the fractal nature of chaotic attractors is that the flow on the attractor will be aperiodic. So a frequency spectrum from a system in chaotic motion will be broad-banded with perhaps broad peaks. This will look like a signal from a periodic or quasi-periodic system interacting with noise. Yet, there is a difference. For a chaotic system, the motion is deterministic in principle and the motion in phase space is confined to a low-dimensional attractor. The continuous frequency spectrum results from the dynamics. For a signal with noise, the noise is random and results from some stochastic process beyond that which gives rise to the signal. Since it is random, the noise will fill out what ever phase space is available and so will appear to have a dimension equal to the embedding dimension.

Now it can be seen that there are several characteristic properties for chaotic motion. Trajectories for chaotic motion will be sensitive to initial conditions and so will have at least one positive Lyapunov exponent associated with them. The attractor to which the trajectories are asymptotically stable will have a complex topology and have a low, fractal dimension. A frequency spectrum of the motion on one of these trajectories will be broadbanded. This last property has been shown to be insufficient by itself to identify a motion as chaotic.

2.4 The Taylor-Couette system

States in the Taylor-Couette system exhibit many of the properties discussed above for nonlinear, dissipative, driven systems. The most convenient way of illustrating this is to discuss the transitions which occur with increasing inner cylinder Reynolds number starting with Couette flow. For the discussion here the outer cylinder will be considered to be stationary. The particular values of the Reynolds numbers are for a radius ratio of .875 and an aspect ratio of about 20. For parameter values other than these the scenario could be different.

The first flow obtained upon rotating the inner cylinder is Couette flow, which is described in chapter 1. It is a featureless, time independent flow and corresponds to a fixed point. This is schematically shown in figure 2.4(a). Next a transition is made at the critical Reynolds number (R_c) to Taylor vortex flow (figure 2.4(b)), breaking the axial symmetry. This is a stable, time independent state and also corresponds to a fixed point. The figure shows two points which reflect the fact that Taylor vortex flow is doubly degenerate for a given axial wavelength. In general there will be several pairs of points as several states with different axial wavelengths are usually stable simultaneously.

Upon increasing the Reynolds number still further a transition is made to wavy vortex flow at about $R = 1.3\ R_c$ (figure 2.4(c)). With transition to this state azimuthal symmetry is broken. This is a time periodic state and therefore a limit cycle (attractor dimension of 1). As mentioned above (though not shown) there is a pair of these attractors as the state is doubly degenerate. Often there are several pairs which are simultaneously stable with different axial and/or radial wave lengths. In general this will be true of all states with higher inner cylinder Reynolds numbers.

Figure 2.4 The route to chaos in Taylor-Couette flow (a). Stable focus. This represents the time independent Couette flow. (b). Taylor-Couette flow. There are now two stable foci as discussed in the previous chapter in the section on bifurcation theory. There will actually be more stable states than this since there may be stable states with different axial wavelengths. (c). Wavy vortex flow. This state is time dependent and so is shown as a limit cycle. As in Taylor-Couette flow there may be many stable states with different axial and azimuthal wavelengths though only one state is shown. (d) Modulated wavy vortex flow. The second frequency is represented by motion about the minor axis of the torus. The frequencies are independent and incommensurate. If mode locking were allowed the orbit would eventually repeat itself and so only be periodic instead of quasiperiodic. Such behavior is forbidden by the azimuthal symmetry of the Taylor-Couette system (Rand, 1981). (e) Chaotic flow. Notice that the attractor roughly resembles the quasiperiodic torus but is "fuzzier" due to the folding.

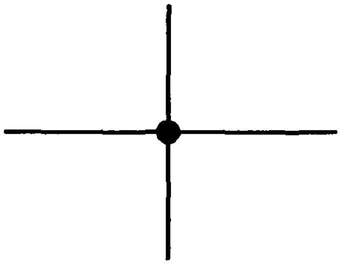

Fig 2.4(a) Couette flow

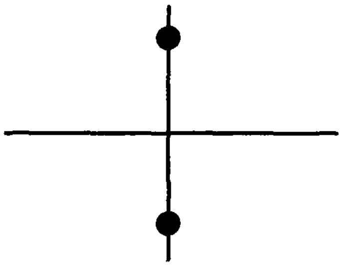

Fig. 2.4(b) Taylor Vortex flow

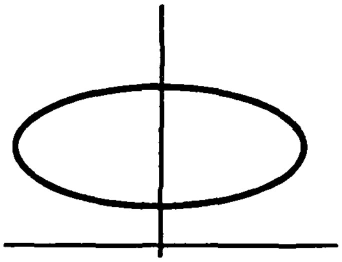

Fig. 2.4(c) Wavy vortex flow

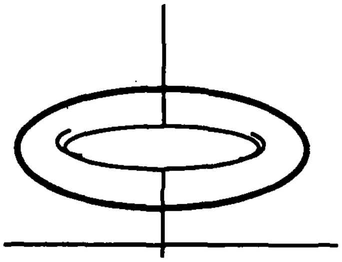

Fig 2.4(d) Modulated wavy vortex flow

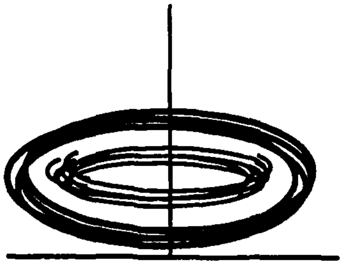

Fig 2.4(e) Weak turbulence

Depending on the axial and azimuthal wavelength, the state may become unstable as the inner cylinder Reynolds number is increased and the system may spontaneously change wavelength. There is one sharp frequency associated with the motion (which depends on the azimuthal wavenumber) though usually several harmonics are present.

A further increase in Reynolds number leads to a transition to modulated wavy vortex flow at about $R = 10\ R_c$ (figure 2.4(d)). This state has two frequencies associated with it and the flow is on a torus (the dimension is 2). There is no frequency locking associated with the two frequencies because of the circular symmetry of the Couette system (Rand, 1982). The actual torus does not appear as the nice "doughnut" shown in the figure but is distorted by the nonlinearity. Actual figures of the torus may be found in chapter 5.

As the Reynolds number is increased still further the transition is made to weak turbulence. The calculated dimension increases to about 2.5 at $R/R_c = 11.8$. The largest Lyapunov exponent becomes positive at about this Reynolds number. The frequency has a continuous background due to the fact the motion is aperiodic and the flow is chaotic. The figures of the reconstructed attractor show that it becomes fuzzy denoting that it is no longer smooth (simulated in figure 2.4(e)). The Poincaré sections show a thickening due to the development of a folded structure but the resolution of the experiment was insufficient to resolve the folding (Brandstater, 1984).

If the outer cylinder Reynolds number is small enough ($\Omega_1/\Omega_2 < -0.78$) then the second transition is to spiral vortex flow instead of Taylor vortex flow. Spiral vortex flow is periodic so for this situation the second time independent state does not appear. Also the quasi-periodic state will be wavy spirals instead of modulated wavy vortex flow.

2.5 Manifestations of the real world

How are the various measures of chaos computed? The most straightforward way to compute the various quantities is from the definition. Sometimes it may be more convenient or practical to perform a calculation using a variant definition of the original quantity or to calculate some related quantity instead. This section is a guide to the real world of computing quantitative properties of chaos.

2.5.1 Attractor reconstruction

How is the attractor constructed from the experimental data? From the above discussion it appears that as many experimental parameters would have to be measured as the embedding space of the attractor. Experimentally it is hard enough to measure one parameter as a function of time. Usually, the experimental data are in the form of a time series of measurements for a single parameter. Fortunately, the attractor can be reconstructed from a time series taken at a single point because of the "embedding theorem" of Takens (Takens, 1981). The embedding theorem states that one can construct vectors, say of dimension m, out of the time series by taking the parameter values at time delays,say τ:

$$V_i = (x_i, x_{i+\tau}, x_{i+\tau}, \ldots, x_{i+(m-1)\tau}) \qquad (2.9)$$

For m large enough, these vectors will span a subspace such that the reconstructed attractor will have the same dimension as the original attractor (Theiler, 1984). The number "m" is called the embedding dimension and obviously needs to be larger than the attractor dimension. Typically, in determining an attractor dimension from experimental data, m is increased on successive calculations until the calculated attractor dimension converges. So, a multi-dimensional attractor can be reconstructed from a time series of a single variable and the dimension of that attractor determined.

Attractors are constructed from time delay vectors using the embedding theorem. In practice the time delay vectors are derived from the time series and stored separately so the result is a series of vectors of the embedding dimension stored in chronological order. If the attractor is to be used in a dimension calculation, it is reconstructed several times, each time with a larger embedding dimension. Once the embedding dimension is large enough, the dimension of the attractor as calculated by one of the algorithms below no longer increases as the embedding dimension increases. This asymptotic value of dimension is assumed to be the attractor dimension. This dimension is usually the average of from several hundred to several thousand calculations for a given set of parameters. If the reconstruction of the attractor is to be used for graphics such as a figure in a paper, then the attractor is usually reconstructed in a 3-dimensional space and a 2-dimensional projection made from it.

2.5.2 How to pick a time delay (mutual information)

An interesting question is how to choose the time delays for an attractor reconstruction. From a theoretical point of view it should not make any difference. From a practical point of view it is immensely important. The problem is caused by the noise and finite resolution of any set of experimental data. Each measurement has some finite number of bits of precision.

How does this affect the time delay? If the time delay is too short then one vector is too much like the vectors before and after it in time. This means the attractor structure will only be represented by a small difference between the vectors. This small difference may be smaller than the noise level or at least not allow enough scaling range in the phase space for the asymptotic value of the dimension to be determined. If too large a delay is chosen, the vectors may also be less independent. This is due to the fact that motion on the attractor is ergodic and for too large a delay the degree of dependence of any two consecutive vectors will be more or less random.

A logical choice for choosing the time delay is to chose a minimum of the autocorrelation function. However, the dynamical systems of interest are nonlinear and a minimum in the autocorrelation only chooses linear independence. A more general independence is needed. It was suggested by R. S. Shaw that the first local minimum of a quantity known as the mutual information might serve as such a measure of independence. This idea has been studied in depth by Andrew Fraser of the Center for Nonlinear Dynamics at the University of Texas at Austin who has found this to be the case (A. Fraser, to be published, Fraser, Swinney, 1986,).

The mutual information is an information theoretic concept. Because of the sensitivity on initial conditions of motion on an attractor and the fact that any specification of the initial conditions will have finite resolution, the ability to determine the initial state is lost after some finite length of time. The specification of the initial state is the information. Now consider two measurements, S and Q, the results of which will be recorded in binary. The mutual information of these two measurements is the number of bits which can be predicted about Q given S, on the average. Thus the correct time delay is the delay which minimizes the this number. As mentioned above, the time delay corresponding to the first local minimum in the mutual information is chosen. So this time delay is computed from the experimental data before the attractor is constructed.

2.5.3 Poincaré sections by computer

Once an attractor is generated it is possible to cut it with a surface one dimension smaller than the embedding dimension such that the attractor trajectories are more or less perpendicular to the surface. The locations of the intersections of these trajectories with the surface is the computational analogue of the Poincaré section. Since this is primarily a graphical aid, the reconstructions of the attractor are done in three dimensional space and the surface will be a plane. Strictly speaking this surface is not a Poincaré section since a Poincaré section is locally perpendicular to the trajectories and a surface perpendicular to the trajectories across the attractor will not in general be a plane. Still there is a topological equivalence and invariant quantities calculated from the surface will be the same as those for the actual Poincaré section. Also the trajectories used are not the actual trajectories since the attractor is really constructed of points. In practice, chronologically consecutive points which lie on opposite sides of the plane are connected by lines. The intersection of these lines with the plane give the computed Poincaré section. Since the lines will not have the actual curvature of the trajectories the constructed Poincaré section will be thicker than the actual section. This will add to the width of "Poincaré sections" of tori and limit cycles which will already have some width due to the experimental noise. It will also tend to smear any folding which might occur and would otherwise be visible in the section. So, this method will give a figure which approximates the Poincaré section though some of the details will be lost. In chapter 5, the figure resulting from this method will be referred to as a Poincaré section without qualification.

2.5.4 Lyapunov exponent calculations

Lyapunov exponents may also be calculated from experimental data. The Wolf method was used to calculate the Lyapunov exponents for this dissertation. The Wolf method uses the definition of the Lyapunov exponent as the algorithm for the computation. Assume first that there is only one positive Lyapunov exponent, λ_1. A point, x_0, and its nearest neighbor, y_0, are chosen which are separated by some distance J_0. Temporally consecutive points of both x_0 and y_0 are followed until the separation is greater than some preset distance, ε. This ε keeps the separation "infinitesimal" so the definition of Lyapunov exponent is valid. The points where this occur are x_0' and y_0' and the separation is J_0'. Now, a new point x_1 is chosen using either the criterion that the point lies as nearly as possible along the vector defined by x_0' and y_0' and less than ε or, barring that, is the nearest neighbor of y_0'. Now y_0' and x_0' are relabeled to be y_1 and $x_1$and the distance between x_1 and y_1 to be J_1. The above process is repeated until there are no more data points. If Δt is the time between the start and end point of the process given above, N is the total number of time steps in the procedure, and M is the number of times a new x_i has to be chosen, it is easily seen that the Lyapunov exponent is given approximately by:

$$\lambda_1 = \frac{1}{N\Delta t} \sum_{i=0}^{M-1} \log_2 \frac{J'_i}{J_i} \qquad (2.10)$$

This procedure may be generalized in principle to any number of Lyapunov exponents but becomes unwieldy for more than two (Vastano, Kostelich, 1986).

2.5.5 Dimension Calculations

There are many different types of fractal (noninteger) dimensions. Examples are the fractal dimension, the dimension of the natural measure, the correlation dimension and a dimension derived from the Lyapunov exponents, the Lyapunov dimension. An example of the fractal dimension is the capacity which was defined in an earlier section. In a calculation of the capacity, all of the cubes containing parts of the attractor are equally important, even if that portion is only rarely visited. This has important implications in the determination of the attractor dimension from experimental data (Farmer, Ott, Yorke, 1983).

The next dimension mentioned was the dimension of the natural measure. A property of dimensions of the natural measure is that the importance of the cubes used to compute the dimension is weighed by the fraction of time which the trajectory spends in that cube. If almost every trajectory spends the same fraction of time in that cube then that fraction is called the natural measure. These dimensions are more important in determining the attractor dimension from experimental data then the fractal dimension since one only needs data in the most important cubes. A good example is the pointwise dimension. It is the power by which the natural measure changes as the radius of a ball containing part of the attractor tends to zero. Let the natural probability measure on an attractor be μ. Let $B_\varepsilon(x)$ denote a ball of radius ε centered about a point x on the attractor. The pointwise dimension is defined as:

$$d_p(x) = \lim_{\varepsilon \to 0} \frac{\log \mu(B_\varepsilon(x))}{\log \varepsilon} \qquad (2.11)$$

It is usually assumed that $d_p(x)$ is independent of x for almost all x and so is simply written: d_p. Provided there are enough data points then the regions where the natural measure is larger contains more points. So the pointwise dimension may be computed as the power by which the number of data points in the ball, B_ε changes as the radius ε tends to zero.

A third type of dimension mentioned in the introduction was the correlation dimension. One particular algorithm for computing the correlation dimension is the Grassberger-Procaccia method (Grassberger, Procaccia, 1983). In order to derive the algorithm for the correlation dimension, Grassberger and Procaccia first define a correlation integral. The definition is (Theiler, 1984):

$$C(r,N) = \frac{2}{N^2}\sum_{n=1}^{N}\sum_{i=1}^{N-n} H(r - |x_{i+n} - x_i|) \qquad (2.12)$$

where $\mathbf{x}_i$ is the location of the ith data point and H is the Heaviside step function. This is basically the probability of finding a pair of points in the data set with a nearest neighbor distance less than r. The correlation dimension is the exponent by which the correlation scales as r goes to zero:

$$\nu = \lim_{r\to 0}\lim_{N\to\infty} \frac{\log C(r,N)}{\log r} \qquad (2.13)$$

Actually, these first three examples are the first three members of integer order of a set of generalized dimensions (Hentschel, Procaccia, 1985). The definition of the generalized dimension is:

$$d_q = \frac{1}{(q-1)}\lim_{\varepsilon\to 0}\frac{1}{\log \varepsilon}\int \mu(B_\varepsilon(x))^{q-1}d\mu(x) \qquad (2.14)$$

where the q is the order of the dimension and the other symbols have been defined above. For the limit as q approaches 0 the fractal dimension is obtained, for the limit as q approaches 1 the dimension of the natural measure is obtained and for the limit as q approaches 2 the correlation dimension results. Though this definition is valid for non-integer values of q, it appears that only the dimensions defined for integer values of q have a physical meaning (Hentschel, Procaccia, 1985). In general, $d_{q'} \leq d_q$ for any $q' > q$ and so d_∞ is a lower bound for the dimension and so all dimensions are bound between d_0 and d_∞.

The fourth dimension was the Lyapunov dimension. This dimension is not part of the hierarchy mentioned above but is conceptually different. This dimension actually relates the dynamics of spreading on the attractor to the metric properties of the attractor itself. The Lyapunov dimension is defined in terms of the Lyapunov numbers as:

$$d_L = k + \frac{\log(\lambda_1 \lambda_2 \ldots \lambda_k)}{\log(1/\lambda_{k+1})} \tag{2.15}$$

where k is the largest value for which $\lambda_1 \lambda_2 \ldots \lambda_k \geq 1$. A connection may be made between the geometric and dynamic properties of the attractor by using the Kaplan-Yorke conjecture. The Kaplan-Yorke conjecture consists of the above definition plus:

$$d_\mu = d_L \tag{2.16}$$

for a "typical" attractor where d_μ is the dimension of the natural measure. The Kaplan-Yorke conjecture is not true in general but it is assumed to be true for all attractors associated with physical systems (Farmer, Ott, Yorke, 1983).

Several algorithms have been used for calculating the dimension from experimental data. One is the box counting algorithm which essentially determines the capacity of the attractor. The others of particular note are the Grassberger-Procaccia algorithm and the Badii-Politi algorithm which determine the correlation dimension.

2.5.5.1 Box counting

The capacity of a geometrical object is defined above. The definition is turned into an algorithm by simulating the limiting process for some finite range and assuming the trend asymptotically approaches the correct answer. To this end, the attractor is covered with boxes. The number of boxes needed, N_i, are counted and both that number and the length of a side, ε_i, are recorded. If V is the volume of the attractor, the definition of the capacity, for small enough ε, can be rewritten as:

$$\ln N = C \ln(1/\varepsilon) + \ln V \tag{2.17}$$

By plotting ($\ln N_i$) vs ($\ln \varepsilon_i$) for small enough values of ε_i, the capacity may be determined as the slope of the curve.

Unfortunately, some points on the attractor have very low probability of being visited yet they must be counted in order for the dimension to be computed correctly. But there must be a large number of data points over the range of ε_i used to compute the slope. This means a very large number of data points must be taken, usually to the extent that for systems of larger than two dimension the data requirements are prohibitive. A better approach is to use a definition of dimension which involves the probability of a part of the attractor being visited, such as the Grassberger-Procaccia correlation algorithm (Greenside et al., 1982).

2.5.5.2 Grassberger-Procaccia

The Grassberger-Procaccia method of calculating of the correlation dimension was given above. The question here is how well it determines the correlation dimension from experimental data. In an experimental situation there are only a finite amount of data. The obvious question is whether there are enough data in practice so that the limits in the definition are well approximated. Or, saying the same thing in a more physical way, is the quantity of data sufficient so that the dimension calculations give the right answer? From experience it appears that the calculation is reproducible. This is certainly a desirable characteristic as it means the determinations can be made precise. The obvious second question is, are the determinations accurate? That is, how close are they to the correct answer?

Part of the answer may be found in a paper by Kostelich and Swinney (Kostelich, Swinney, 1987). In this paper they calculated the Badii-Politi and the Grassberger-Procaccia dimensions for the Mackey-Glass equation (the Badii-Politi algorithm will be discussed in the next section). The Lyapunov dimension of the Mackey-Glass attractor depends on the coefficients and can be calculated independently of the Grassberger-Procaccia and Badii-Politi algorithms. So the results of the algorithms may be checked against the correct value (assuming the Kaplan-Yorke conjecture holds) of the dimension. The comparison of the dimension determined by the Grassberger-Procaccia algorithm with the correct values shows that for low dimension ($d \leq 3$) the algorithm gives the correct answer for 250,000 data points.

For larger dimensions ($d > 3$) the Grassberger-Procaccia algorithm gives a value for the dimension which is consistently too small. To understand this it is necessary to explain how the dimension is determined. First, the correlation is calculated from equation 2.12 for a given point on the attractor at a given upper limit of the nearest neighbor distance, r. Then r is reduced and the correlation is calculated again. This procedure is continued over the range of available data. Another point is chosen on the attractor and this procedure is repeated. After several hundred trials the results for a given r are averaged together. Then the logarithms of both are taken and plotted. The slope of the resulting line should be the correlation dimension.

Unfortunately, the result is not usually a straight line. For large enough ε the attractor looks like a point attractor and the dimension is zero. In practice, the upper limit of the scale is half the attractor diameter so this domain is never seen. In the case of weakly chaotic Taylor-Couette flow, the attractor is a wrinkled torus. So, as the ε approaches the size of the attractor, the wrinkles are not seen and the dimension appears to be 2. Once the folding on the attractor can be seen, the dimension is the correct dimension of the attractor (say 2.5). Figure 2.5(a) is part of a plot of the correlation against the radius, ε. The slope representing the attractor dimension actually lies between -2 and -4 on the $\log_2 \varepsilon$ axis. The part of the slope between -1 and -2 is actually greater but may be due to oscillations in the scaling of the correlation which is explained later in this section. If infinite, noiseless data were available then this dimension would remain the same as ε became smaller. Of course, all experiments will have some noise distributed about the actual values. Assuming this noise is random, then it will fill out the embedding space. Thus, at the lowest scales the attractor will appear to have the dimension of the embedding space. This is seen in the increasing slope between -4 and -6. Figure 2.5(b) is a plot of the local slope of the curve in 2.5(a) averaged over 4 points. The oscillation between -1 and -2 and the increase in slope as the noise becomes important are more obvious in this plot.

The oscillation seen in the first part of figure 2.5(a) and 2.5(b) is the reason why the Grassberger-Procaccia algorithm underestimates the dimension. A paper by

Figure 2.5(a) Grassberger-Procaccia correlation function vs. radius. The attractor from which this data is taken was reconstructed in an 8 dimensional embedding space with a time delay of 19 sampling points as determined from a calculation of the mutual information vs. time delay. This plot represents an actual calculation for the correlation function vs. the radius of the sphere used to limit the distance between points in determining the correlation. Notice that the slope appears approximately constant until $\log_2 \varepsilon$ reaches -4 then it increases dramatically. (b) Local slope (dimension) vs. radius. This is a plot of the local slope of figure 2.5(a) taken over four points. The local slope should therefore be the dimension. The fluctuations now appear much more pronounced. The small bump at the beginning is probably due to the oscillations discussed in the text. It is assumed that the dimension of the attractor is adequately represented by the minimum of the local slope (dimension) between -2 and -3. The data used for this plot are from a Taylor-Couette experiment with $R/R_c = 14$, an aspect ratio of 24.7 and a radius ratio of 0.862. The actual data file was ccc109 .

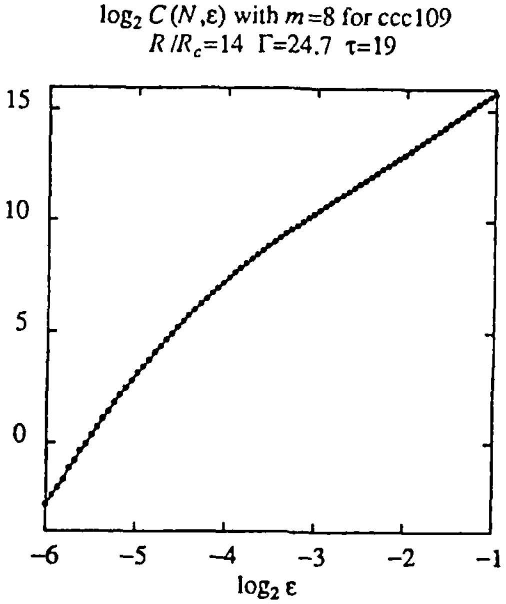

Figure 2.5(a) Correlation dimension vs. radius

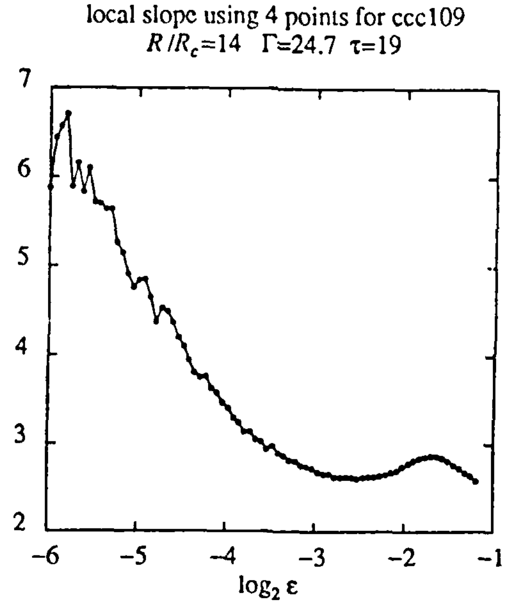

Figure 2.5(b) Slope vs. radius

Arneodo, Grasseau and Kostelich discusses this source of error (Arneodo, Grasseau, Kostelich, to be published). The paper shows that there are oscillations in the slope of the regression line fitted to the data in the log-log plot. These oscillations are due to the lacunarity of self-similar strange attractors. Lacunarity of a self-similar fractal object is due to the fact that in the folded structure there are large empty spaces. Thus, as the correlation scales with r, it "sees" these voids of data and so oscillates. Since the slope is very sensitive to the range of scales used these oscillations lead to large errors in the values of the dimension. All geometric methods for calculating the dimension from experimental data should suffer from these oscillations and so the calculated dimension should be less than the actual value.

2.5.5.3 Badii-Politi

The Badii-Politi algorithm is a way of computing the information dimension (which is another name for d_1). The approach is to look at the behavior of the average nearest neighbor distance as a function of the number of points selected on the attractor. To that end, select a reference point, **x**. Select n-1 other points on the attractor, chosen at random. Now let $\delta(n)$ be the nearest neighbor distance between the point **x** and its nearest neighbor among the n-1 points. One can define a probability distribution, $P(\delta,n)$, of the nearest neighbor distances among n points. The average value of δ for all δ at a given value of n is simply (Badii, Politi, 1985):

$$\langle \delta \rangle = \int_0^\infty \delta \, P(\delta,n) \, d\delta \qquad (2.18)$$

It can be shown that (Badii, Politi, 1985):

$$\langle \delta_n \rangle \propto n^{-1/d} \qquad (2.19)$$

where d is the information dimension. This may be generalized to higher, non-integer moments of δ but is not important here. Because the dominating effect at the smallest scale in experimental data is the experimental noise, the nearest neighbor distance would tend to reflect the dimension of the noise rather than the fractal structure of the attractor. To look at this structure it is necessary to use not the nearest neighbor but the k^{th} nearest neighbor. In practice $10 < k < 300$ for datasets larger than 32k points.

Consider figure 2.6(a). Here the information dimension vs. the nearest neighbor order are plotted for a particular time series from the experimental data. At lowest order the noise dominates and so the dimension is high. As the nearest neighbor order approaches the region such that $10 < k < 300$ the curve tends to flatten out. For this dimension the plot does not appear to approach a limit with the nearest neighbor order. A plot of the information dimension against the embedding dimension clearly shows a limit of about 3.5 however (figure 2.6(b)). The reason for the failure of the information dimension to approach a limit with the nearest neighbor order is not known. Choosing the correct value of nearest neighbor range from which to pick the dimension is based on experience with applying this algorithm to the Mackey-Glass equation.

This algorithm should suffer the same effects of lacunarity as the Grassberger-Procaccia algorithm. This could be a reason for the failure of the algorithm to converge to a value of information dimension with increasing nearest neighbor order. However, the study of Kostelich and Swinney shows that this method gives values of the dimension of the Mackey-Glass attractor comparable to the actual values (within 10%).

2.5.6 Frequency spectra

Practically, due to the sensitivity of chaotic motion to initial conditions, the chaotic motion does not appear to be deterministic. How can chaotic motion be discriminated from random motion? Determination of the attractor dimension is one way to find out if motion is chaotic or random. Simply, chaos is deterministic (strictly speaking) and random motion is not. Chaotic motion does not fill phase space. Random motion will fill phase space. Thus, in reconstructing attractors,

Figure 2.6(a) Information dimension vs. nearest neighbor order. The data used for this plot is from a Taylor-Couette experiment with $R/R_c = 14$, an aspect ratio of 24.7 and a radius ratio of 0.862. The attractor from which this data is taken was reconstructed in an 8 dimensional embedding space with a time delay of 19 sampling points. The dimension is chosen by using a nearest neighbor order of 200. The value of nearest neighbor order is picked by experience from comparing the results of this algorithm with the actually dimensions for the Mackey-Glass equation. (b) Information dimension vs. embedding dimension. In this plot it is easier to see why a dimension of 3.5 is a reasonable choice. The plots approaching the embedding dimension axis are of increasing nearest neighbor order.

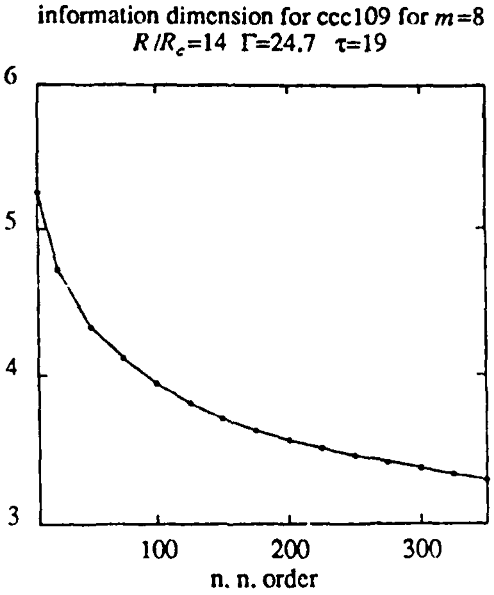

Figure 2.6(a) Information dimension vs nearest neighbor order

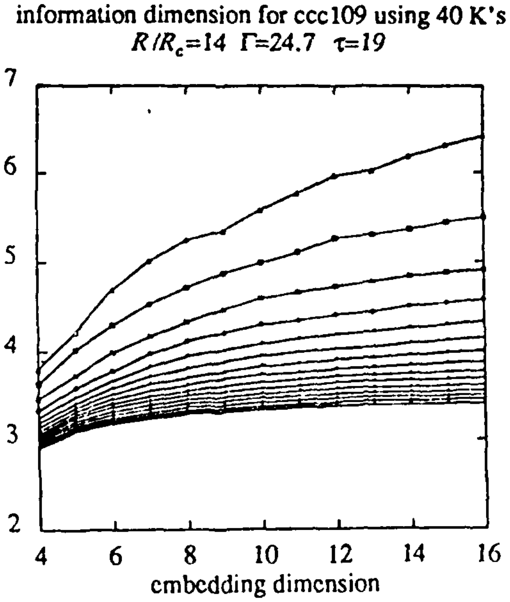

Figure 5.6(b) Information dimension vs embedding dimension

chaotic motion will have a relatively small attractor dimension.

It is also possible to look at the power spectra for evidence to distinguish the two. Basically the spectra from chaotic motion and from stochastic motion are broadbanded. However, the decay with frequency differs for the two. It has been shown that for a nth-order stochastic process the power at high frequencies falls off as a power law $\propto f^{-2n}$. For deterministic equations with infinitely differentiable solutions the spectra falls off exponentially. So, one should be able to discriminate between chaotic and stochastic motion by plotting the power spectrum on a semi-logarithmic graph. Clearly if such a plot yields a straight line or provides a reasonable fit to a straight line, deterministic chaos may be suspected (Sigeti, Horsthemke, 1987).

2.6 Aspect Ratio Dependence of the Attractor Dimension

For any dynamical system there is an absolute upper bound on the attractor dimension or the number of Lyapunov exponents. This is the dimension of the phase space of the system. One property of dissipative dynamical systems is that the dissipation damps many of the degrees of freedom. For example, if the phase space is three dimensional, the attractor dimension must be less than three and there can be at most one positive Lyapunov exponent. This last statement may be seen to be true by considering that the attractor is absolutely stable so there must be one negative Lyapunov exponent associated with the "attraction". There is a zero Lyapunov exponent associated with the relation between different points on the same trajectory since the spreading there is not exponential. Finally, if the attractor is chaotic (or "strange") there will be one positive Lyapunov exponent associated with the exponential spreading transverse to the trajectories. Nevertheless, the solutions may be examined in the full phase space since it is small.

Now, what about dynamical systems described by partial differential equations such as the Navier-Stokes equation? Since the solutions are functions of a continuous range of spatial points there is conceivably an infinite dimensional phase space. In a physical system, this would be limited by the fact that there is a finite number of particles per volume but in fluid mechanics the assumption is that the medium is continuous. The justification of this assumption is that viscosity damps out the fluid motion on a scale much larger than the distance between molecules. Mathematically, the dissipative part of the Navier-Stokes equation must restrict the solutions to a finite dimensional attractor as well if it is to accurately model the physics. For Couette flow, the phase space is zero dimensional. From some initial studies there is some information on how the dimension grows with energy input, or, in particular, how the attractor dimension of Taylor-Couette flow grows with increasing inner cylinder Reynolds number for a limited parameter space (Brandstater, Swinney, 1987). It would be of interest to know how the dimension scales with the size of the system.

Several estimates of this scaling can be made. The first to be considered here is a result from the Kolmogorov theory of isotropic turbulence. In Kolmogorov theory the energy is pumped into the flow at the largest length scale. The energy then cascades to smaller and smaller length scales, the correlation of the motion at a given length scale decreasing very rapidly with respect to motion on larger or smaller scales. Viscosity dominates the flow at the smallest length scales and so terminates the cascade. This smallest length scale is the Kolmogorov length, l_k. Thus, for well developed turbulence where the Kolmogorov scaling would hold, the "modes" would be associated with length scales. The number of modes per unit volume would be the number of cubes per unit volume with a side of length l_k or:

$$n = \frac{1}{l_k^3} = \frac{(R/R_c)^{9/4}}{\Lambda^3} \qquad (2.20)$$

where n is the number of modes, l_k is the Kolmogorov length, R is the Reynolds number at which the number of modes is estimated, R_c is the critical Reynolds number for the transition to turbulence and Λ is a characteristic length of the system of interest (Landau and Lifshitz,1959). The total number would be just n times the fluid volume. For a Taylor-Couette system the number of modes would be:

$$n \times \text{volume} = \frac{R^{9/4}}{d^3}\pi L(b^2 - a^2) = \frac{R^{9/4}}{d^2}\pi(b^2 - a^2)\Gamma \qquad (2.21)$$

where d = b - a, i.e., the gap size, and the other symbols have been defined previously. So, by this estimate, the number of degrees of freedom, and so the dimension, should scale linearly with the aspect ratio. One may use this to calculate the number of modes using some typical dimensions for a Taylor-Couette apparatus (see Appendix A). If the Reynolds number is assumed to be $R/R_c = 20$ and the aspect ratio is assumed to be 20, the number of modes is estimated to be approximately ten billion. Since the measured attractor dimension for Taylor-Couette flow with about the same parameters is on the order of 5 (Brandstater, Swinney, 1987), then the Kolmogorov theory grossly over estimates the number of modes.

This overestimate is not really surprising. Kolmogorov theory assumes there is a large range in length scale where the flow is independent of the geometry of the large scale motion. Most of the modes are contributed by the isotropic modes in the scaling region. This only occurs at very high Reynolds numbers ($> 10^7$ (Tritton, 1977, p.259)). This is not the situation in the range of Reynolds number where this experiment was run. The Reynolds number is only about 2000 and the Kolmogorov length ($d/(R/R_c)^{3/4}$) is only about one-tenth of the characteristic length in the system (the gap size).

The Kolmogorov estimates are based on dimensional analysis. In several papers, D. Ruelle derives some expressions for an upper bound to the density of Lyapunov exponents per unit volume for the Navier-Stokes equation for a large volume system from properties of the eigenvalue spectrum (Ruelle, 1984, Ruelle, 1982). The method, which hopefully would produce a better estimate, is based on upper bounds of eigenvalues for a Schroedinger-type operator, H in the equation:

$$\frac{dv}{dt} = H(v(t))\, v \qquad (2.22)$$

It will be noticed that the Navier-Stokes equation fits this form. The derivation of the relationship is complex and the interested reader is referred to the references. The derived expression for three dimensional flow is:

$$d \leq 0.06 \ \Omega^{2/5} \ \nu^{-9/4} \left\langle \int_{\Omega} \varepsilon^{5/4} \, d\Omega \right\rangle^{3/5} \qquad (2.23)$$

where d is the dimension, Ω is the volume of the system, ν is the kinematic viscosity, ε is the energy dissipation per unit volume, and the average is with respect to the invariant measure on the attractor. If it is assumed that the energy dissipation is constant over the volume of fluid and over the attractor, then the average is just $\Omega\varepsilon^{5/4}$ and the equation becomes:

$$d \leq 0.06 \ \Omega \ \nu^{-9/4} \ \varepsilon^{3/4} \qquad (2.24)$$

The energy dissipation per unit volume can be calculated from the torque and angular velocity if the measurements are available. Otherwise, the energy dissipation may be calculated from the Kolmogorov relation:

$$\varepsilon = (\nu R)^3 \Lambda^{-4} \qquad (2.25)$$

Upon substituting in equation 2.24 :

$$d \leq 0.06 \ \frac{\Omega}{\Lambda^3} \ R^{9/4} \qquad (2.26)$$

This is basically equation 2.21 multiplied by 0.06. Thus, it would not be expected that the estimate provided by this method would give a significant improvement over the Kolmogorov estimate. Some improvement could be made by using the estimates of the dissipation from Frisch's β-model of intermittency in turbulence (Ruelle, 1982) but this would be basically patching a model which is not valid in the domain in which it has been applied. Nevertheless, the functional dependence on the volume may be correct which would imply that the attractor dimension should increase as the aspect ratio increases.

Another approach to determining the number of modes as a function of the volume is presented in a series of papers by Manley, Temam, Treve and Foias (Foias et al., 1983, Foias et al., 1986). An expression for the upper limit to the number of eigenvalues of the Stokes problem is derived. The results are applied to Rayleigh-Benard convection. For long convection rolls, the number of degrees of freedom necessary to describe the system are shown to be proportional to the aspect ratio. The actual number of modes is on the order of ten billion at the onset of turbulent convection. This once again is seen to be an overestimate. These overestimates seem to result from the necessity of using Kolmogorov type arguments to obtain estimates of the energy dissipation or of the smallest length scales of dynamic importance in the flow. These estimates are applicable only for the Reynolds number becoming arbitrarily large. Still, the prediction is for a linear dependence of the attractor dimension on the aspect ratio.

Another reason for thinking that the number of modes might increase would be the analogous behavior of non-linear differential equations with dissipation. Since the fluid motion is presumably governed by the Navier-Stokes equation, this might be a reasonable approach. The key to such a study would be to choose an equation showing spatiotemporal chaos but was simple enough to study indepth numerically. A study along these lines was done by Y. Pomeau, A. Pumir and Pelce (Pomeau, Pumir, Pelce, 1984). These authors studied the behavior of a one-dimensional equation with time dependence: the Kuramoto-Shivashinsky equation. This equation has been used in previous studies of the propagation of flame fronts and is:

$$\varphi_t + \varphi\varphi_x + \varphi_{xx} + \varphi_{xxxx} = 0. \tag{2.27}$$

This is an equation with non-linearity (second term), a term for energy input to the system (third term) and dissipation (fourth term). The relation between the order of the terms and their function is different in the Kuramoto-Shivashinsky equation and in the Navier-Stokes equation. Nevertheless, both equations represent driven, nonlinear, dissipative systems. The function of the terms in the Kuramoto-Shivashinsky equation was obtained by deriving an energy balance equation, using the boundary conditions given below and demanding that the energy is pumped in at the largest length scales and dissipation occurs at the smallest. The chosen boundary conditions were:

$$\varphi = \varphi_x = 0 \quad \text{at } x = 0 \text{ and } x = L \tag{2.28}$$

where L is the length of the support (that part of the x-axis where φ was non-zero) of the equation. To increase the "volume" of the system, the authors increased "L". The quantity of interest here was actually the number of positive Lyapunov exponents but the dimension of the attractor for the system should increase similarly. A comparison of the behavior of solutions to the Kuramoto-Shivashinsky equation with the theoretical behavior of developed turbulence revealed some interesting analogies. For solutions of the Kuramoto-Shivashinsky equation with sufficiently many positive Lyapunov exponents, the k spectrum of the states exhibited both a power law range ($\propto k^{-4}$) and a dissipative region at large enough wave vector above the scaling region. This resembled the inertial scaling range in developed turbulence. The number of Lyapunov exponents themselves scaled with the length L as:

$$N(L) = 0.14\,L - 1.5 \tag{2.29}$$

where $N(L)$ was the number of positive Lyapunov exponents as a function of L. The authors pointed out that the number N reached zero at $L = 11$ which was more or less the value for the onset of "turbulence" for this system. They also mentioned that the number of positive Lyapunov exponents grew more slowly than the number of linearly unstable modes which grow approximately as L/π. Thus, there is a well defined threshold in the system beyond which the system is chaotic and the chaotic flow tends to be low dimensional. Similar qualitative behavior would be expected for solutions of the Navier-Stokes equations if weak turbulence was a low dimensional phenomenon. This again would support the argument that the attractor dimension should increase with the aspect ratio.

Thus, it is seen that theoretical estimates of the aspect ratio dependence of the attractor dimension are possible. The methods of using Kolmogorov theory and bounds on the eigenvalues of various differential equations yield numbers that are much too large to be realistic. Still, the scaling of the dimension with aspect ratio may be correct. This agrees with the modelling using the Kuramoto-Shivashinsky equation in that both techniques imply that the attractor dimension should increase as the aspect ratio increases (indeed, both predict a linear dependence which, however, is probably due to the large number of predicted modes).

3. Experimental Details

3.1 Introduction

The experiments conducted for this dissertation consisted of various measurements of flow parameters of fluid in a Taylor-Couette apparatus. The basic description is given in chapter 1 where the boundary conditions are discussed. In this chapter the particular pieces of apparatus are described. These are the Gorman and Hirst systems as described below. Several techniques used for data collection are also discussed.

One technique used in the bifurcation study was observation by eye of the qualitative changes in state of the fluid. The flow patterns were made visible by the aid of flow visualization (Kalliroscope) flakes (Matisse, Gorman, 1984). These flakes aligned with the shear in the flow velocity field and so revealed flow features. Also in the bifurcation study the frequencies in the flow were obtained by Fourier transforming time series of the fluctuations of laser light reflected from the visualization particles in the flow. Pictures of the flow states were taken along with established fiducial marks so that the axial wavelengths could be measured.

A variety of measurements were made in the aspect ratio dependence study as well. The primary measurement was of the radial component of the fluid velocity at a point. This was done by laser Doppler velocimetry (LDV) using a sophisticated system to collect data and also control various experimental parameters. Since there was no flow visualization in this experiment the wavelength of the flow had to be measured using the LDV system as well.

A variety of subsidiary measurements had to be performed to support both experiments. The main example of this type of measurement was of the kinematic viscosity of the working fluids. In all a wide variety of experimental techniques were required to support this research.

3.2 The bifurcation experiments

The Couette system used in the bifurcation experiments was an apparatus designed and built by a previous research associate, Dr. Michael Gorman. A picture of this system appears in figure 3.1. It consisted of an inner cylinder of blackened brass and an outer cylinder of glass, which could be rotated independently. The cylinders were housed in a plexiglas bath so the temperature could be regulated by controlling the temperature of the water entering the bath. The water was pumped through the bath by a NESLAB circulator which maintained the temperature to within 0.01 ^{0}C. The temperature was measured by a mercury thermometer inserted in the bath. The cylinders were driven through toothed belts and sprockets by Compumotor stepper motors which had a resolution of 25,000 steps per rotation. The motors were controlled by a PDP 11/23 computer which also recorded any time series taken and maintained an experimental parameter file.

3.2.1 DEC 11/23 computer control and data acquisition system

The experiments to study the primary and secondary bifurcations for counter-rotating cylinders were controlled with a DEC PDP 11/23 with digital I/O and an ADAC interface for analog to digital conversion. The motors were controlled via the Compumotor bus boxes, designed and built in the Center for Nonlinear Dynamics. The Compumotor indexers had inputs at the back for computer control of velocity, acceleration, position, direction, start, stop,etc. These inputs were latched only upon a start pulse being received. The Compumotor bus boxes were designed to utilize these inputs and adapt them to be compatible with the outputs of the standard TTL I/O. Basically the velocity and acceleration bits (BCD) were TTL compatible and were simply fed straight through to the indexer from the computer output. The start,stop, direction bits however took negative logic and required open collector outputs. To this end, buffer inverters with open collector outputs were added for those particular bits. To take advantage of the latching of the data on a start pulse, a four bit decoder was added. Thus, the Compumotor bus boxes could be arranged in parallel on the same bus; only the box addressed by the four address bits would pass the start pulse and so latch the data on the bus. This way the

Figure 3.1 Gorman Taylor-Couette System. This is the Taylor-Couette system used in the bifurcation experiments. On the left side of the photograph the cylinders are clearly visible. The flow state at the time of the picture was Taylor-Vortex flow. The tubular objects pointing toward the middle of the outer cylinder are the Helium-Neon laser (longer of the two tubes) and the photodetector used to obtain the power spectra. The rectangular object in the center of the picture is the structure which held the Compumotors which drove the cylinders. One of the motors may be seen at the top of the structure, as can the drive belts from the motors to the sprockets on the ends of the cylinders. On the right is the Endocal (NESLAB) RTE-9 bath and circulator which maintained the temperature in the thermal bath surrounding the cylinders. Below the bath are two circuit boards. These boards are the indexers which provided the stepping pulses to the Compumotors. The ribbon cables disappearing off to the right of the photograph go the DEC PDP 11/23 computer which controlled the experiment. Visible at the far left (on the floor) is the cathetometer used to measure the fiducial marks on the cylinders in determining the axial wavelengths of the various flows.

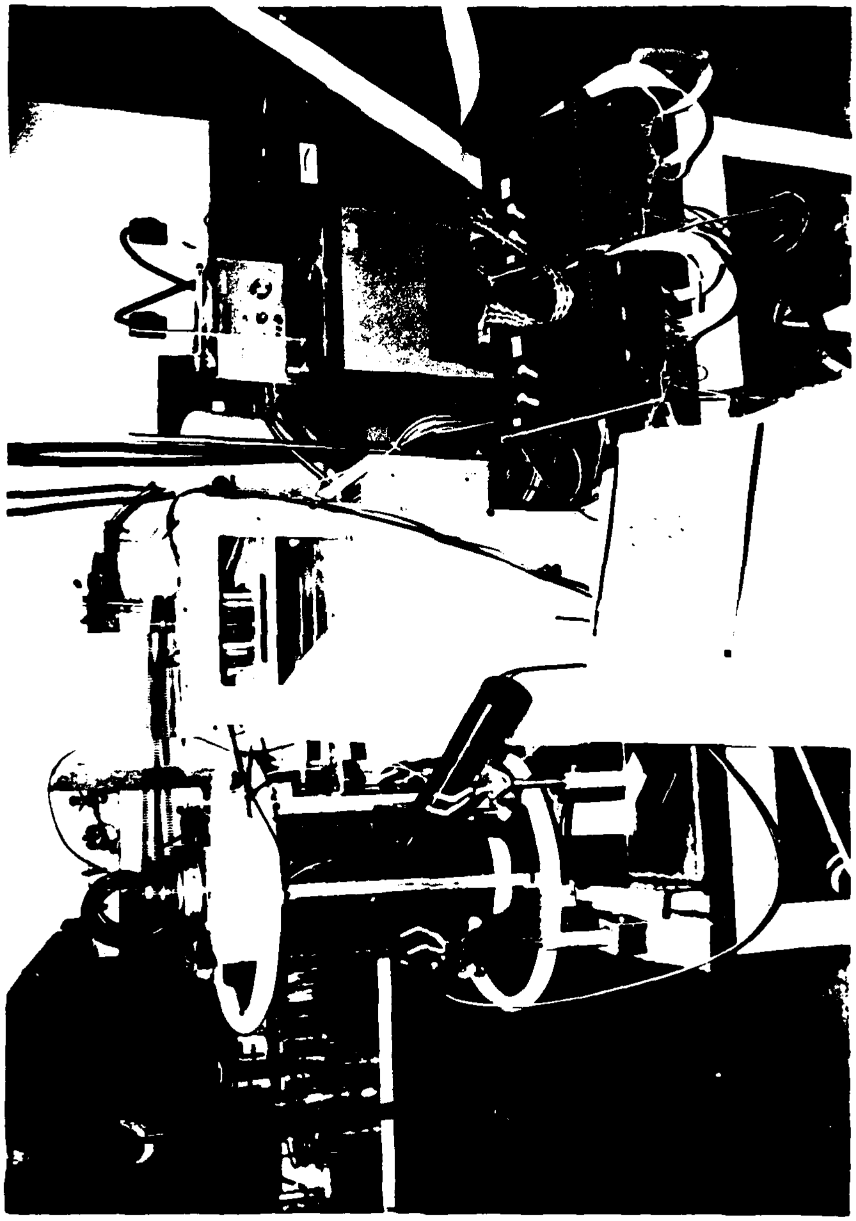

Figure 3.1 Gorman Taylor-Couette System

individual motors could be addressed by software from the single bus.

Yet another capability was added in the "divide by 10" boxes. These boxes made it possible to divide the pulse rate out of the indexer by 10, thus increasing the possible resolution of the motor at the slower speeds. Of course the highest velocity obtainable was 1/10th that obtainable without the boxes but the higher speeds were not necessary at the Reynolds numbers at which the bifurcation experiments were run. The "divide by 10" boxes were enabled or disabled from the computer by an additional bit. All the experiment control and data acquisition software for this experiment was written by Dr. Randy Tagg in the Center for Nonlinear Dynamics.

Higher motor speeds were required in the aspect ratio study than in the bifurcation study and this led to a problem. The Compumotor Model 172 indexers used in the aspect ratio experiment allowed setting the external thumbwheel switches or inputting a BCD velocity signal to velocities which corresponded to pulse rates higher than the indexer internal oscillator could produce reliably. There was no obvious indicator of error from the indexer. However, the problem revealed itself when transitions to various flow states did not appear at the correct Reynolds number. It was tracked down by timing rotations of the Compumotor shaft with a stop watch. The problem was easily fixed by not using the "divide by 10" boxes in the aspect ratio experiment. This points out the need to check parameters which should "obviously" be correct during experiments.

3.2.2 Frequency spectra of the light intensity

The frequency spectrum of the flow was obtained by scattering laser light off of Kalliroscope particles in the flow (Savas, 1985). The light was modulated by the changing pattern of the Kalliroscope flakes. The reflected laser light was focused onto a photodiode and the resulting signal was fed into an analog to digital converter, the digital results of which were fed into a computer. The computer then calculated the power spectrum of the reflected light intensity using a Fast Fourier transform. From this was determined the peak spectral locations and intensities, the background noise. This information as well as a plot of the frequency spectrum was printed. From this data the wavespeed of singly and doubly periodic flow could be determined. The wavespeed is, as defined in Appendix D, simply the ratio of the primary frequency resulting from the flow divided by the inner cylinder frequency. Since the wavespeeds change discontinuously from one state to the next, monitoring the wavespeed was also a good way of observing a transition (King et al., 1984). This was particularly true for the transition between the spiral states m=2 and m=3. The pitch change in the spirals of the flow was not particularly noticeable to the eye and monitoring the wavespeed made for a much more accurate determination.

3.2.3 Wavelength measurements

One of the values measured in the bifurcation experiments was the axial wavelengths of the various flows. For Taylor vortex flow this could have been done with a cathetometer. A cathetometer is a telescope mounted on a vertical post. The telescope is mounted on a slide which has a vernier which can be read against a scale etched in the post. The foot of the cathetometer is three-legged and may be adjusted so the post is parallel with the gravitational field. So the distance between vortices could have been measured by adjusting the cross-hairs of the telescope onto the boundary and recording the position and then moving the slide and repeating the procedure. The difference between every pair of vortices would have been the axial wavelength. This procedure was not used due to the fact that it would not have been possible to measure the wavelength of time dependent flows this way.

The actual procedure used was to take measurements from a picture of the flow. The scaling of the picture was done by measuring the distance between the top and bottom ends of the flow with the cathetometer and comparing it to the distance between the ends of the flow on the picture . The scaling was the ratio of the two measurements. The axial wavelengths were measured by placing a comparator on the photograph and reading off the distance from the scale. A comparator is a magnifier with a scale placed so the picture and the scale are imaged in the same place and with the same magnification. In this way it was possible to directly measure distance to a tenth of a millimeter on the photograph. Actually the largest distance between the flow boundaries that would fit on the scale were measured to reduce the error. The comparator was moved up and down the photograph to obtain between 10 and 20 measurements and the results were averaged to obtain the final value. This resulted in standard deviations of about 1 percent that were mainly due to the difficulty of determining the location of the boundaries on the photograph. It is not clear whether the diffuse nature of the boundaries under magnification was due to poor (grainy) photographic material (Polaroid pictures) or to resolution of the Kalliroscope particles frozen in motion.

3.2.4 Experimental procedure for the bifurcation study

The thrust behind the bifurcation experiments was to locate the bifurcation boundaries and investigate the changes in the states as bifurcation boundaries were crossed. The parameters of importance were the radius ratio, aspect ratio, inner and outer Reynolds numbers and fluid viscosity. In all these experiments the radius ratio was fixed at 0.80 (inner radius/outer radius). The aspect ratio (ratio of axial length of fluid to the gap between cylinders) was 28.75. The fluid used was a mixture of 60% glycerine, 39% water and 1% Kalliroscope fluid by volume. The viscosity was measured for a range of temperatures by using a Cannon-Fenske viscometer. The viscosity was kept at 10.27 centistokes by maintaining the temperature of the bath at 25.00 ^{0}C. The parameters varied in this investigation were the inner and outer cylinder Reynolds numbers. The experimental parameters for the Gorman system are listed in Appendix A.

The first objective in studying a boundary was to precisely determine its location. Since there were two parameters being varied (inner and outer cylinder Reynolds numbers), there were several choices in how to go about the search. This was important since the Taylor-Couette system may have multiple stable states for a given set of parameters and the transitions may exhibit hysteresis. Thus, the states obtained can depend on how a boundary was approached. In the beginning of this investigation the parameter space was searched by increasing the outer cylinder Reynolds number until the desired value was reached, keeping the inner cylinder Reynolds number such that the system was always in Couette flow. Then the inner cylinder Reynolds number was increased. Initially, the system was stepped through the region of interest fairly rapidly, say at 1 Reynolds number per minute. When a transition was made the appropriate value of the Reynolds numbers were recorded and the inner cylinder Reynolds number was lowered well below the parameters at which Couette flow was once again obtained. The reason for lowering the Reynolds number well below that required to obtain Couette flow was to damp transients remaining of the previous flow. Now the inner cylinder Reynolds number was increased again but at a much slower rate, especially in the region of the transition. In particular, the slowest rate used was a change of 0.03 Reynolds number/minute. After the boundary was located to within the precision of the experimental system (about .3 Reynolds number), the boundary was traversed in the reverse direction in a search for hysteresis. This process was continued for increasingly higher outer cylinder Reynolds numbers.

At the point where the state to which the Couette flow bifurcated changed, several other parameters were recorded. In particular, on each side of this point the axial wavelength of the particular stable state was recorded, the azimuthal wavenumber was determined, a picture of the flow was taken and a frequency spectrum was obtained.

After determining the location of the primary bifurcation and some of the parameters for the secondary flows, the secondary bifurcations became an object of investigation. As mentioned above, several characteristics of the flow states on opposite sides of the secondary bifurcation boundaries were measured. In addition, the boundaries were crossed by keeping the inner cylinder Reynolds number fixed and changing the outer cylinder Reynolds number as well as the procedure mentioned above. This allowed a more complete determination of the regions of stability of the various states and allowed a search for hysteresis. If the boundaries between states traversed in opposite directions is Reynolds number space did not coincide, then the experiment was repeated at a slower speed. The slower speed was necessary because the relaxation time in this Couette system could have been as long as half an hour and the lack of agreement could therefore have resulted from crossing the boundary too quickly. If the boundaries did not move upon going to slower speeds then hysteresis was probable in the transition.

3.3 The aspect ratio dependence studies

The aspect ratio experiments were performed in an apparatus designed by myself. A photograph appears in figure 3.2. The inner and outer cylinders could be rotated independently. The superstructure allowed the aspect ratio of the system to be changed while the cylinders were rotating. The stepper motor which changed the aspect ratio was supplied power by a six brush commutator located at the top of the superstructure. The entire Couette apparatus could be moved along linear bearings perpendicular to the optical axis of the LDV optics. This enabled adjustment of the radial location of the probe volume.

Similar to the Gorman system, the Couette cylinders were located in a thermal bath which also provided a means of index matching. The temperature was controlled to ± 0.01^0 C by a NESLAB RTE-9 circulator. The index matching fluid for the LDV experiments was Cargille Laboratories Code 0195 which is described in Appendix A. The viscosity of the index matching fluid was determined as a function of temperature over a range from 24^0C to 26^0C. A curve was fit to the viscosity data and was used in the computer routine "Hirst" to adjust the speed for temperature drift. This kept the Reynolds number constant during a run. The seed particles were titanium dioxide microspheres (TSI 10082) 0.22 microns in diameter. A seeding density of approximately 100 particles per scattering volume was mixed, though, due to settling, the density was probably below that value.

3.3.1 Velocity measurements-The LDV System

The method used to measure the velocity at a particular location in the fluid was Laser Doppler Velocimetry (LDV). The basic idea is that light scattered off a moving particle is Doppler shifted by an amount (Drain, 1980):

Figure 3.2 Hirst Taylor-Couette System. This is the Taylor-Couette system used in the aspect ratio dependence study. The flow apparatus itself appears in the upper, center part of the photograph. The round structure at the top supported the apparatus used in varying the aspect ratio. The rectangular structure beneath it is the bath housing and the support structure for the bearings in which the cylinders rotated. The inner and outer cylinders which contained the flow are visible in the upper, center of the photograph behind the windows in the bath housing. The large frame in the enter of the photograph supported the LDV optics. These optics are visible in the center of the photograph. Behind the bath and off to the left are the collection optics: a black cylinder with a "wire" coming out of the top. The "wire" is the fiber optics cable which carried the light signal from the collection optics to the photomultiplier tube. In front of the bath housing is another object with wires coming out of it. The little black boxes out of which the wires emerge are the Bragg shifters. The cylindrical part on the end of this object and nearest to the bath is the focusing lens. The cylinder on the other end of the object is the beam splitter. On the left of the photograph is the Helium-Neon laser used as the light source for the LDV technique.

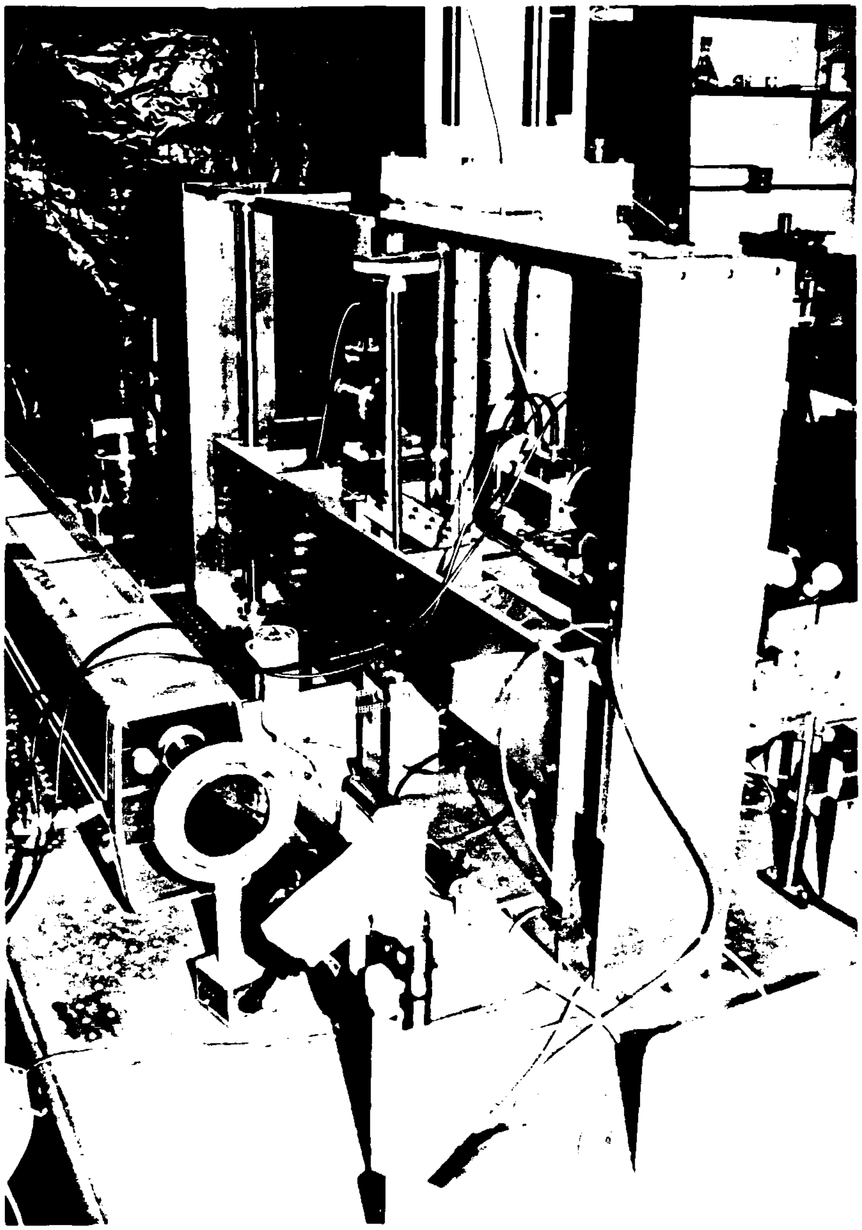

Figure 3.2 Hirst Taylor-Couette System

$$\nu_D = \left[\frac{2v}{\lambda}\right] \sin\left[\frac{\alpha}{2}\right] \qquad (3.1)$$

where ν_D is the Doppler shifted frequency, v is the velocity of the scattering particle, λ is the wavelength of the light and α is the angle between the direction of the laser beam and the detector (see figure 3.3). For typical applications the Doppler frequency ranges from kilohertz to megahertz.

One way to observe such a small frequency difference as the Doppler shift is by heterodyning. If the laser beam is split into 2 parts, one may be scattered off the fluid flow and the other may be used as a reference. If both beams are combined on the surface of a square law detector then the detector sees not only the primary frequencies but the sum and difference of those frequencies. Since one beam is Doppler shifted then the frequencies differ by the Doppler shift. Since all such detectors (photomultipliers, photodiodes) have a frequency response well below that of the primary and sum frequencies, the output of the detector will just be the Doppler frequency.

The technique of scattering one of the beams off of the fluid flow and using the other as a reference is known as reference beam LDV or single beam LDV. Though it was the first method used and has some applications, this technique has two primary limitations (Adrian, 1983). The first of these is alignment difficulties and the second is a small collection aperture for scattered light. These both result from coherence requirements. The light in both the scattered and reference beams must have a definite phase relationship for optical beating to occur, thus the path differences of the two beams should be as close to equal as possible (assuming single mode lasers). Secondly, equation (3.1) contains α, the angle between the scattered and incident light. Obviously a large collection aperture will average over this angle and light collected at different angles will have different frequencies at the same velocity. This spread in frequency will result in a loss of coherence and thus no heterodyning if the collection angle is too large. Usually the aperture is limited to a diameter equal to several diameters of the initial laser beam.

Figure 3.3 Laser Doppler Velocimetry Geometry. As the two laser beams cross, they form an ellipsoidal volume defined by the e^{-2} intensity points. The fringes are perpendicular to the plane of intersection of the beams, i.e., perpendicular to the paper in figure (a). The actual geometry is defined in (b) where δ is the angle between the two laser beams.

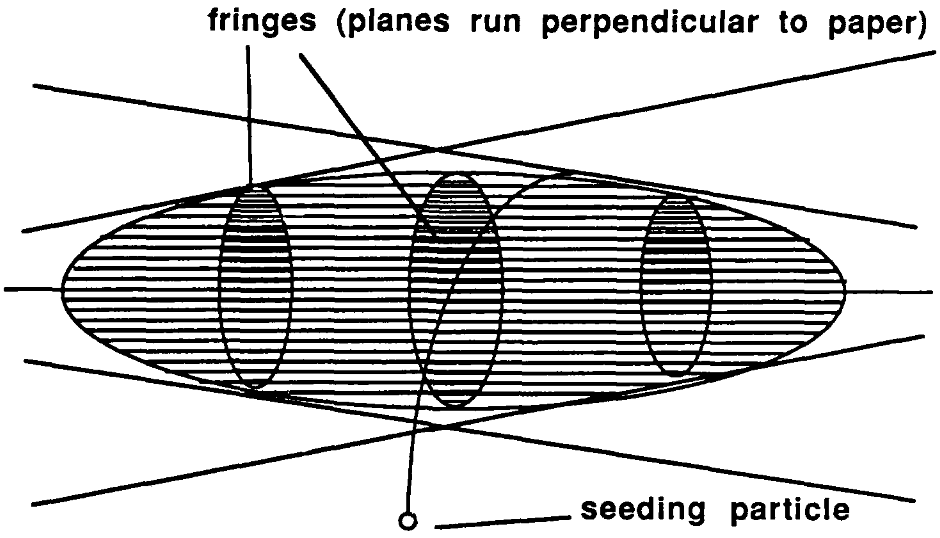

(a) Ellipsoidal scattering volume

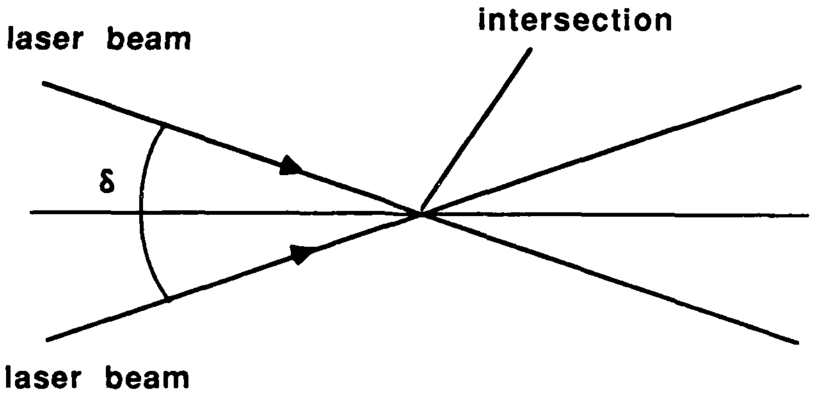

(b) scattering geometry

Figure 3.3 Laser Doppler Velocimetry Geometry

At present, the most popular LDV technique used is dual beam or differential LDV and was the technique used in the research for this dissertation. In this form of LDV both beams cross at the measuring volume. Since the beams enter the measuring volume at different angles, the angle between the incident and detected light will be different for each beam. If the angle from the first beam to the detector is α and the angle to the second beam is $\alpha' = \alpha + \delta$ then the scattered light frequency is proportional to $\sin(\alpha/2)\ \sin((\alpha + \delta)/2)$ and the heterodyne difference frequency will be proportional to $\sin((\alpha + \delta - \alpha)/2) = \sin(\delta/2)$. More exactly:

$$\nu_D = \left[\frac{2v}{\lambda}\right] \sin\left[\frac{\delta}{2}\right] \tag{3.2}$$

which is almost the same as equation 3.1 except the scattering angle is replaced by the angle between the beams. This results in one of the great advantages of dual beam LDV over reference beam LDV: the collection angle is not limited by a coherence condition. Thus the collection optics can have an aperture limited only by practicality. Also note that the Doppler frequency is fixed by the focal length of the focusing lens and the separation of the beams before focusing since the frequency is proportional to the crossing angle. So once an differential LDV system is designed and built, the system does not need calibration; the conversion from Doppler frequency to velocity is fixed by δ.

One model of the laser Doppler process which is useful in certain situations is the fringe model. The fringe model starts with the observation that in the ellipsoidal volume where the two laser beams cross, there is interference. This occurs due to the small spectral width and high coherence of the original laser source. This interference produces fringes which appear transversely to the beams such that the intensity variations are coplanar with the incident laser beams (see figure 3.3). The Doppler signal results from the scattering particles modifying the intensity of the transmitted light as they cross the fringes. This model is obviously wrong if the particle diameter is about the same size as the wavelength of light as it makes no allowance for interference and diffraction effects. It has the advantages over the more correct theoretical treatment in that it is a very simple model, is easily visualized, and gives the correct behavior if the particles are smaller than the wavelength of the laser light (diameter of the scatterer is smaller than the wavelength of the light divided by π (Born and Wolf, 1975, p. 654)).

An LDV system is more complex than the above description implies. In order to understand the behavior of an LDV system, one should understand the properties of the reflected light and the sources of noise. This should include properties of the scattering particles, optics, detector and any sources of unwanted scattering. Basically, the properties of the unwanted scattering and any rf interference picked up by the detector depend very much on the physical setup and are not included in a theoretical analysis of an LDV system. Eliminating these depends on the expertise of the experimenter.

Some of the noise sources are inherent in the LDV process or in the method of determining the Doppler signal from the total signal. These include the non-Doppler shifted light scattered by the particles and noise due to the various random processes involved. The non-Doppler shifted light is the reflected light from one beam which has not been modified by interference with light from the other beam. One could think of the non-Doppler shifted scattered light as the intensity with the cross-term set to zero. This intensity is known as the pedestal. The pedestal itself can easily be eliminated from the detected signal by a method to be discussed later (Bragg Shifting) but can still contribute noise in the detector. This may be seen by considering the fringe model.

Since the detector is a square law detector the signal is positive definite. As a particle crosses the scattering volume the signal oscillates as it crosses the fringes while the envelope of the signal slowly rises and falls due to the Gaussian cross-section of the laser beam.. The moving average over one Doppler period is the pedestal. Ideally, the optical quality is such that the pedestal is fully modulated. The low frequency component does not contribute to the Doppler signal but will generate noise due to emission of photoelectrons in the photomultiplier. This noise is white and is known as shot noise. If the pedestal is not fully modulated then the Doppler signal is smaller but the pedestal remains the same. Thus the signal gets smaller but the noise remains the same. No LDV system will have a fully modulated pedestal because the two incident beams will be of different intensity, will not be focused in the same position along the optical axis or will not overlap. Reducing any of these deficiencies will improve the signal to noise ratio of the signal. One of the measures of the optical quality of an LDV system is the ratio of LDV signal intensity to the pedestal. This is known as the visibility and is given by (Adrian, 1983):

$$V = D/(P_1 + P_2) \tag{3.3}$$

where D is the intensity of the LDV signal, and P_1 and P_2 are the scattered light from the two crossing beams. The visibility can range from 1 to 0; 1 corresponding to full modulation and 0 to no LDV signal.

There are several sources of electronic noise inherent in the detection process. These include shot noise, thermal emission (dark current), secondary emission noise and so forth. A good review is given in Appendix A of the RCA Photomultiplier Handbook (Engstrom, 1980). In a good photomultiplier tube in a typical LDV setup the only noise mechanism that is important is the shot noise. Shot noise arises because the photoelectric effect at the photocathode and the electron impact emission at the dynodes are random (Poisson) processes. The probability that n photons will strike the cathode of the photomultiplier in a time interval τ is simply (Engstrom, 1980):

$$P(n,\tau) = \frac{(I_p \tau)^n}{n!} \exp(-I_p \tau) \tag{3.4}$$

where I_p is the average photon arrival rate. The mean of this Poisson distribution is just $I_p\tau$ which is also the variance (Papoulis, 1984). The signal is the mean value and the noise is the variation (square root of the variance) and so the signal to noise is:

$$SNR_I = \frac{(I_p\tau)}{(I_p\tau)^{1/2}} = (I_p\tau)^{1/2} \qquad (3.5)$$

This is a little simplified since it does not deal with a time dependent mean. The interested reader will find a complete discussion of Poisson processes with a time dependent mean in the discussion of shot noise in Chapter 12 of Papoulis' book. This model will be sufficient for this discussion.

The shot noise is white; that is, the spectral intensity is constant with frequency. Since there is only finite energy for the noise spectrum this is an approximation. Realistically, there is a bandwidth, B. This bandwidth is related to τ by (Engstrom, 1980):

$$B \doteq 1/2\tau \qquad (3.6)$$

The coefficient of τ will change depending on the exact filter used but this is sufficient for the purpose at hand. The signal to noise will also depend on the visibility, V, as discussed above. Incorporating these modifications the signal to noise ratio becomes:

$$SNR_I = (I_p\tau)^{1/2}\, V = (I_p/2B)^{1/2}\, V \qquad (3.7)$$

The signal to noise ratio is usually given in terms of power, not intensity. The signal to noise ratio of the power which is just the square of equation 3.7 averaged over one Doppler cycle. The signal which is actually measured will depend the number of electrons emitted by the photocathode. The number of electrons will be less than the number of photons by a factor, η, which is the quantum efficiency of the cathode. Taking into account the quantum efficiency of the photocathode, the power signal to noise for the electrons emitted by the photocathode is:

$$SNR_p = 0.5\,(\eta I_p/2B)V^2 = \frac{\eta}{4h\nu\,B}\,w\,V^2 \qquad (3.8)$$

where h is Planck's constant, ν is the frequency of the laser light and w is the power of the laser beam at the measurement volume. B is usually determined by a band pass filter after the preamplifier connected to the output of the PMT.

Some further modifications of equation 3.8 are desirable. First, w is hard to measure so it would be more convenient to relate it to the output power of the laser. If attenuation by scattering off imperfections in the optics and in the fluid are ignored, then the power of the output of the laser is related to the power at the scattering volume by the ratios of the cross-sections of the beams. Laser beams have a Gaussian profile and so the relative diameters of the beams cannot be determined from simple ray optics. It can be shown that, for Gaussian beams, the ratios of the beam waists on opposite sides of an optical system is (Adrain, 1983, p. 168):

$$\frac{D_2}{d_2} = \frac{\pi D_2^{\,2}}{4f\lambda} \qquad (3.9)$$

where d_2 is the $1/e^2$ diameter of the beam at the scattering volume, f is the focal length of the optical system, and D_2 is the $1/e^2$ diameter of the laser beam waist at the laser (exactly where this waist is depends on the design of the laser). The power signal to noise now becomes:

$$SNR_p = \frac{\eta}{4h\nu\,B}\left(\frac{\pi D_2^{\,2}}{4f\lambda}\right)^2 W\,V^2 \qquad (3.10)$$

This number is rather large. If I substitute into the variables using the appropriate values for my laser Doppler system (see Appendix A), the SNR may be seen to be on the order of 10^{14}! Actually, such a large number should be expected from the formula since it is essentially the number of electrons generated if all the photons passing through the measurement volume per second hit the photocathode. In order to obtain a more realistic number and to obtain a qualitative understanding of the behavior of the signal to noise on the number of scattering particles in the measurement volume, consideration needs to be given to the experimental set-up.

The final modification of the power signal to noise ratio is the inclusion of terms which take into account the scattering cross-section of the seeding particles, the collection aperture of the optics and the attenuation due to the scattering particles that are not in the measurement volume. In a Taylor-Couette apparatus, the measurement volume is a very small ellipsoid of fluid located in a tubular column of fluid. Scattering takes place not only from the ellipsoid but light is scattered out of the beams as they pass through the fluid before and after they cross at the ellipsoid. The scattering process can be represented by three terms or transfer functions:

$$I = ABC\ I_o \tag{3.11}$$

where A, B and C represent the transfer functions of the various regimes. The first regime is the where the laser beams have been focused and are converging toward the measurement volume. The cross-section of the beams is slowly becoming smaller but it will be assumed that it is constant here. The incident intensity will be reduced by scattering out of the beam. The differential change in the intensity is given by Beer's law:

$$dI = -(I_o/A_1)\sigma N_e A_2 dx \tag{3.12}$$

where I_o is the initial intensity, A_1 is the area of the beam when the intensity is I_o, σ is the scattering cross-section of the particles, N_e is the scattering particle density, A_2 is also the area of the beam but contains the functional dependency on x and dx is the incremental distance along the optical path. The term in the right hand side in the parenthesis is the incident density of the laser. In this first regime it is assumed that the beam is not spreading and so the A_1 and A_2 simply cancel. Integrating this equation with respect to x:

$$I = I_o A = I_o \exp-(\sigma N_e X_A) \tag{3.13}$$

where X_A is the path length through the fluid in regime A.

The regime for process B is the scattering of the incident light by the scattering particles. This is the opposite of the process for regime A in that the signal is the light scattered by the particles instead of the signal being reduced by the scattering. It follows that the scattered light is the difference between the intensity when the beams enter the regime and the intensity when they leave the regime. Thus, the transfer function is:

$$I = I_o B = I_o(1 - \exp -(\sigma' N_e X_B)) \tag{3.14}$$

where σ' is the scattering cross-section for the scattering particles in the scattering volume and is different that the scattering cross-section is equation 3.13. The variable X_B is the length of the optical path in regime B, in this case, the length of the scattering volume.

The final regime is the regime for process C. In this regime the light is scattered into the collection optics and so the beam is spreading. The light which is collected is that which was scattered into a cone with its base at the collection lens and its vertex at the scattering volume. The reduction of the signal intensity is due to the number of scatterers in the path growing as x^2, i.e., as the cross-section of the cone. So the differential change in intensity is:

$$dI = I \frac{N_e}{A_1} \sigma (\pi x^2 \tan^2 \alpha)\, dx \tag{3.15}$$

where the term in parenthesis is the cross-section at x (along the optical axis) of the cone. Integrating:

$$I = I_o C = I_o \exp -(N_e \sigma X_c^3 \tan^2 \alpha / 3a^2) \tag{3.16}$$

where X_c is the length of regime C along the optical axis and a is the radius of the scattering volume.

The only term which has not been calculated in the above derivations is the scattering cross-section. If the scattering particle diameter is at the upper limit at which the diffraction effects may be ignored in the scattering (see Appendix A), the lowest order results of a multipole expansion of the electric field of light scattered from a dielectric particle can be used. The lowest order electric multipole moment in the differential cross-section is (Jackson, 1975, p. 413):

$$\frac{d\sigma}{d\Omega} = \frac{r^6}{\lambda^4}\left|\frac{\varepsilon-1}{\varepsilon+2}\right|^2 \left|e^{*}\cdot e_o\right|^2 = \frac{\tilde{\sigma}}{\pi^2}\left|e^{*}\cdot e_o\right|^2 \qquad (3.17)$$

where r is the radius of the scattering particle, ε is the ratio of the dielectric constants of the scattering particle and the fluid (respectively), **e** is the direction of the induced dipole moment and $\mathbf{e}_0$ is the direction of the wavevector of the scattered light. The quantity $\tilde{\sigma}$ is defined by the above equation and is simply the cross-section for scattering into 4π steradians. For regimes A and C, $\sigma = \tilde{\sigma}$. For regime B, the differential cross-section is integrated over the solid angle subtended by the collection optics. If the volume subtended is a cone with a vertex of 2α then:

$$\sigma' = \frac{\tilde{\sigma}}{\pi}\left(\frac{\alpha}{2} - \frac{\sin 2\alpha}{4}\right) \qquad (3.18)$$

Using equations 3.10, 3.11 3.13, 3.14, 3.16 and 3.18, the signal to noise, including the effects of the scattering particles in the apparatus, is given by:

$$\mathrm{SNR} = \mathrm{SNR}_p\{\exp-(2N_e\tilde{\sigma}X_A)[\,1 - \exp-\{N_e\frac{\tilde{\sigma}}{\pi}X_B(\frac{\alpha}{2}-\frac{\sin 2\alpha}{4})\}]$$

$$\exp-(\frac{X_c^3\tan^2\alpha}{3a^2}N_e\tilde{\sigma})\,\} \qquad (3.19)$$

The signal to noise is plotted as a function of the average number of particles in the measurement volume in figure 3.4 using this equation and values typical of my Taylor-Couette apparatus (see Appendix A). It is seen that there is an ideal concentration thought the maximum is rather broad. With too few particles, insufficient light is scattered from the measurement volume for a reliable signal measurement. With too many particles, too much intensity is lost by light scattering

Figure 3.4 Signal to noise vs. the average number of particles in the measurement volume. This plot is the result of a theoretical calculation using equation 3.19 and the parameters found in Appendix A. The curve is rather flat at the peak and so the signal quality should not vary much over a range of particle densities. The output power of the laser at the time the experiments were run was down to 25 milliwatts. The visibility was assumed to be 0.9.

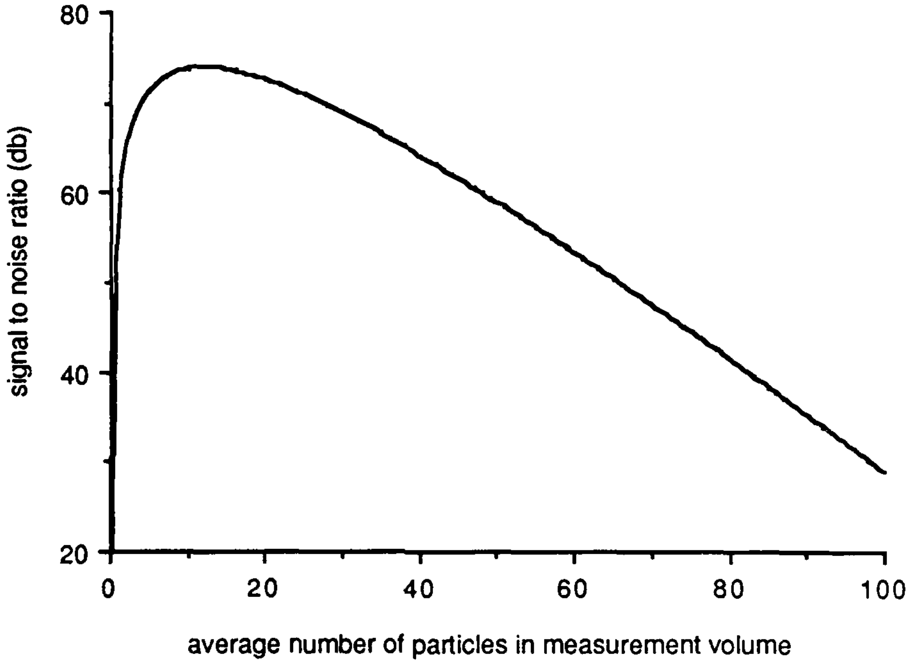

Figure 3.4 Signal to noise ratio vs. number of scattering particles

out of the collection volume. The location of the peak is rather sensitive to the arguments of the exponentials and so figure 3.4 should be understood qualitatively. Also, electromagnetic interference, light loss at the various optical interfaces and other factors will further reduce the signal to noise thought the qualitative behavior should not change.

There are other sources of error in LDV measurements. The experimental system used for this dissertation contained a tracker which followed the Doppler frequency. A tracker basically is an oscillator the frequency of which is locked to the frequency of the incoming signal and the output of which is a voltage proportional to the oscillator frequency. The tracker oscillator is locked in phase with the incoming signal. The incoming signal is due to light reflected off the scattering particles in the fluid. The occurrence of particles in the measurement volume is a Poisson process (Adrian, 1983). The statistics of the scattering particles in the measurement volume can be treated as shot noise, similarly to the emission of electrons from the photocathode. The question is how does the shot noise statistics of the scattering particles affect the detected Doppler frequency.

First, consider a single particle. As mentioned above, the signal will be a Gaussian envelope modulated by the Doppler frequency. The duration of the envelope as given by the $1/e^2$ width of the measurement volume cross-section will be 2a/v where a is the radius of the scattering volume perpendicular to the optical axis and v is the particle velocity. The power spectrum of this signal will also be Gaussian and centered at the Doppler frequency. A more rigorous treatment for an arbitrary particle density and the shot noise statistics of the scattering particles gives the bandwidth of the Doppler signal as (Adrain, 1983, p. 200):

$$\Delta\omega_A = 2\sqrt{2}\frac{v}{2a} \qquad (3.20)$$

where $\Delta\omega_A$ is known as the ambiguity bandwidth. It should be noticed that the ambiguity bandwidth scales as the velocity and is independent of the number of particles. In terms of the ratio of the width of the peak to the Doppler frequency (Adrian, 1983, p. 201):

$$\frac{\Delta\omega_A}{\omega_D} = \frac{\sqrt{2}}{\pi N_{FR}} \tag{3.21}$$

where N_{FR} is the number of fringes in the measurement volume and ω_D is the Doppler frequency. The ambiguity bandwidth represents the uncertainly in the measured Doppler frequency. Since the Doppler frequency is proportional to the velocity, this ratio is constant, defined by the LDV geometry. Once the accuracy of an instantaneous measurement is determined, it is valid for any flows measured by the apparatus if the ambiguity broadening is the dominant source of uncertainty. For the LDV system used in the dimension measurements the theoretical ambiguity bandwidth/Doppler frequency ratio was 1.4%. The measured value of the fluctuations of the LDV signal for Taylor flow at $R/R_c = 1.33$ was 3%.

A block diagram of the LDV optics is shown in figure 3.5. The laser used was a Spectra Physics Model 125 Helium-Neon laser operating at 6328 Angstrom and capable of 50 milliwatts output. The output was guided around the isolation table mounting platform by several mirrors until it was reflected down the LDV system optical axis by the final bending mirror. The beam was then passed through a spatial filter. This was necessary to remove laser light scattered by imperfections in the guiding optics. Also the second lens element of the spatial filter enabled the focusing of the waist of the laser beam at the crossover point in the measuring volume. The laser beam was then split into equal intensity components by a beam splitter. Each beam passed through a Bragg shifter. The Bragg shifter is an acousto-optical device which shifts the laser frequency by an amount equal to the frequency of the RF input to the Bragg Shifter. These shifters enabled the determination of the sign of the fluid velocity (positive and negative velocities provide the same Doppler shift otherwise) and also eliminated any low frequency noise components from the Doppler signal (pedestal removal).

The beams emerging from the Bragg cells were focused by the focusing lens. The actual cross over volume was an ellipsoid with the major axis along the optical axis of the LDV system. The interference fringes produced were perpendicular to the plane of the beams and the LDV optical axis. The number of fringes produced

Figure 3.5 Laser Doppler optics block diagram. This is a schematic of the arrangement of the optics for the laser Doppler velocimetry (LDV) system.

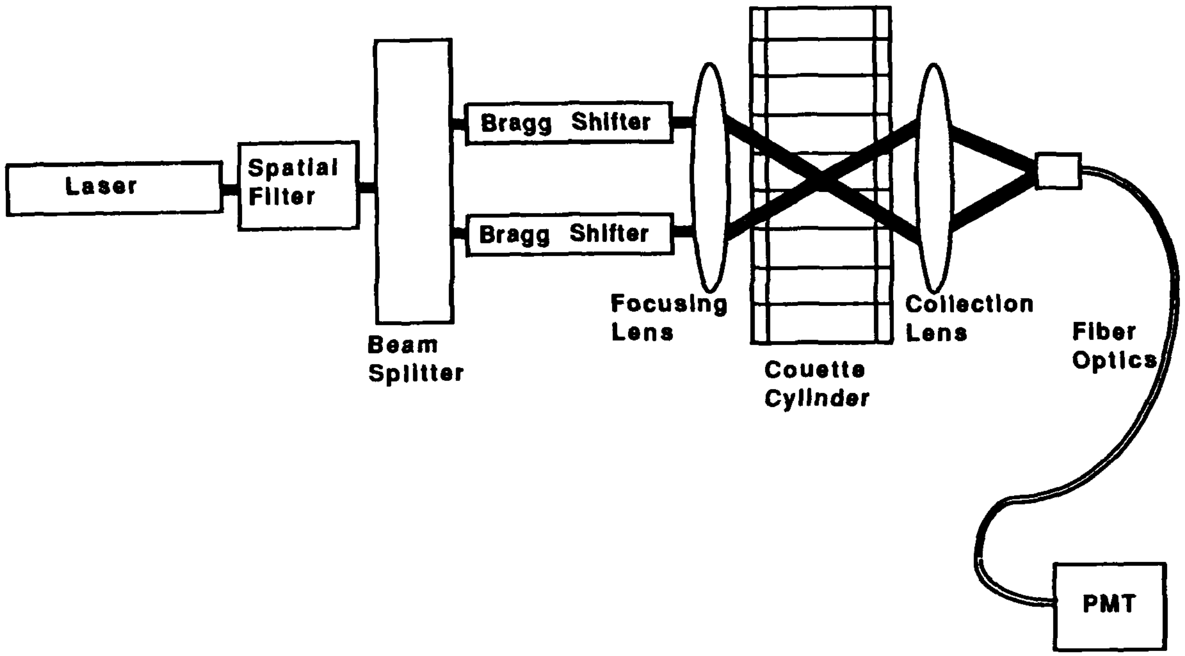

Fig. 3.5 Laser Doppler Optics Block Diagram

depend on the diameter of the laser beam before focusing and the beam separation (roughly) and is given by:

$$N_{NF} = 1.27 \frac{d}{D} \qquad (3.22)$$

where N_{NF} is the number of fringes, d is the separation of the laser beams and D is the e^{-2} diameter of the laser beams.

The scattered light was collected by the collection lens. The unscattered beams themselves were masked off to reduced a large random noise contribution to the signal. The collection lens focused the light onto a 100 micron pinhole mounted in an aluminum adapter for the fiber optics transmission cable. This pinhole acted as a spatial filter to further reduce the background contribution to the signal. The fiber optics cable guided the collected light to the photomultiplier tube. The fiber optics was used to avoid mounting the bulky photomultiplier tube housing on the optics track. Inside the photomultiplier tube housing were an interference filter with a maximum transmission of 60% at 6328 Angstroms and a 1/e bandwidth of 20 Angstroms. An iris and shutter mechanism were also mounted in the photomultiplier tube housing to enable varying the intensity of the detected scattered light independent of the laser output. A transmission lens system was installed in the photomultiplier tube housing to image the end of the fiber optics cable on to the photocathode of the PMT. Additionally it provided a x0.5 demagnification of the image since the end of the fiber optics had a 3.2mm diameter and the photocathode was 2 .5 mm in diameter. Finally an EMI 9863B/100 photomultiplier tube with an S-20 response was used to detect the signal.

The entire optics train from the final bending mirror to the collection optics was mounted on an optics bench. The track itself was split into two parts to allow the Couette system to be slid into place between the transmission and collection optics. The spatial filter, beam splitter, Bragg cells, and focusing lens comprised the transmission optics and were all mounted on a translation stage to permit the location of the sample volume to be changed azimuthally without having to realign the optics.

The collection optics were likewise located on an x-y translation stage to permit locating the sample volume. Both the transmission and collection optics stages were mounted on separate platforms which were in turn attached to a single vertical translation mechanism. This mechanism adjusted the vertical sampling location of the flow via a computer controlled stepper motor allowing very accurate (within .001") location of the sample volume along the cylinder axis.

As mentioned above the spatial filter provided the capability of insuring that the laser beam waist was at the intersection of the beams. The focusing was performed by imaging the beam intersection on the wall of the lab with a x10 microscope objective and with the detector removed from the optical path. If properly done, the fringes were visible (with the Bragg shifters off). The second lens element was then adjusted along the optical axis until the diameter of the spot on the wall was minimized. The fringes were also examined for uniformity and for how well the two beams actually overlapped at the measuring volume.

3.3.2 Analog electronics

The analog electronics was composed of several amplification and signal processing elements. A block diagram is shown in figure 3.6. The output of the photomultiplier was fed into a H-P Model 466A AC amplifier. Since the photomultiplier is basically a current source, a 1k ohm resistor was placed across the input to the amplifier. The voltmeter, having a high impedance input then essentially measured the voltage across the 1k ohm resistor (as opposed to 50 ohms if the cable had been directly connected to the amplifier). This insured an adequate signal to be fed to the next stage, a Krohn-Hite Model 3202 filter.

This filter could be configured in a variety of ways. It was essentially two 24 db./octave active filters in one unit. Used as a high or low pass filter, the response was flat with unity gain in the pass region and the selected frequency represented the 3 db. down point. Since the difference in Bragg shifters was 50 kilohertz then this was obviously the center of the band. A consideration of the probable velocities involved led to the conclusion that the Doppler shift would never exceed 10 kilohertz. Thus one section was configured as a low pass filter with a 60 kilohertz

Figure 3.6 Analog electronics block diagram. This is a block diagram of the analog electronics used to process the LDV signal between the PMT and the analog to digital converter in the IBM microcomputer.

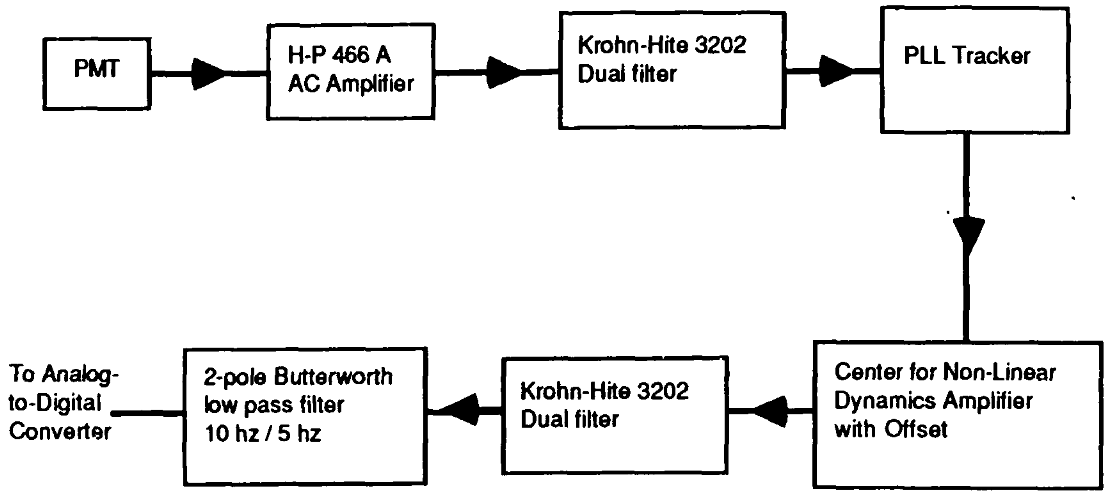

Fig. 3.6 Analog Electronics Block Diagram

cutoff and the other section was configured as a high pass filter with a 40 kilohertz cutoff. This gave a 6 db insertion loss but at this point in the circuit the frequency, not the intensity, contained the important information.

The output of the first Krohn-Hite filter was fed into a Phase Locked Loop (PLL) tracker (Institute of Applied Physics, D-2300 Kiel, West Germany). The output of the tracker was a voltage proportional to input frequency and therefore the velocity. The tracker was composed of several elements (figure 3.7). First was a preamplifier and amplifier, of which the preamplifier was not used. The amplifier had an adjustable gain. Following that the signal was clipped to 1 Volt by a voltage limiter which kept the signal within the linear range of the electronics. The output of the voltage limiter was split and fed into two mixers which mixed the input signal with a signal from a voltage controlled oscillator (VCO). The result of one signal (the difference between the input frequency and the VCO frequency) was fed into a loop filter. The output of the loop filter was a voltage proportional to the input frequency difference. This voltage was then fed to the VCO which adjusted its output to match the input frequency. Obviously the voltage to the VCO was proportional to the Doppler frequency. Both this voltage and the frequency output of the VCO were available for sampling. The output of the other mixer was fed into a data valid processor. The processor checked the size of the difference signal and if it was too small for the tracker loop to lock onto the input, the data valid light was extinguished. A signal was also output in this case. This could have been used to freeze the local oscillator voltage if the signal were to drop below a useful level. Unfortunately this was never implemented in the tracker itself but with careful adjustment of the gain and care in seeding most of the drop outs were be avoided. (Drop-outs are periods of time when the intensity drops below threshold or changes rapidly due to the random nature of the signal (Drain, 1983))(PLL Tracker Manual).

Needless to say use of the tracker assumed that there was an almost continuous signal otherwise the tracker would not be able to lock onto the input frequency. For a heavily seeded fluid flow this is usually a valid assumption. Care was required in adjusting the gain of the tracker amplifier. The tracker could lock onto higher harmonics in the signal and the very non-linear voltage clipper in the

Figure 3.7 Block diagram of phase locked loop (PLL) tracker. This diagram shows the basic elements of the tracker used in the laser Doppler velocimetry in this experiment.

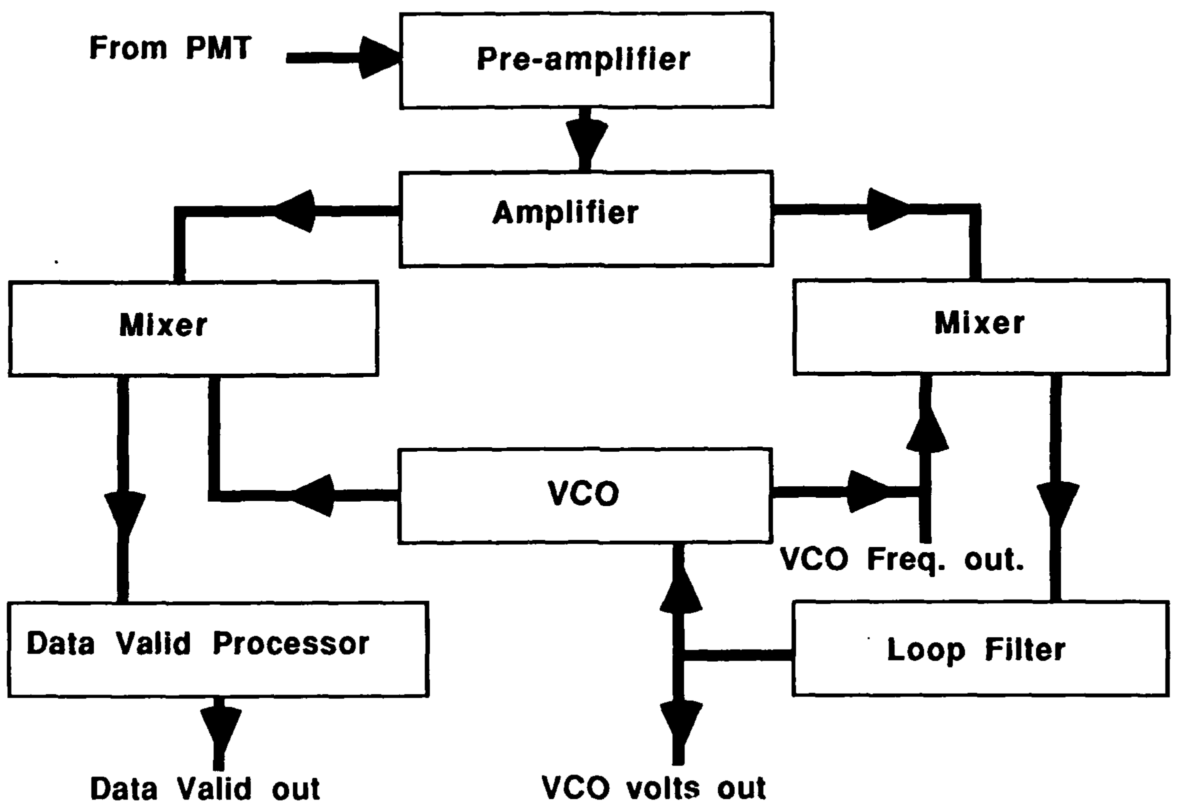

Fig 3.7 Block Diagram of PLL Tracker

tracker was very good at producing them (essentially square waves). The trick was to adjust the gain so that the data valid light was on most of the time but to watch the output of the amplifier on the scope and keep the peak voltage below 1 volt. The only times this method failed was when the seeding density was too small to keep at least one particle in the scattering volume on the average. When this would occur the tracker would drift and eventually lock on to some spurious noise. This process showed up as spikes in the velocity signal. The cure for this would be to freeze the oscillator frequency when the signal became too small, as mentioned in the last paragraph.

As mentioned above the output of the tracker was a voltage proportional to the velocity through the Doppler frequency. Thus the tracker needed to be calibrated. This was done by feeding a sine wave into the tracker at a known frequency and measuring the voltage output. The calibration was performed at several frequencies and the results plotted (see figure 3.8). From the output of the tracker careful record of the voltage amplifications and offsets were kept so that the actual fluid velocity could be reconstructed if desired.

Following the tracker was yet another amplifier. The purpose of this amplifier was to maximize the signal spread across the range of the Analog-to-Digital Converter (ADC) in the computer. This amplifier was built in the Center for Nonlinear Dynamics. It had switchable gain in steps of 0.5, 1.0, 2.0, 5.0 and 10.0. It also had a capability of offsetting the input signal in both positive and negative senses. This last capability was particularly valuable because the actual velocity signal was offset quite a bit by the Bragg shifted contribution. The offset was usually run about -1.2 ± .2 volts as could easily be guessed by looking at the tracke calibration curve. Care was required in setting the output gain so that the range of both the next filter and of the ADC in the computer were not exceeded.

In order to reduce noise, a filter followed the amplifier. This was another Krohn-Hite Model 3202. From previous studies it seem that all frequencies of interest would lie below 20 hertz. This being the lowest setting on the filters, both sides were set as 20 hertz lowpass filters. The maximum DC plus AC range of this filter was 0 to 4.2 volts which was a restriction in setting the gain and offset of the

Figure 3.8 Tracker calibration. This is the plot of the data collected during the tracker calibration. A stable sinewave generator was used as the source of the tracker input. The output of the tracker was read with a digital voltmeter. The tracker calibration consisted simply of recording the voltage output for each frequency of input and then fitting a line to the resulting data. The equation fit to the line appears in the lower part of the graph.

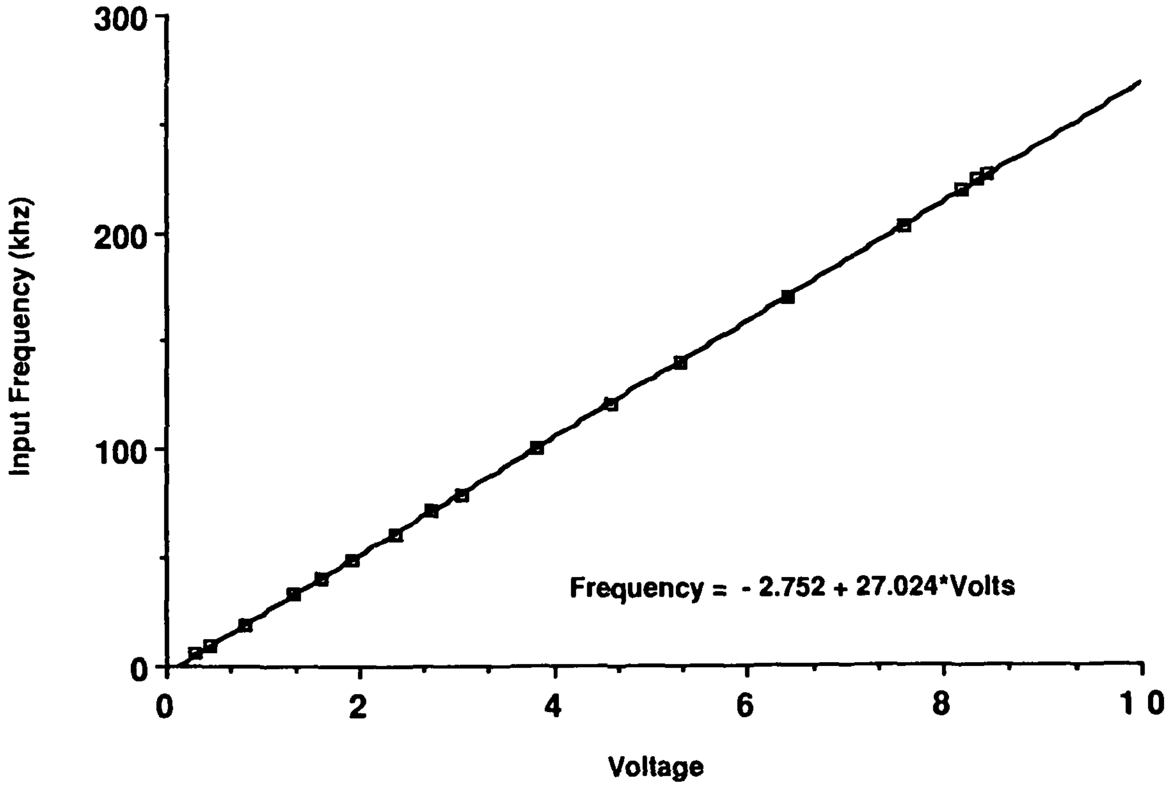

Fiqure 3.8 Tracker Calibration

previous amplifier. From this filter the signal was fed into a lowpass 2-pole filter with selectable 3 dB downpoints of 5 or 10 hertz. This filter could optionally be switched out. The output of this filter went to the ADC in the IBM PC-AT.

The response of the electronics was checked by simulating the tracker input from the photomultiplier. This was done by using a frequency synthesizer which had an output that could be frequency modulated. The synthesizer output was set to produce a peak-to-peak sine wave at 50 khz with no modulation. The output of a Heathkit signal generator with an output of 1 volt peak-to-peak and a frequency of about 0.5 hertz was fed into the FM input of the synthesizer. This input caused the output of the synthesizer to vary between 49 and 51 khz at a frequency of 0.5, about the values appropriate for a signal from wavy vortex flow at $R/R_C = 10$. This signal was then fed into the tracker. The electronics showed only the 0.5 hertz signal on the computer and showed no DC drift.

3.3.3 IBM PC-AT system computer control and data acquisition system

The experiments involving the LDV measurements were controlled by an IBM PC-AT with Burr-Brown PCI 20000 system boards installed for control and data acquisition. The IBM PC-AT is a 16 bit mini-computer with an 80286 processor running at an 8 Mhz clock rate. It is well described elsewhere (IBM PC-DOS 3.10 Manual, IBM PC-AT Technical Reference Manual) so will not be described in detail here. The particular configuration of options used in this experiment appear in the appendix.

The actual interface with the experiment was provided by a Burr-Brown PCI 20000 Instrumentation system. The Burr-Brown PCI 20000 system is a series of carrier cards, module cards, software and accessories which enable the IBM PC and compatibles to perform equipment control and data acquisition. The carrier cards plug into the internal slots in the computer. The carriers interface the module cards to the computer bus and, in addition to supporting the modules, may have 32 bits of digital I/O. The module cards essentially handle the incoming data from the appropriate transducers or send the appropriate signals out to equipment. These modules plug into the carrier card with a maximum of 3 modules per card.

Additional accessories provided for opto-isolators, signal conditioners, etc. but were not used in this experiment. The software consists of drivers for the various functions on the modules. In the particular version used in this experiment, the routines were callable as Microsoft "c" subroutines.

The particular configuration of the PCI 20000 system installed in the IBM PC-AT used in this experiment is shown in figure 3.9. It consisted of a PCI 20001C-2 carrier card with 32 bits of digital I/O, a PCI 20007M-1 Timer-Counter module, and a PCI 20002M-1 Data Acquisition module. The digital I/O on the carrier card was used to interface the computer to the Compumotor Bus described in the section on the DEC 11/23. The Timer-Counter module consists of a programmable 32 bit rate generator and 4 programmable 16 bit counters. This module provided the ability to output pulses to control the Slo-Syn stepper motors used in the optical table and the aspect ratio changing mechanism. Additionally, it provided a time base for the Data Acquisition module in data collection. Finally, the Data Acquisition module was used to read the voltage output from the LDV Tracker and from the thermistor which measured the temperature in the Couette bath.

Most of the software used on the IBM PC-AT was basically the same as that used on the DEC 11/23. Changes were made to adapt it to Microsoft FORTRAN for the IBM PC and new subroutines had to be written to use the software drivers for the PCI 20000 system instead of the ADAC board. Additionally, a new program in assembler was written to run the Slo-Syn stepper motors which controlled the aspect ratio and the height of the optics. Several "c" drivers and utilities were also written specifically for the PC-AT. A list of the programs and a short description of each appears in the appendix.

3.3.4 LDV experimental procedure

The LDV technique was used solely in the aspect ratio dependence experiment. For these runs the outer cylinder was held stationary; only the inner cylinder was rotated. The first procedure to be determined was the "recipe" to obtain the appropriate state. This state was a 4/4 modulated wavy vortex state with an

Figure 3.9 Digital electronics block diagram for laser Doppler velocimetry data collection. This block diagram shows the data input circuitry as the PLL tracker and the PMT, which symbolically stand for figure 3.5. The thermistor box consisted of an amplifier for the thermistor and an external power supply. These two represented the analog inputs to the computer. The boxes to control the motors for rotating the cylinders and raising and lowering the optics were digital electronics.

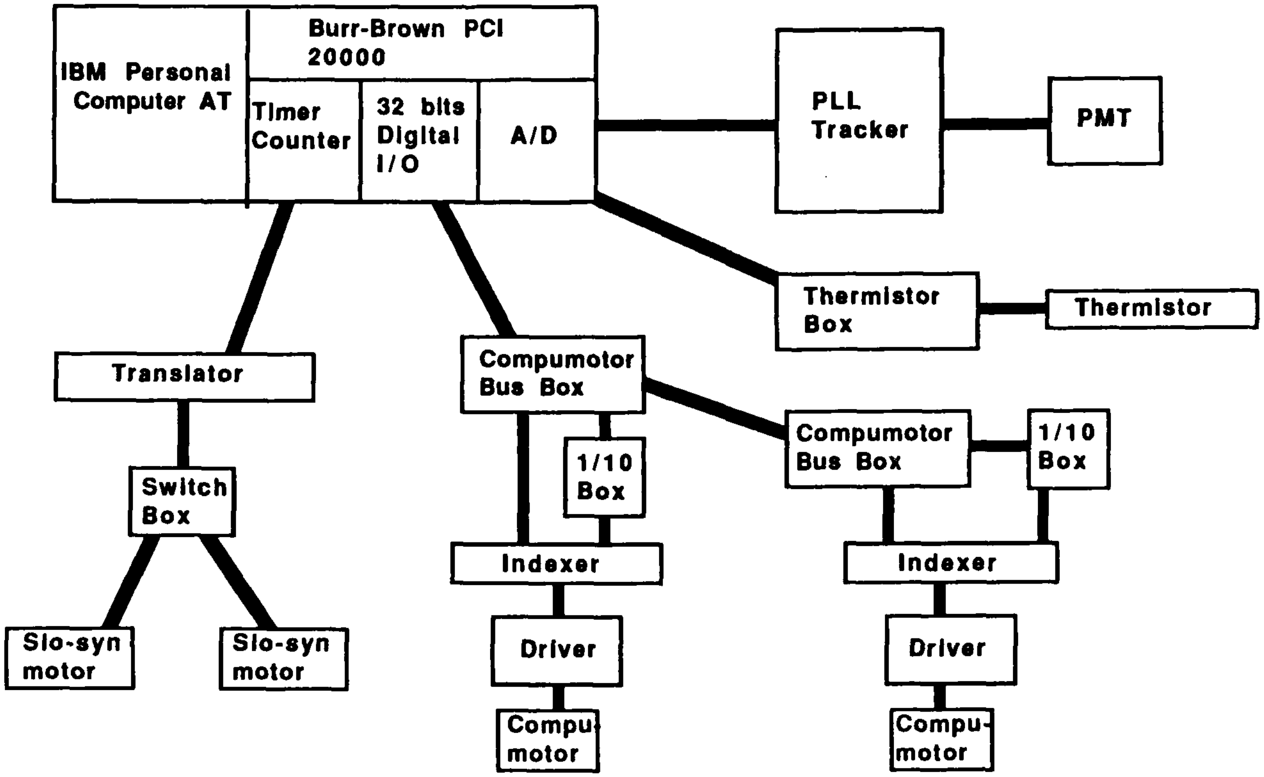

Figure 3.9 Digital Electronics Block Diagram

axial wavelength of approximately 2.60 cm. From previous studies it seemed likely that, for this state, the m_1 and m_2 values and the axial wavelength would remain the same throughout the range of parameters to be searched (Brandstater, 1984). The determined recipe, at least for an aspect ratio of 20 was:

1. Obtain Couette flow at about $R/R_c = 80$. Let the system sit for half an hour.
2. Increase R_{inner} to $10R_c$ with an acceleration of 85 R/R_c per minute. Let the system sit half an hour.
3. Take a frequency spectrum to ascertain that the appropriate $m_1 = 4$ state was obtained. Measure the axial wavelength to verify that it was about 2.6 ± .05 cm.
4. Increase R_{inner} to $11R_c$ by 85 R/R_c Reynolds numbers per minute.
5. Take a frequency spectrum to verify that $m_2 = 4$ was obtained.

Once the correct state was obtained, time series were taken for increasing inner cylinder Reynolds numbers. Typically each increase was 1 R_c for a range of R_{inner} from $11R_c$ to $15R_c$. In between each change in Reynolds number the system was allowed to rest about an hour. This also provided a convenient time to transfer files from the IBM PC-AT to the Ridge computer for data analysis. The maximum file length which could be obtained on the PC was 32768 integers due to the segmented architecture of the memory. Below $13R_c$ files of this length only were taken for dimension calculations. At 13_c and above 4 files each of 32768 integers were taken.

After the time series were taken at $R_{inner} = 15R_c$ the inner cylinder was returned to a Reynolds number of $11R_c$ at a rate of 0.085 R/R_c per minute. Then the aspect ratio was changed. Several routines were written to facilitate this change and are described in the appendix. The stepper motor which changed the aspect ratio was driven by ramping up the output of the rate generator of the Burr-Brown system, running at a constant rate for the necessary number of steps then decelerating to zero. The program "aspect" which controlled this process had as an input the number of steps per second of the constant rate section. This provided a controlled way of adjusting the way the aspect ratio was changed such that the axial wavelength was 2.60 cm. The m_1 and m_2 values seemed very insensitive to the process of aspect ratio changes. Basically, the aspect ratio was changed by one wavelength for each Reynolds number run. The recipe was:

1. Increase the aspect ratio by 4/5 the axial wavelength with the constant rate being 77 steps/second.
2. Increase the aspect ratio by 1/5 the axial wavelength with the constant rate being 10 steps/second.
3. Let the system rest 1.2 hour.

The axial wavelength was checked by locating adjacent outflow boundaries. First the LDV signal was averaged over 3000 points taken in 30 seconds. This was recorded and the location of the probe volume moved vertically 2 mm. The average LDV signal was again measured. The procedure was continued until an extremum was found. Figure 3.10 shows the result of this type of procedure for modulated wavy vortex flow at $R/R_c = 12.5$. In this figure the data points were taken every 0.05 inches. The outflow boundaries could be distinguished from the inflow boundaries since the outflow boundaries are sharper. Once an outflow boundary was found, the probe volume was moved 1.9 cm. and a search begun for another outflow boundary. Once two outflow boundaries were found, the program "fit" was run. "Fit" fitted each curve for the velocity profile at the boundary by a parabola and the wavelength was calculated as the distance between the extrema of the parabolas.

3.4 Viscosity Measurements

The viscosity was measured in two ways. The first was to use a Cannon-Fenske capillary viscometer. This viscometer was a glass U-shaped apparatus as shown in figure 3.11. In one arm of the U was a capillary tube. Above that was a reservoir. Below the lowest part of the capillary and in the other arm of the tube was another reservoir. A fixed volume of fluid was placed in the upper reservoir and held in place by a vacuum. The viscometer was then immersed in a water bath held at a temperature to $\pm.01\,^{\circ}C$ and allowed to equilibrate for 15 minutes. The vacuum was broken and the time it took the fluid to completely pass through the capillary was recorded. The viscosity was determined from this time as the

Figure 3.10 Axial wavelength measurement at $R/R_C = 12.5$ and an aspect ratio of 19.9. The signal is the result of a laser Doppler velocimetry (LDV) measurement of the radial velocity. Each data point consists of the average of 3000 measurements taken over a 30 second time interval. The LDV optics are mounted on an optical bench that is moved vertically by 0.05 inches by a lead screw for each data point. Notice that the outflow boundaries are much sharper than the inflow boundaries.

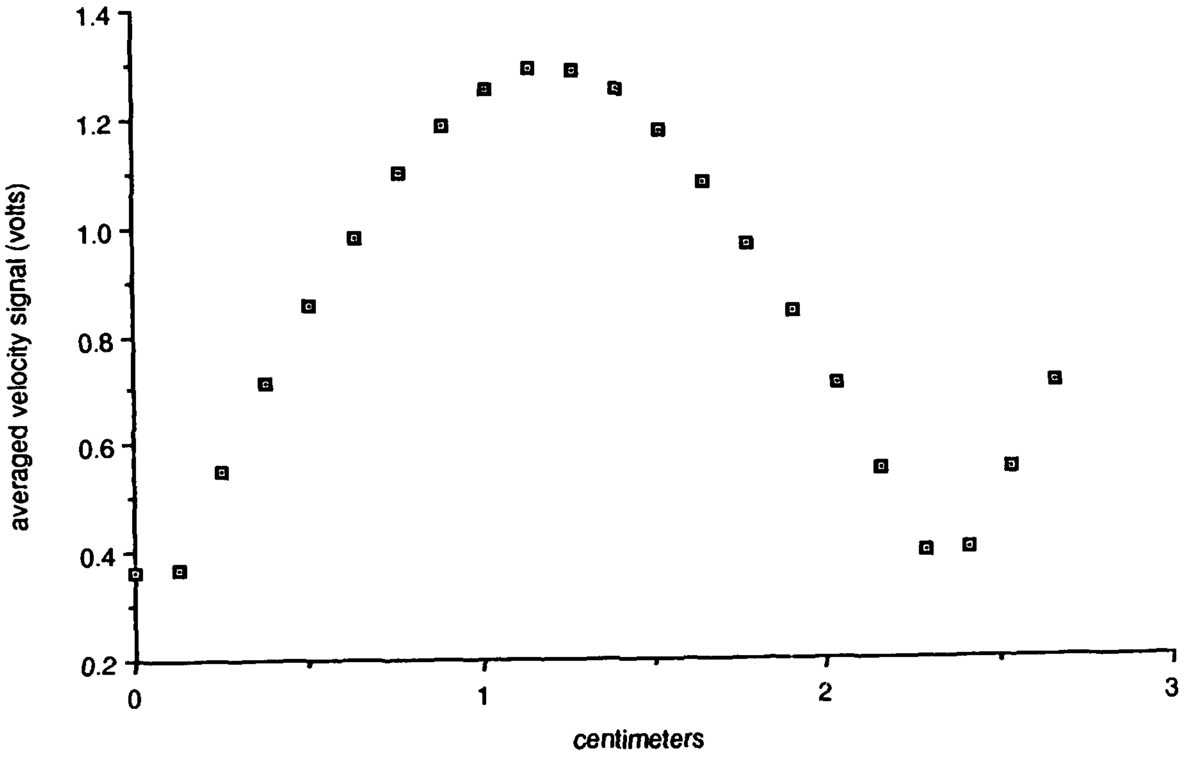

Fig 3.10 Axial wavelength measurement (R/Rc = 12.5)

viscometer was calibrated with a fluid of known viscosity at the factory. With care the viscosity measurements were repeatable to within about 0.2%. As viscosity is a function of temperature, the viscosity was measured over a range of temperatures from about 24°C to 26°C.

The second way the viscosity was determined was by finding the inner cylinder frequency at which the system made the transition to Taylor vortex flow from Couette flow. This was with the outer cylinder stationary. The transition was found by quasi-statically increasing the inner cylinder frequency until the transition occurred. This was then compared to the value of the Reynolds number for the system obtained from linear stability theory. Due to the electronics the smallest step in Reynolds number, and therefore the viscosity, obtainable was about 0.3% . The viscosity, compared to that obtained from the viscometer measurements, was usually about 1% too low. Linear stability theory assumes that the cylinder is infinitely long. Several previous studies of the dependence of the Taylor transition with aspect ratio suggest that the critical Reynolds number is larger for an infinite cylinder than one of finite length by an amount which is a function of the aspect ratio (Cole, 1976, Aider, 1983). If the infinite cylinder value was used to determine the viscosity, the calculated viscosity would have been too small. This would lead to Reynolds numbers obtained from the experimental frequencies which would be too large. Therefore the capillary viscometer method was the preferred method of determining the viscosity absolutely.

Figure 3.11 Cannon-Fenske routine capillary viscometer. This type of viscometer was used to determine the viscosity of the working fluid in these experiments. To fill the viscometer, it was inverted and tube A was placed in the fluid. A suction was applied to tube G until the fluid reached the upper fiducial mark. The suction was then removed and the tube inverted and placed in a temperature controlled bath. A closed tube was placed on tube A to prevent the fluid from draining down through the capillary to the collection reservoir. After sitting in the bath for 15 minutes the upper tube was removed. When the meniscus passed the upper fiducial mark the timer was started. The timer was turned off when the meniscus passed the lower fiducial mark. The time was then inserted into the calibration equation supplied with the viscometer and the viscosity calculated.

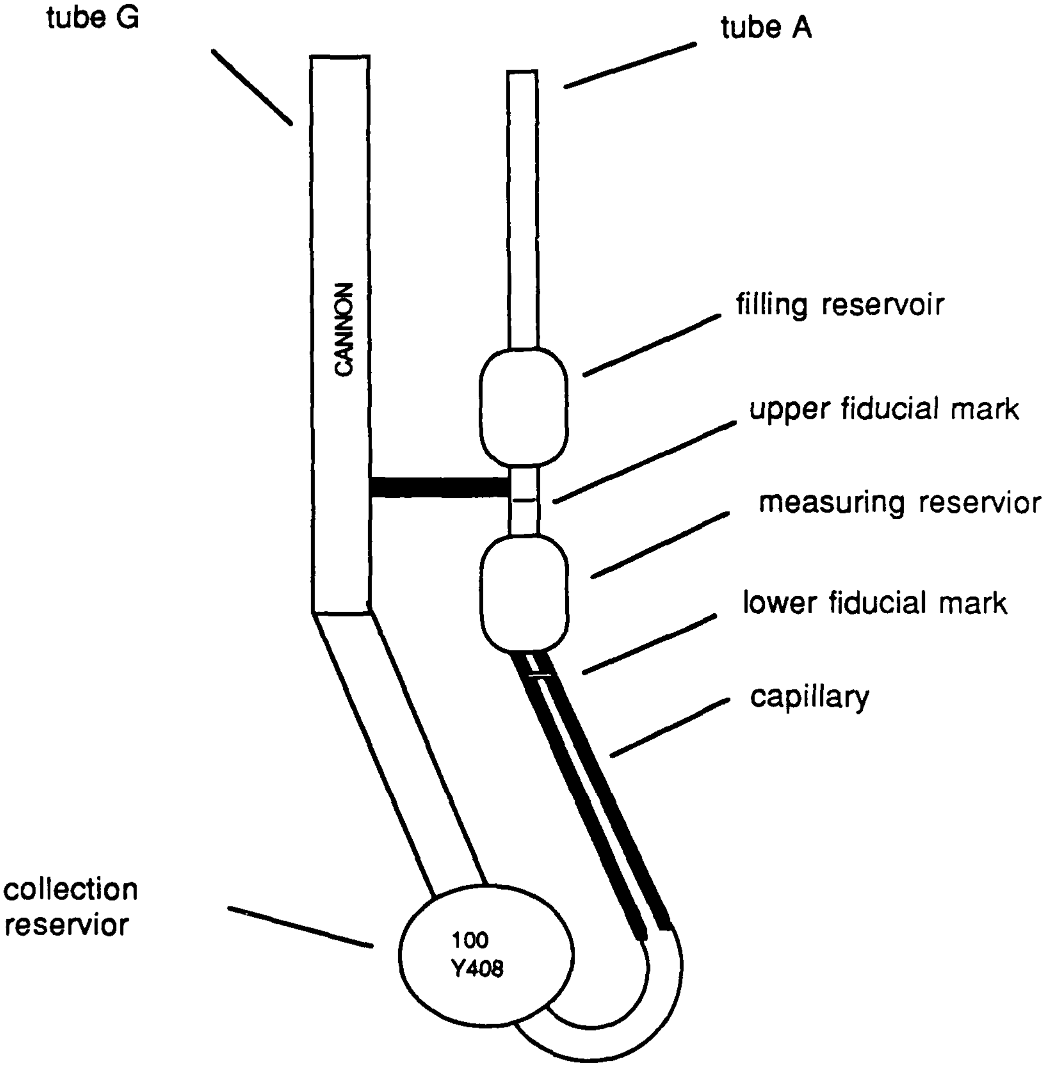

Figure 3.11 Cannon-Fenske routine viscometer

4. Bifurcation Studies

4.1 Introduction

A review of past experimental research is necessary to put the experimental results in perspective. The first paper to which all papers on the subject of the stability boundaries of Taylor-Couette flow must refer is Taylor's 1922 paper in the Philosophical Transactions of the Royal Society (Taylor, 1923). The theoretical aspects of this paper have been discussed in Chapter 1 of this dissertation. Here it is Taylor's experimental results which are of interest. His experimental efforts were directed at determining the location and form of the primary instability of Couette flow as a function of inner and outer cylinder frequencies. His results for the location of the primary bifurcation agreed within a few percent of his calculated values for the primary bifurcation from Couette to Taylor vortices Also, Taylor's experimental values agreed well with most of the experimental results published in the literature since then (Snyder, 1968(a)). The form the instability took most of the time was what is now known as Taylor vortices. His flow visualization was sufficient for him to have also described both spiral flow and what is now called wavy vortex flow.

Chronologically, the next experimental work of importance in the investigation of the primary bifurcation was that of Coles (Coles, 1965). Coles performed a study of the inner and outer cylinder Reynolds number parameter space in a Taylor-Couette system with a radius ratio of 0.874 and an aspect ratio of 27.9. The parameter space was quite large, the inner cylinder Reynolds number, R_i, falling in the range $0 \leq R_i/R_c \leq 20$ and the outer cylinder Reynolds number, R_o, falling in the range $-80 \leq R_o/R_c \leq 10$. He seemed to be interested in discriminating the regions of stability for laminar, periodic, quasiperiodic and turbulent flow. In particular, he observed that a spiral motion was typical of the Taylor instability for counter rotating cylinders for all but low outer cylinder velocities (Coles, 1965, p. 399). Oddly, he did not separate the periodic spiral flow from the time independent

Taylor vortex flow on his parameter space diagram nor did he seem to pursue the location of the bifurcation boundary between the two types of flow. This may have been beyond the capability of his equipment as his rotation speed stability was only 2-3 % in one cylinder rotation at the onset to Taylor vortex flow.

A more thorough study of the transitions in a smaller region in the inner and outer cylinder Reynolds number parameter space was performed by Snyder (Snyder,1968, 1968(a),1970). In three papers, he reported his own work in looking at the bifurcation boundaries. Also, he summarized the work of other investigators done through 1968. He showed that the location of the primary bifurcation as found by later experiments agreed well with Taylor's initial investigation. The particular importance of his work was in assigning the primary bifurcation for a sufficiently negative ratio of inner to outer cylinder frequencies to a transition from Couette flow to spiral flow. Thus he established spiral flow as a stable state. Snyder also compared his results with Krueger, Gross and DiPrima's stability calculations. Snyder found experimentally that for a Couette apparatus with a radius ratio of 0.95, the primary bifurcation change from Taylor vortices to spirals when the inner to outer frequency ratio, μ, was -0.766 ± 0.01. This agreed well with Krueger, Gross and DiPrima's theoretical value of -0.78 (Krueger, Gross, DiPrima, 1966).

Since the time of Snyder's research considerable theoretical work has been done which allows prediction of the parameters for transition to Taylor and spiral vortex flow for a finite radius ratio from the linear stability theory. The work most applicable to the experimental studies discussed in this dissertation has been performed by Chossat, Iooss and DeMay , Golubitsky and Stewart and Golubitsky and Langford. In particular, Golubitsky and Langford provided predictions of wave speed and wavenumber (Golubitsky, Langford, private communication). Because of these results a more careful study of the primary bifurcation for oppositely rotating cylinders was necessary for comparison with the predictions.

If the theory mentioned above were extended to allow nonlinear interactions, interesting new phenomena might be predicted. One of these phenomena could be hysteresis at bifurcation boundaries. This would arise if the bifurcation were subcritical. The existence of states created by mode competition in the neighborhood of the co-dimension 2 point where the primary transition changes from Taylor vortex flow to spiral vortex flow could also be a possibility. Such phenomena are seen in other non-linear problems. The required non-linear theory was unavailable at the time of this research. Nevertheless, a search for such phenomena could serve as a guide to and a verification of such a theory. So, the boundaries between the various flow states were examined for hysteresis and searched for possible new states arising from mode competition.

4.2 Results

The initial task was to determine the location of the primary bifurcation from Couette flow in the parameter space of the inner and outer cylinder Reynolds numbers. Figure 4.1(a) shows the determined location for the primary bifurcation. The reproducibility of the boundary locations was within the size of the Reynolds number step possible in the Gorman system i.e., 1/3 % of the Reynolds number. The accuracy was not quite as good as this, amounting to about 1 percent of the Reynolds number. The most probable source of error was in the viscosity determination, as discussed in chapter 3.

The results shown in figure 4.1(a) may be compared with calculations performed by Langford and Golubitsky (Langford et al., to be published). Their method, as discussed in chapter 2, was basically linear stability theory. As can be seen in figure 4.1(a), the results of their calculations for the primary bifurcation from Couette flow shows good agreement. The error in determining the viscosity may be responsible for part of the apparent systematic discrepancy. It also may be seen from figure 4.1(a) that the discrepancy between experiment and theory for the primary bifurcation became larger for smaller outer cylinder Reynolds numbers. This may be due to the Ekman pumping by the end boundaries (Snyder, 1968(a))

My data are compared with Snyder's experimental data in figure 4.1(b) (Snyder, 1968(a)). The agreement is good to 2% except at the co-dimension point on the primary bifurcation boundary where the stable flow after bifurcation changes from Taylor vortex flow to m=1 spiral vortex flow. Here Snyder's transition occurs at higher inner cylinder Reynolds number than mine. If Snyder's data were taken during too rapid an increase in the inner cylinder Reynolds number near the

Figure 4.1(a) A comparison of the experimentally determined location of the primary bifurcation for oppositely rotating cylinders with the linear stability analysis of Langford and Golubitsky. The error bars denote my experimental data and the line is an interpolated fit to the data calculated by Langford and Golubitsky. For my experimental data the aspect ratio was 30, the radius ratio was 0.8 and the inner cylinder radius was 4.759 cm. For Langford and Golubitsky's calculations the radius ratio was 0.8 and the length was assumed infinite with the structure in the fluid having a periodicity of a wavelength. (b) A comparison of the location of the primary bifurcation from my data with that of Snyder for oppositely rotating cylinders. The error bars denote my experimental data, the hollow squares are Snyder's data (Snyder, 1968) and the line is an interpolated fit to the data calculated by Golubitsky and Langford. For Snyder's data the aspect ratio was 76.86, the radius ratio was 0.8 and the inner cylinder radius was 5.032 cm.

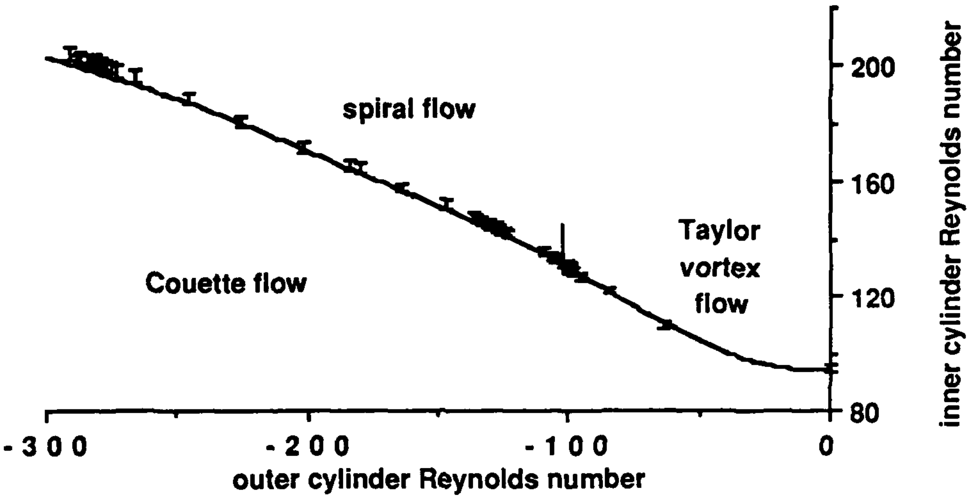

Figure 4.1 (a) Comparision of Experimental and Calculated Results

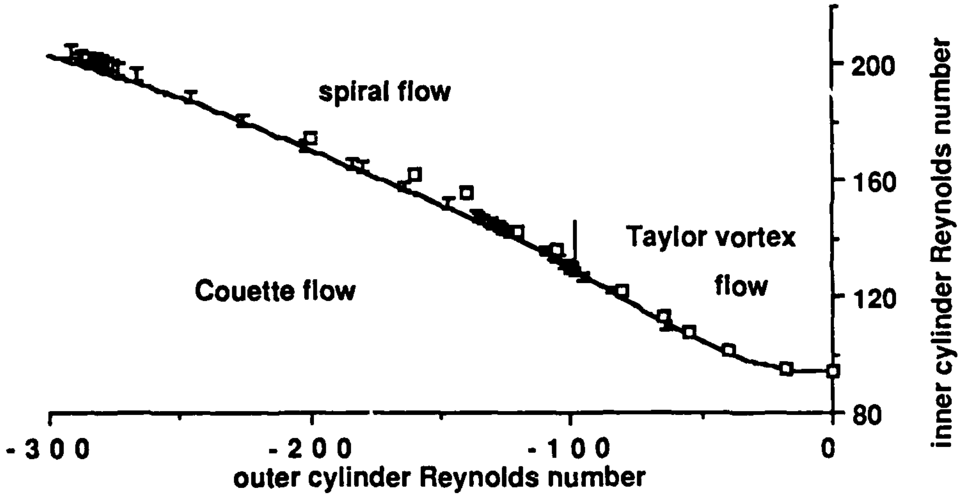

Figure 4.1 (b) Comparision of experimental with Snyder's results

co-dimension 2 point then this would have resulted in his data being too high in the vicinity of this point. The reason for suspecting this is that the transitions I observed near the co-dimension 2 point took nearly 1/2 hour to become stationary. Thus, increasing the inner cylinder Reynolds number too rapidly would result in a state becoming stable after the actual transition boundary had been passed

The observation that the time to reach an asymptotic state increases near the co-dimension 2 point seems to imply a kind of critical slowing down, in analogy with the critical slowing down for equilibrium phase transitions. This idea is supported by the fact that this time, the Snyder time, is proportional to the length of the fluid squared. If critical slowing down is involved then it is expected that the correlation length of the fluctuations should increase as the critical point is approached. However, in a finite system, the correlation length is limited by the actual physical size of the system; in my case, this is the length of the fluid in the cylinder. I observed that near the codimension 2 point the system did take approximately a Snyder time to become stationary (approximately 30 minutes).

In addition to locating the primary bifurcation, I was also interested in locating the points where the bifurcation changed to a different stable state, the so-called co-dimension 2 points. The experimentally determined locations are labelled on figure 4.2. It should be noticed that the states with higher azimuthal mode numbers ("m") appear at higher outer cylinder Reynolds numbers. This seems to be a general trend; that is, higher mode numbers are associated with the higher Reynolds numbers. This trend seems to hold both for axial and azimuthal modes. The data is bunched at the locations of the co-dimension 2 points since I was trying to locate these to within the accuracy of my experimental system.

Tables 4.1 and 4.2 show a comparison of the experimental determination of the transition points on the primary bifurcation with those calculated by Langford and Golubitsky (Langford et al., to be published). The agreement between the experimental and theoretical values was good for the first two transitions. The experimental error in these numbers was about ±1% (absolute), once again probably due to the viscosity problem. With this in mind, the experimental aspect ratio was apparently large enough such that the assumption of cyclic boundary conditions made in the theoretical analysis gave results close to the measured values for these

Figure 4.2 Location of the various azimuthal wavenumbers (m) on the primary bifurcation for oppositely rotating cylinders. The hollow triangles represent the transition to Taylor vortex flow, the cross represent the transition to m=1 spirals, the hollow diamonds represent the transition to m=2 spirals and the solid squares represent the transition to m=3 spirals. The line is once again an interpolated fit to the data calculated by Langford and Golubitsky. For my experimental data the aspect ratio was 30, the radius ratio was 0.8 and the inner cylinder radius was 4.759 cm. For Langford and Golubitsky's calculations the radius ratio was 0.8 and the length was assumed infinite with the structure in the fluid having a periodicity of a wavelength.

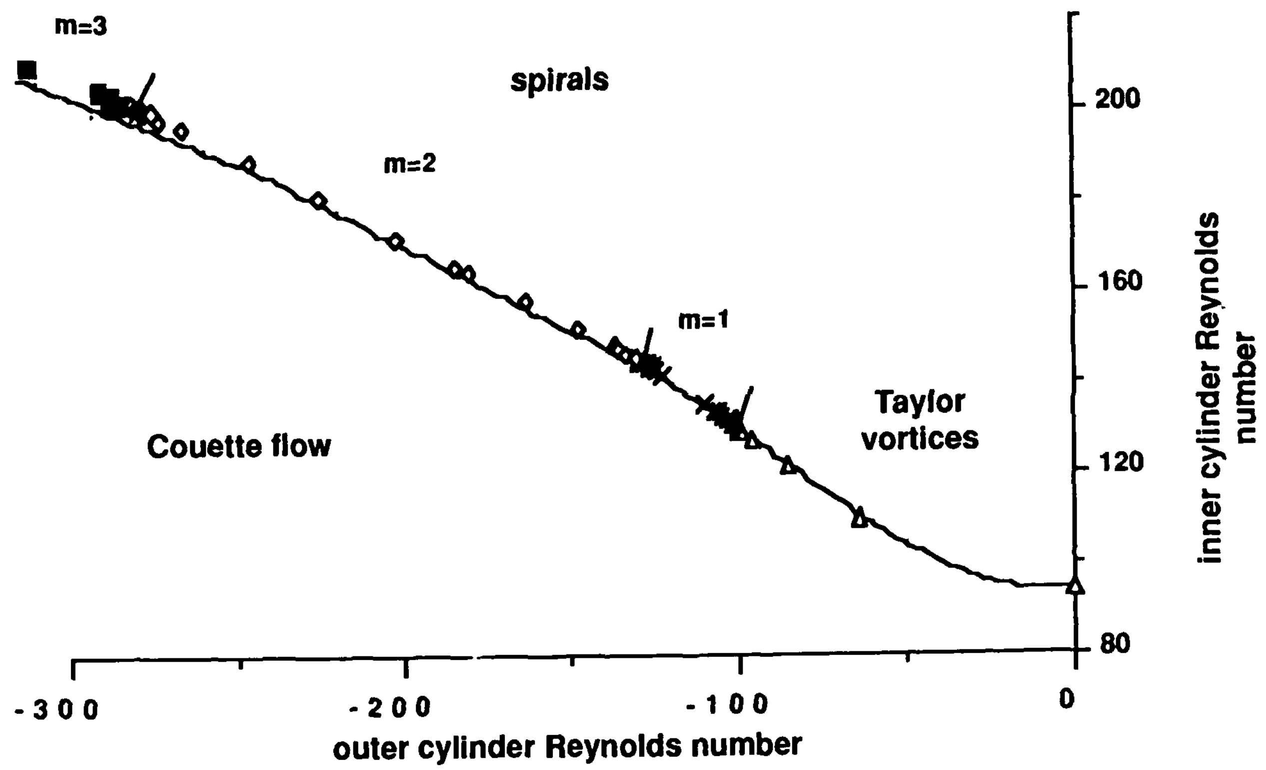

Figure 4.2 Location of azimuthal wavenumbers on primary bifurcation

	Experimental	Theoretical	%difference
R_i	131.0 ± .4	129.8	0.9 %
R_o	-100.7 ± .3	-99.75	0.9 %
$k_{(m=0)}$	3.59 ± .04	3.57	0.6 %
$k_{(m=1)}$	3.49 ± .03	3.55	-1.7 %
ω_1/Ω_i	0.339 ± .003	0.345	-1.8 %

m=0 → m=1 codimension 2 point

Table 4.1 Comparison of Computation and Experiment

	Experimental	Theoretical	%difference
R_i	145.3 ± .4	141.8	2.4 %
R_o	-130.2 ± .4	-124.6	4.4 %
$k_{(m=1)}$	3.55 ± .04	3.73	-5.5 %
$k_{(m=2)}$	3.78 ± .04	3.68	2.7 %
ω_1/Ω_i	0.364 ± .003	0.367	-0.8 %
$\omega_2/2\Omega_i$	0.332 ± .003	0.335	-0.9 %

m=1 → m=2 codimension 2 point

Table 4.2 Comparison of Computation and Experiment

transitions. The tables also give a comparison of the wavespeeds and axial wavenumbers on each side of the first two co-dimension 2 points. These values are determined when the associated states become stable upon crossing the bifurcation boundary. Also, these states should be as close to the boundaries between the different azimuthal modes as the Reynolds number resolution of the experimental system permits.

The wavespeeds are simply the azimuthal angular velocity of the waves normalized by the inner cylinder angular velocity. The simplest way to measure these wavespeeds is to take a time series of laser light backscattered from particles in the fluid and perform a Fourier transform. The azimuthal angular velocity is the fundamental frequency divided by the azimuthal mode number (number of azimuthal waves in one circumference). The error quoted (0.03 or 0.1% of the quoted value) is the resolution of the Fourier transforms. Since Taylor vortex flow is azimuthally symmetric there is no associated azimuthal wave speed. For the spiral flow with m = 1 the measured wave speed agreed within 2% with the calculated value at the first co-dimension 2 point. For m = 1 and m = 2 at the next co-dimension 2 point the agreement is better than 1%.

The agreement of the calculated values of the wavenumbers with the measured values was not quite as good. At the first co-dimension 2 point the computed wave numbers for the m = 0 and m = 1 disagreed by 0.6% and -1.7% respectively with the experimental values. At the second co-dimension 2 point the values were not as close. Experimentally the change in wavenumber from m = 1 to m = 2 spirals was opposite that predicted computationally. The calculated values disagreed with the measured values for m = 1 and m = 2 by -5.5% and 2.7% respectively. The experimental errors quoted in the tables are the standard deviations of the wavenumber measurements and are considerably less than the discrepancies between the measured values and the calculated ones.

If the wavenumbers are strong functions of the Reynolds numbers, then the disagreement could have resulted from the resolution being no smaller than 1/3 of a Reynolds number. In figure 4.3 I have plotted the wavenumber as a function of inner cylinder Reynolds number for an outer cylinder Reynolds number of -100.0. The wavenumbers do not change much except when the number of vortices

Figure 4.3 Axial wavenumber as a function of inner cylinder Reynolds' number for Taylor vortex flow with $R_o = -100.0$. The axial wavenumber is defined as $2\pi d/\lambda$ where d is the gap size and λ is the axial wavelength. There seems to be no trend with increasing Reynolds' number. The jump in wavenumber is due to a change in state from 32 to 34 vortices. The solid squares are for 32 vortices and the hollow squares are for 34 vortices. The error bars are the standard deviation of the measurements for each wavenumber. The wavenumbers were computed from the wavelengths measured on photographs of the flow as discussed in chapter 3. These data were taken with an outer cylinder Reynolds' number of -100.0 for increasing inner cylinder Reynolds' number. As with the previous figures the radius ratio at which this data was taken was 0.8, the aspect ratio was 30 and the inner cylinder radius was 4.759 cm.

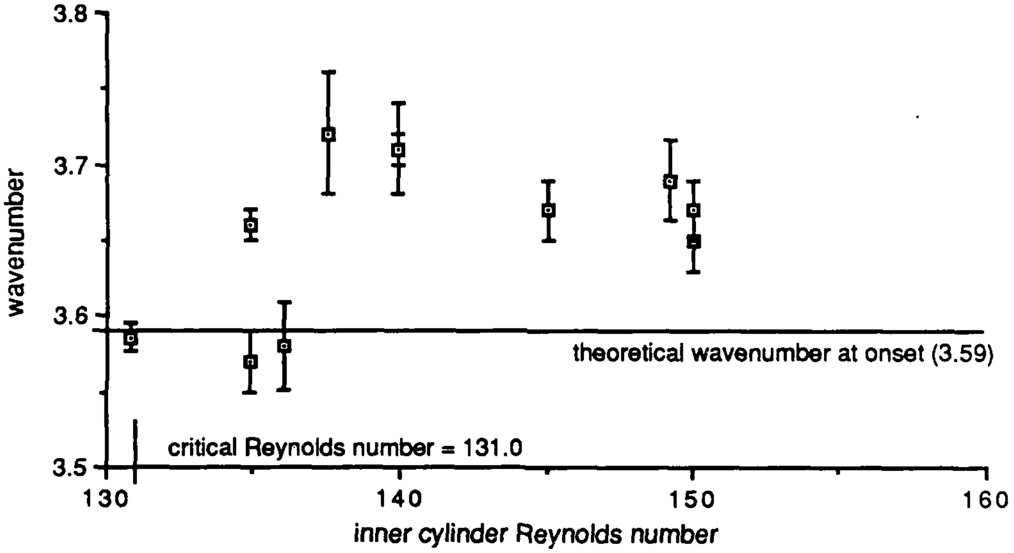

Figure 4.3 Axial wavenumber as a function of inner cylinder Reynolds number

changes. The only trend evident in the discrepancies is that the calculated values for the m=1 spirals are consistently above the measured values which might suggest a small error in the calculations. Any systematic experimental error should bias all the measured values the same way.

While locating the primary stability boundary I also searched for hysteresis in the bifurcation. Since it is possible for the transitions between states in Taylor-Couette experiments to exhibit hysteresis, the path taken in parameter space must be known for the results to be meaningful. My experimental procedure was to increase the outer cylinder speed to the speed of interest and then to increase the inner cylinder speed to obtain the transitions. The inner cylinder speed was reduced back to Couette flow in selected cases to search for hysteresis. No detectable hysteresis was found in the primary bifurcation. The hysteresis would have to have been greater than about 1/3 of a Reynolds number to have been detectable.

After looking at the primary bifurcation, I investigated the region around the first co-dimension 2 point. In this case I was interested in manifestations of mode interactions. An enlargement of this region where the primary bifurcation changes from Taylor vortex flow to m=1 spirals is given in figure 4.4. It was plainly evident that there was hysteresis in the boundary between spirals and TVF. The hysteresis region was traversed by varying the inner cylinder Reynolds number to higher and lower values for a fixed outer cylinder Reynolds number and also by varying the outer cylinder Reynolds number while keeping the inner Reynolds number fixed. The diagonally lined region is the area in parameter space where Taylor vortex flow and m=1 spiral flow were both stable states. More interesting effects, such as the generation of new states by mode interactions, were not observed. The lower boundary of the hysteresis region at an inner cylinder Reynolds number of approximately 132 represents the limits of my investigation. It is possible that this region extends to smaller inner and outer cylinder Reynolds numbers. It would be interesting to circle the codimension 2 point entirely to see if the spiral flow loses stability to Taylor vortex flow or Couette flow for decreasing inner cylinder Reynolds number below the codimension 2 point.

In these bifurcation studies, four objectives were accomplished. First, the primary bifurcation for counter-rotating cylinders was determined to an accuracy not

Figure 4.4 Hysteresis in the Taylor vortex spiral transition near the codimension 2 point. The hysteresis was determined by making transits through the shown region by increasing and decreasing either the inner or outer cylinder Reynolds' number and noting the locations of the transitions. The lower boundary of the hysteresis region at approximately an inner cylinder Reynolds' number of 132 represents the limits of my investigation. It is possible this region extends further down in inner and outer cylinder Reynolds' number. As with the previous figures the radius ratio at which this data was taken was 0.8, the aspect ratio was 30 and the inner cylinder radius was 4.759 cm.

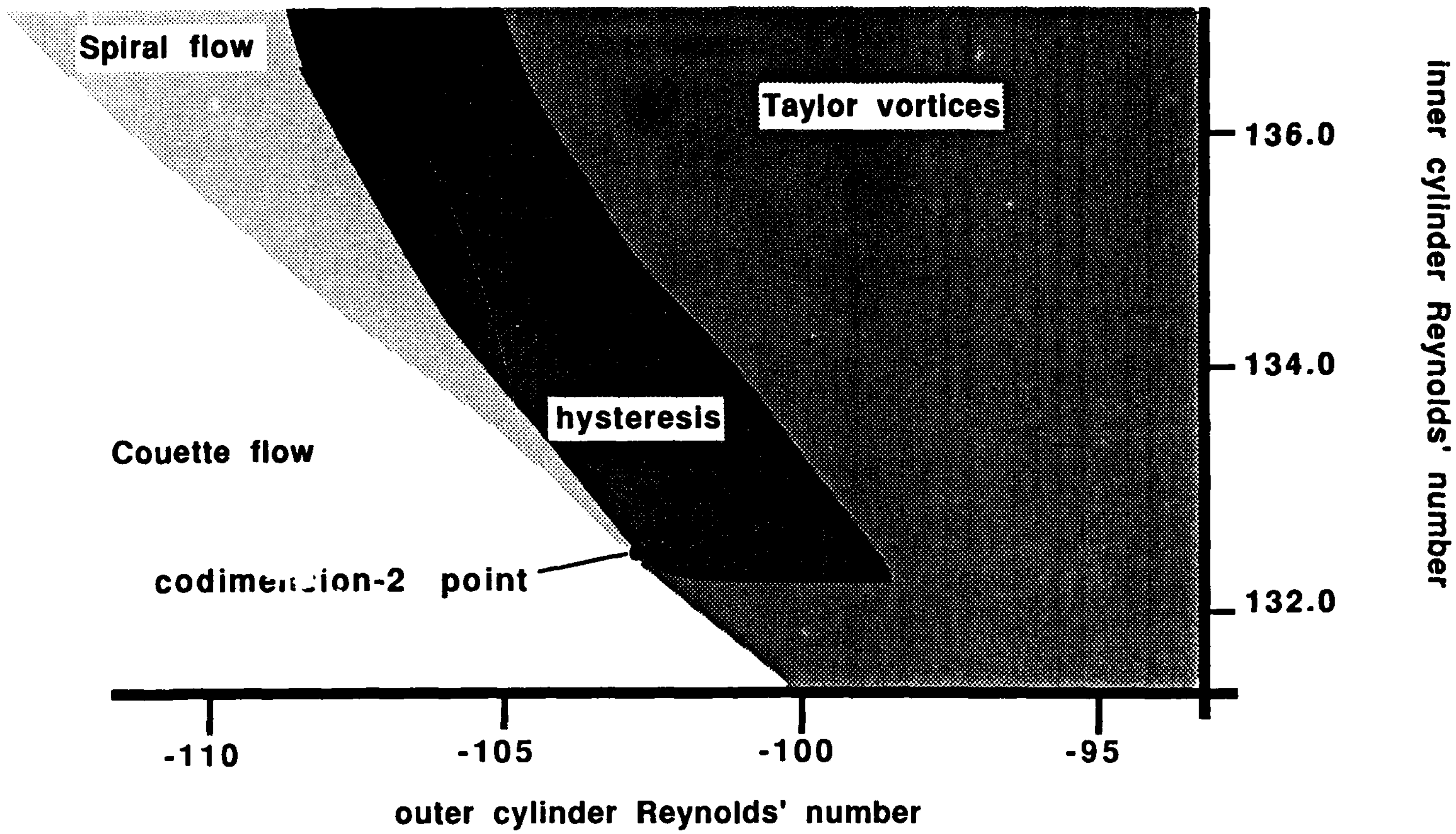

Figure 4.4 Hysteresis in the Taylor vortex - spiral vortex transition

previously attained. Secondly, measurements were made of wavespeed and axial and azimuthal wavenumber for the flow states near the codimension 2 points. The experimentally measured values were compared with theoretical calculations of Langford and Golubitsky. Thirdly, no hysteresis was found in the primary bifurcation. However, hysteresis on the order of four percent of the outer cylinder Reynolds number was found in the bifucation between Taylor vortices and m=1 spiral flow. Finally, the neighborhood of the first co-dimension 2 point was examined for states arising from mode interactions. No such states were found.

5. Aspect Ratio Experiment

5.1 Introduction

This research examined the attractor dimension as a function of aspect ratio. Why would such a dependence be expected? From a statistical mechanics point of view, increasing the size of the system increases the number of particles and so would increase the number of degrees of freedom associated with the particles' motions. One may also look at this question from a continuum mechanics point of view. Since the fluid flow is presumably governed by the Navier-Stokes equation, increasing the volume provides more points at which the behavior of the continuous fluid must be described, requiring more modes or degrees of freedom for the description. From the point of view of Kolmogorov turbulence theory (well developed turbulence; that is, turbulence at Reynolds numbers far beyond the transition boundary), the density of modes depends on the Reynolds number to the nine-fourths power ($R^{9/4}$) (see the last section of chapter 2). The total number of modes is the density times the volume of the system. So, there are indications that the attractor dimension should depend on the volume and hence on the aspect ratio.

The most important reason that these arguments are not necessarily valid is that they all assume a density of a large number of modes. The regime explored in this dissertation is the transition to turbulence, well below the regime in which such an assumption could be claimed to be appropriate. As has been shown in recent experimental work, the weakly turbulent flow is chaotic, not random, and involves only a small number of degrees of freedom (Brandstater et al., 1983). Fluid motion is then correlated locally for all length scales.

This does not preclude that in an extended fluid system there could be a correlation length in the fluid motion. Motion separated by more than the correlation length would then involve some different degrees of freedom. The fluid system would have more degrees of freedom as the system size increased, once some characteristic length in the system exceeded the correlation length. Similar ideas are discussed in the language of non-linear dynamics in a paper by Kurz and

Mayer-Kress (Kurz, Meyer-Kress, to be published). Basically, the idea is that if the spatial correlation decays for an extended physical system, the total dimension of a system will be larger than that measured locally. To obtain an intensive quantity, the authors define a dimension density, $D_2(x_0)$. The local dimension will just be this quantity integrated over a correlation "volume"; that is, integrated over a volume defined by the correlation length. The total dimension would involve integration over the entire system. So, it follows that as the system is increased the total dimension must increase correspondingly. The total dimension would be an extensive property. Similar ideas concerning spatially localized degrees of freedom have been discussed by Eckmann and Ruelle (Eckmann, Ruelle, 1985, Section V.A.1.c).

It is not obvious from theoretical considerations whether the flow has a finite correlation length smaller than the apparatus. The flow has well established spatial structures, namely the vortices, which reflect the symmetry of the apparatus. In photographs the flow appears well correlated. However, one could argue that the vortices themselves are independent spatial structures, each with a given dimension but each not correlated with the other. The system would have spatially localized degrees of freedom. This is shown not to be the case for wavy vortex flow in an experiment performed by Donnelly, Park, Shaw and Walden (Donnelly et al., 1980). This experiment was performed in a system with an aspect ratio of 80,for wavy vortex flow. The authors found the signals between two sensors in the flow to be well correlated throughout the flow provided there were no defects in the flow. This would argue against the idea put forth that an increase in the attractor dimension with aspect ratio would be due to a correlation length in the flow smaller than the characteristic system dimensions. Of course, this experiment should be conducted for chaotic flow to verify that these results hold in the regime of weak turbulence.

There are arguments which can support both the points of view that the attractor dimension should and should not depend on the aspect ratio. The support for either view is only suggestive. Without an experimental investigation of the Taylor-Couette flow, the question of the aspect ratio dependence of the dimension (or degrees of freedom) cannot be answered. The results of just such an investigation are discussed in the following section.

5.2 Results

The thrust of the experiment was to determine if there was an aspect ratio dependence of the attractor in Taylor-Couette flow. There was a large parameter space available for this study and a selection of the appropriate experimental parameters had to be made so that the experiment could be performed in a reasonable period of time. Additionally, there were some previously published results for the attractor dependence with Reynolds number for a given set of parameters (Brandstater, 1987). The parameters were chosen so that some comparison could be made with this previous work.

The parameters were chosen as follows. The radius ratio was 0.862. The inner cylinder Reynolds number ranged from $R/R_c = 10$ to $R/R_c = 15$ for the dimension determinations. The outer cylinder remained stationary throughout this part of the experiment. The data collected consisted basically of time series for each selected Reynolds number and aspect ratio. The aspect ratios were adjusted such that the axial wavelength was the same in all cases. The initial flow state was chosen to be a $m_1=4$, $m_2=4$ modulated wavy vortex flow with a normalized axial wavelength of 2.44, measured at the center of the cylinder. This state was chosen because, in a previous study, these parameters remained the same throughout the range of Reynolds numbers of interest (Brandstater, 1987). It was discovered as the experiment proceeded that this was a wise choice. A steady state could be obtained with the appropriate parameter values throughout the range of aspect ratio. Based on this, the available values of aspect ratio were 19.90, 22.33, 24.76, 27.19, 29.62, 32.04 and 34.48. No smaller aspect ratios were chosen because the end effects become too strong as the aspect ratio becomes smaller. In this study it was desired to investigate the effects of length in Taylor-Couette flow, not of velocity field modifications due to the no-slip boundary conditions at the ends. So, the aspect ratios were chosen equal to or greater than 19.90. Further experimental details may be found in chapter 2 and Appendix A.

5.2.1 Time series

The data actually collected were time series of the radial component of the fluid velocity at a point. The measurement volume was chosen near an outflow boundary and halfway between the inner and outer cylinders to maximize the measured velocity. The measurement volume was also located away from the upper and lower boundaries to minimize any end effects. Part of a typical set of time series for a system with an aspect ratio of 22.33 and for Reynolds numbers $R/R_C = 11, 12, 13, 14$, and 15 is shown in figure 5.1. Each plot represents 512 points. The flow starts at a Reynolds number of 11 in quasiperiodic flow. Though it is not obvious in the plots that there were only two frequencies associated with the flow, there are no sharp changes that might be associated with turbulence. As the Reynolds number was increased, small scale structure appeared and was particularly evident at $R/R_C = 15$. At this Reynolds number the fluid was definitely chaotic, as will be shown latter.

5.2.2 Frequency Spectra

Perhaps a better idea of the state of the fluid can be obtained from the frequency spectra. The frequency spectra were obtained from the time series by Fast Fourier transform methods. The spectra were normalized such that the integral of a power spectrum was equal to the variance of the velocity time series. In figure 5.2 appear the corresponding frequency spectra for the time series in figure 5.1. In the first spectrum, corresponding to the time series for $R/R_C = 11$, there are only two frequencies, their harmonics and a few sum and difference frequencies; all are well above a flat, experimentally noisy background. As the Reynolds number is increased, the familiar behavior of a system making the transition to chaos is evident: the background rises well above the instrumental noise. The background is not measurement noise; it is the frequency components of the dynamical system. It is due to the fact that the system is no longer composed of a finite number of periodic states. As was shown by Dr. Brandstater and will be shown later in the dissertation, the flow is truly chaotic. It should be pointed out that the broad chaotic background which appears for the higher Reynolds numbers decreases linearly with increasing frequency until it disappears in the experimental noise. Since the plots of frequency are semi-logarithmic, the chaotic background decays exponentially with frequency. It has been shown that the broad background arising from a deterministic, chaotic system will decay exponentially with frequency but that the background due to a random process will obey a power law (Sigeti, Horsthemke 1987). The spectra for

Figure 5.1 Plots of the time series as a function of Reynolds number at fixed aspect ratio. The radius ratio was 0.862. Each plot is the first 512 points out of a time series of 32K points. The horizontal axis is in units of one inner cylinder period, T_i. Notice that the plots have more sharp, rapid changes as the Reynolds number increases, denoting transition to more complex states.

(a) $R/R_c = 11$, Aspect ratio = 22.3

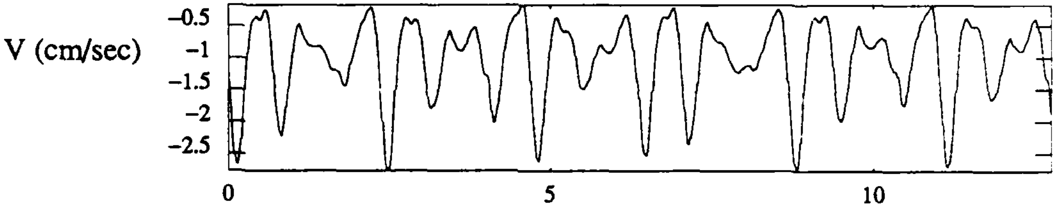

(b) $R/R_c = 12$, Aspect ratio = 22.3

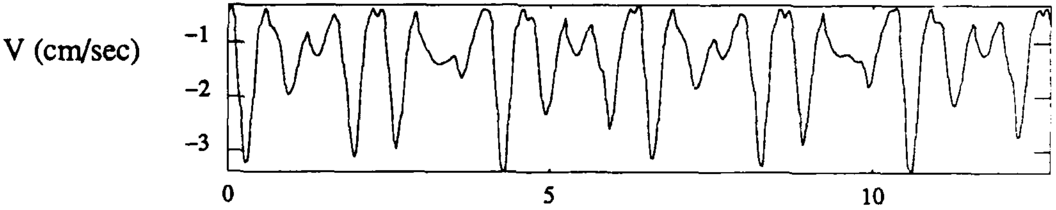

(c) $R/R_c = 13$, Aspect ratio = 22.3

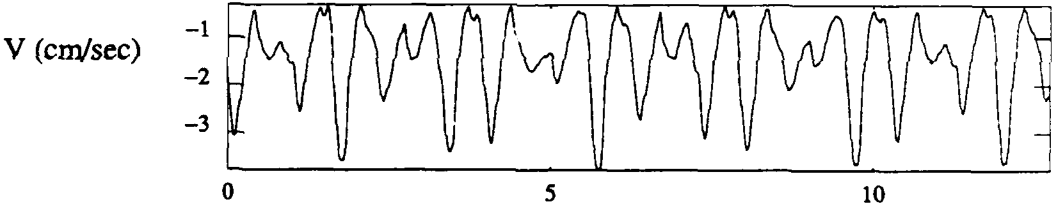

(d) $R/R_c = 14$, Aspect ratio = 22.3

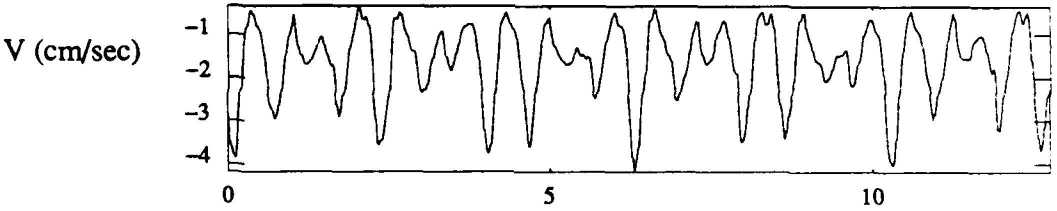

(e) $R/R_c = 15$, Aspect ratio = 22.3

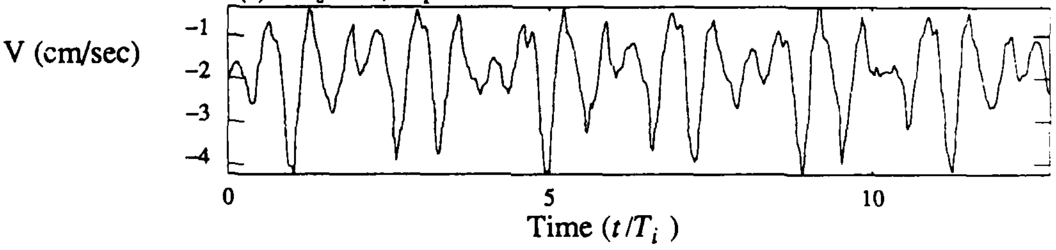

Figure 5.2 Plots of the frequency spectra as a function of Reynolds numbers at fixed aspect ratio. The radius ratio 0.862. The horizontal units are in terms of the inverse of the inner cylinder period, $f_i = 1/T_i$. The population of the sharp spectral peaks does not seem to change with an increase in Reynolds number but the increase in the background due to the aperiodicity of the flow at higher Reynolds numbers is clearly evident.


(a) $R/R_c = 11$, Aspect ratio = 22.3

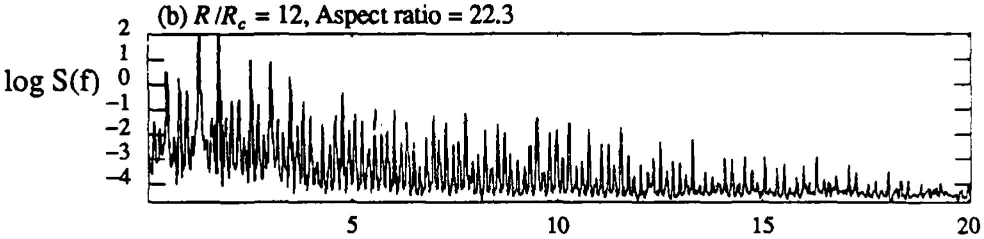
(b) $R/R_c = 12$, Aspect ratio = 22.3

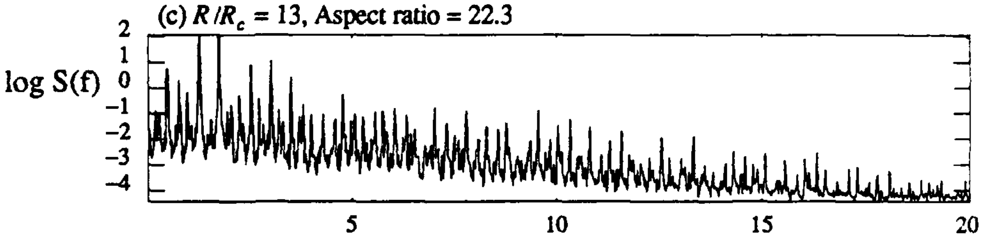
(c) $R/R_c = 13$, Aspect ratio = 22.3

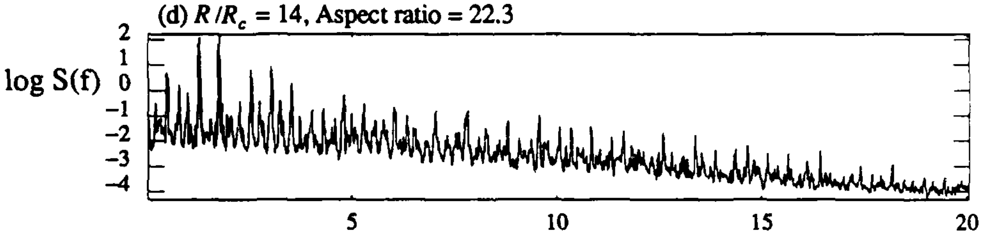
(d) $R/R_c = 14$, Aspect ratio = 22.3

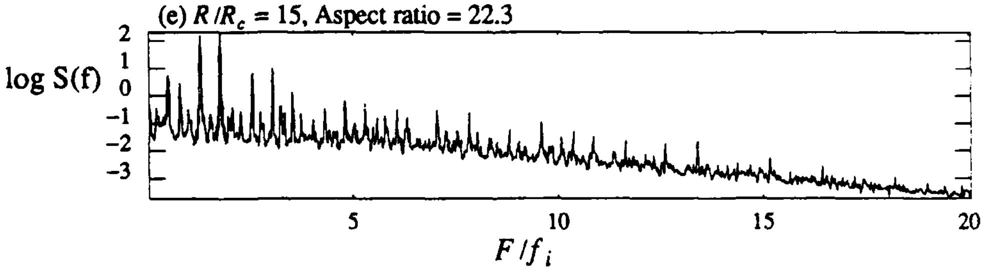
(e) $R/R_c = 15$, Aspect ratio = 22.3

increasing Reynolds number are behaving as the spectra for a system making a transition to turbulence.

An interesting observation can be made by examining a series of the power spectra for the same Reynolds number and various aspect ratios. Such a series of plots appears in Figure 5.3. The Reynolds number for these data was $R/R_c = 13$ and the aspect ratio varied from 19.90 to 34.48. The frequencies, F, are normalized by the inner cylinder frequency, f_o, to eliminate the purely numerical effect of the increasing cylinder frequency. It is seen that the background remains essentially the same for all values of the aspect ratio. The peaks also remain sharp but the higher harmonics are populated more for larger aspect ratios. This may be seen quantitatively in figure 5.4. Plotted here are the number of peaks in the upper fourth of the spectra, that is, between 15 F/f_o and 20 F/f_o which equalled or exceeded an intensity of one order of magnitude above the noise. It is seen that for $R/R_c = 11$ and $R/R_c = 13$ the number of peaks increases dramatically for the first two aspect ratios and then remains more or less constant. Small scale noise shows up in the spectra as higher harmonics of the periodic flow states. This is similar to most physical non-linear systems which show increasing harmonic content as they are driven harder. Physically, this may be due to the reduced influence of the ends in constraining the flow for the large aspect ratios. These observations would tend to support the idea that the dimension of the attractor for the flow is not changing with aspect ratio. For $R/R_c = 15$ a trend is not as apparent. Probably most of the energy that was being coupled out to the higher harmonics is now being fed into the background.

A further observation can be made. The wavespeeds can be derived from the frequency data. The wavespeeds are simply the inverse of the time it takes a wave in the flow to go around the circumference once. It is easily seen that for an $m_1 = 4$ state the wave speed is just the fundamental frequency associated with this state divided by the number of waves in a circumference (namely, 4). Likewise for an $m_2 = 4$ state the wave speed is just the second fundamental frequency divided by 4. In figure 5.5(a) are the wavespeeds (S_1) verses aspect ratio for $R/R_c = 11, 12, 13, 14$, and 15. As can be seen the wavespeeds are tending toward an asymptote as the aspect ratio increases. The change in the wavespeed between the last two values of aspect ratio for any of the Reynolds numbers is smaller than .01%. The error is

Figure 5.3 Plots of the frequency spectra at $R/R_C = 13$ for aspect ratios 19.90 to 34.48. The radius ratio was 0.862. The horizontal units are in terms of the inverse of the inner cylinder period. The increase of the higher harmonics with aspect ratio for the first three ratios is clearly shown. Notice also that there is no increase in the background with aspect ratio.

(a) R/R_c = 13, Aspect ratio = 19.9

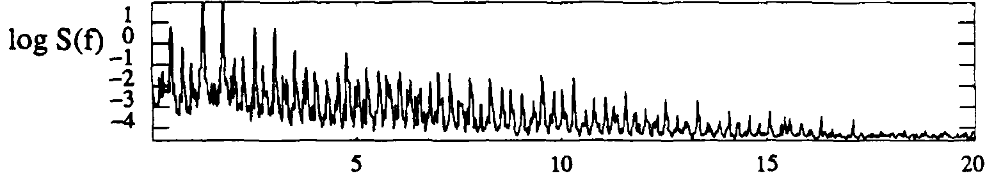

(b) R/R_c = 13, Aspect ratio = 22.3

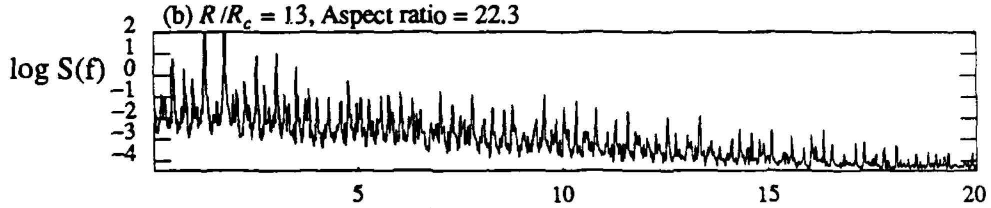

(c) R/R_c = 13, Aspect ratio = 24.8

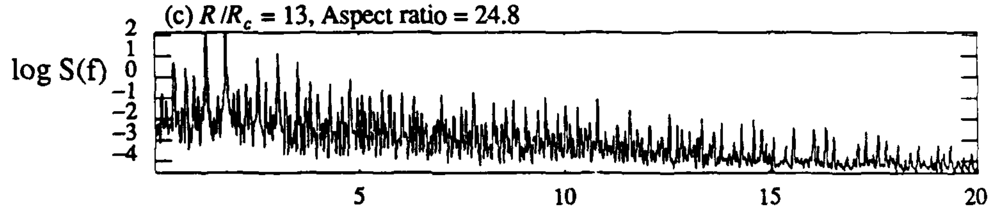

(d) R/R_c = 13, Aspect ratio = 27.2

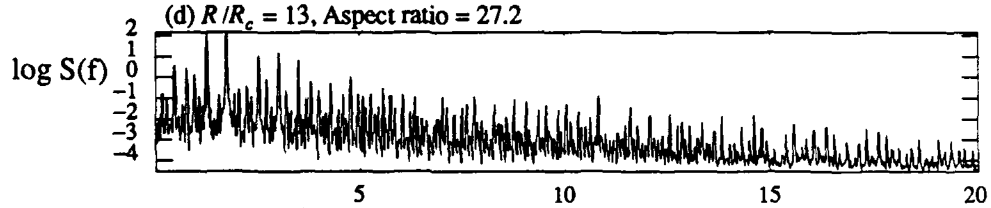

(e) R/R_c = 13, Aspect ratio = 29.6

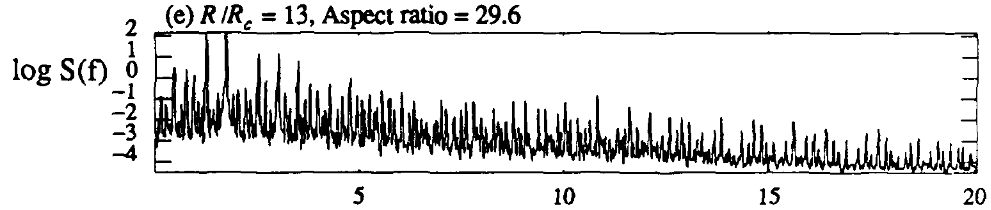

(f) R/R_c = 13, Aspect ratio = 32.0

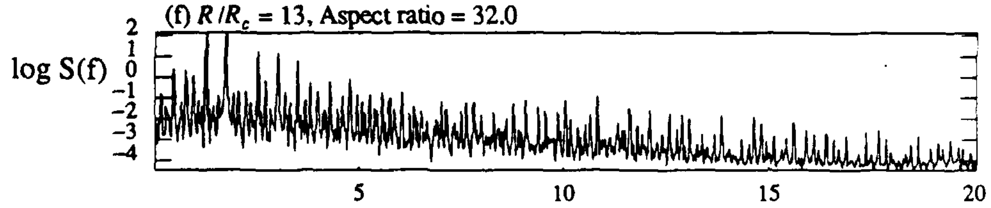

(g) R/R_c = 13, Aspect ratio = 34.5

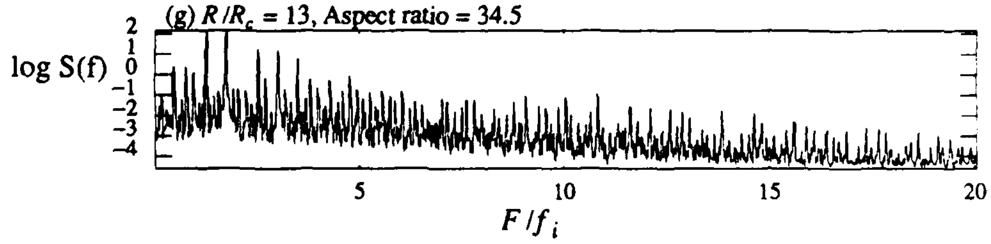

Figure 5.4 Number of higher harmonics vs. aspect ratio. The data are plotted for Reynolds number of 11, 13, and 15. The vertical axis represents the number of harmonics which are at least an order of magnitude above the noise and fall within the upper quarter of the frequency range of the spectra. For Reynolds numbers of 11 and 13 there is a trend toward a limiting number of higher harmonics as the aspect ratio increases. For a Reynolds number of 15 the trend is not as clear. However, it is clear it is not a strong function of the aspect ratio. The frequencies used here are normalized by the inner cylinder frequency so that the effects seen are not merely due to the fundamental frequencies becoming larger.

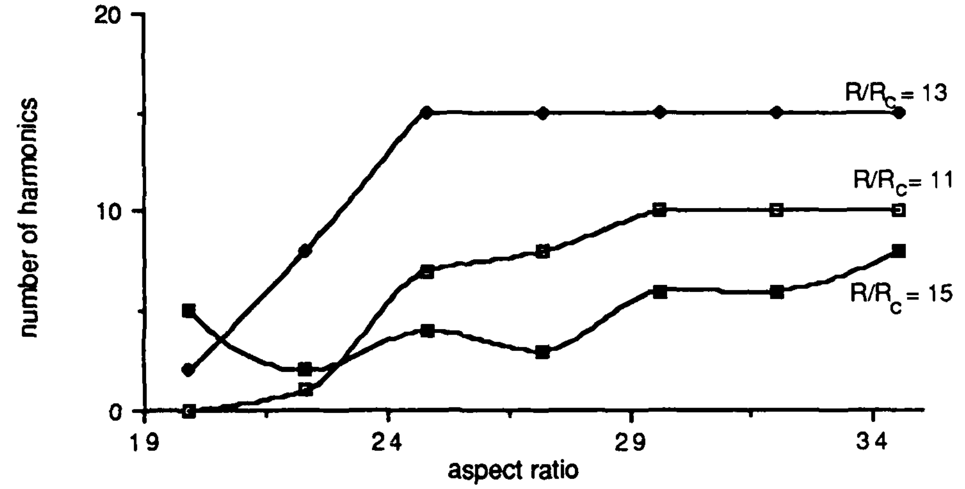

Figure 5.4 Number of higher harmonics vs. aspect ratio

between .1% and .2%. Likewise, a plot of the aspect ratio dependence of the wavespeed (S_2) associated with the mode $m_2 = 4$ is shown in figure 5.5(b). Here the wavespeed (S_2) approaches an asymptote for all the Reynolds number within the error of the experiment. Finally, figure 5.6 is a plot of the ratio of the wavespeeds (S_2/S_1) as a function of aspect ratio. As expected the ratios also approach an asymptote. The point of this is that the wavespeeds are becoming independent of the aspect ratio as the aspect ratio increases. Here are indications that the flow is independent of the aspect ratio if the aspect ratio is large enough. A study showing similar results for the wave speeds was performed by King et al.(1984).

The dependence of the wavespeeds on aspect ratio can be fit to a variety of functions of $1/\Gamma$. Two functions used by King et al. (1984) were:

$$s_1(\Gamma) = s_1(\infty) + \frac{\alpha}{\Gamma} \qquad (5.1)$$

and:

$$s_1(\Gamma) = s_1(\infty) + \frac{\beta}{\Gamma} \exp - \frac{\Gamma}{l} \qquad (5.2)$$

A non-linear least-squares method (Levenberg-Marquardt method (Press et al.,1986) was used to fit my data to these equations. The results are given in Tables 5.1 (a) - (d). The fits are fairly good, the rms % deviation being less than 0.02 % for most cases. Equation 5.1 seems to provide a better fit than equation 5.2 for both wavespeeds s_1 and s_2. The goodness of the fits supports the assertion that the wavespeeds are approaching asymptotic values as the aspect ratio increases. Quantitative comparison with the results of King et al.(1984) would not be meaningful since the experimental parameters are somewhat different ($\lambda/d = 2.4$ and radius ratio = 0.868 for the King paper compared to $\lambda/d = 2.44$ and radius ratio = 0.862 for my experiment). Qualitatively, the wavespeeds from the King paper approached an asymptotic value for increasing aspect ratio from above rather than from below as in my data. This is probably due to the difference in the experimental parameters.

5.2.3 Attractor Reconstruction

As explained in chapter 2, one may reconstruct the attractor from a time series. The idea was to create vectors from the time series, each vector element chosen by a

Figure 5.5 (a) Plots of the wavespeed (s_1) associated with the wavenumber $m_1 = 4$ as a function of aspect ratio. (b)Plots of the wavespeed (s_2) associated with the wavenumber $m_2 = 4$ as a function of aspect ratio. Notice the asymptotic trend toward a constant value as the aspect ratio increases for both wavespeeds. The hollow squares with a center dot represents $R/R_c = 11$, the filled diamond represents $R/R_c = 12$, the filled square represents $R/R_c = 13$, the hollow diamond represents $R/R_c = 14$, and the star represents $R/R_c = 15$. The radius ratio is 0.862.

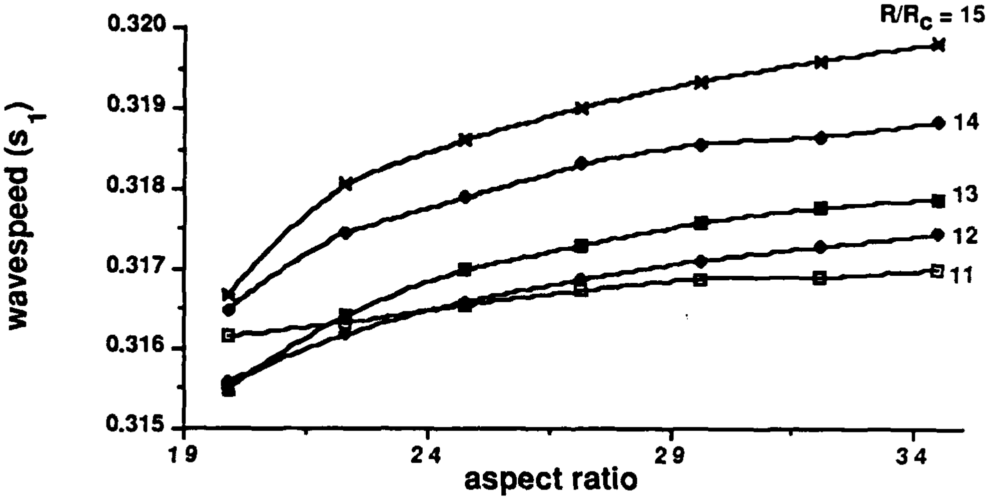

Figure 5.5(a) s_1 (wavespeed) vs aspect ratio

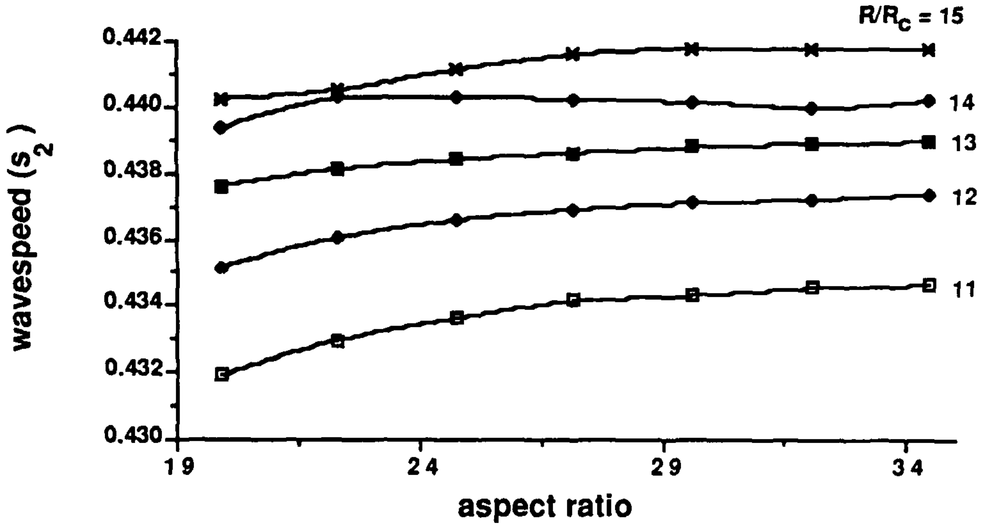

Figure 5.5(b) s_2 (wavespeed) vs aspect ratio

Figure 5.6 Plots of the wavespeed ratio (s_2/s_1) associated with the wavenumbers $m_1 = 4$ and $m_2 = 4$ as a function of aspect ratio. The hollow squares with a center dot represents $R/R_c = 11$, the filled diamond represents $R/R_c = 12$, the filled square represents $R/R_c = 13$, the hollow diamond represents $R/R_c = 14$, and the star represents $R/R_c = 15$. The radius ratio is 0.862. Here the ratio of wavespeeds are approach a constant value with aspect ratio. It is interesting to note that the sign of the trend depends on Reynolds number.

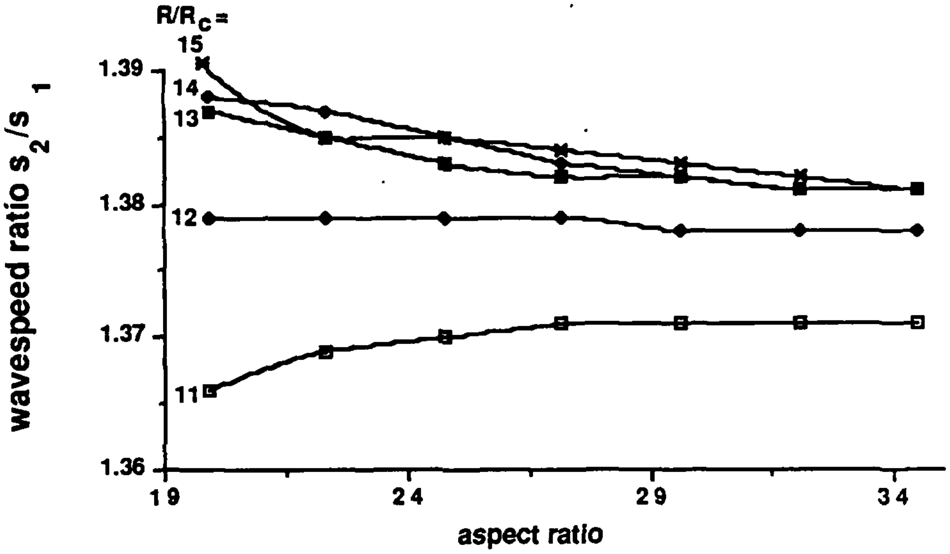

Figure 5.6 s_2 / s_1(wavespeed ratio) vs aspect ratio

R/R_c	λ/d	$s(\infty)$	α	rms % deviation
11	2.44	0.318	0.041	0.0027
12	2.44	0.320	0.087	0.0048
13	2.44	0.321	0.110	0.0117
14	2.44	0.322	0.107	0.0123
15	2.44	0.324	0.139	0.0163

a). aspect ratio dependence for wave speed s_1

R/R_c	λ/d	$s(\infty)$	α	rms % deviation
11	2.44	0.439	0.127	0.0119
12	2.44	0.440	0.102	0.0097
13	2.44	0.441	0.062	0.0042
14	2.44	0.441	0.024	0.0161
15	2.44	0.444	0.081	0.0101

b). aspect ratio dependence for wave speed s_2

Tables 5.1(a) & (b) Fit of the Aspect Ratio Dependence
of the Wave Speed to Equation 5.1

R/R_c	λ/d	$s(\infty)$	β	l	rms % deviation
11	2.44	0.317	0.053	29.5	0.0026
12	2.44	0.319	0.111	33.5	0.014
13	2.44	0.319	0.154	20.4	0.016
14	2.44	0.320	0.156	15.1	0.040
15	2.44	0.321	0.204	5.97	0.16

c). aspect ratio dependence for wave speed s_1

R/R_c	λ/d	$s(\infty)$	β	l	rms % deviation
11	2.44	0.439	0.100	83.5	0.123
12	2.44	0.440	0.082	73.8	0.098
13	2.44	0.441	0.033	76.1	0.126
14	2.44	0.441	0.022	50.5	0.040
15	2.44	0.444	0.080	55.1	0.041

d). aspect ratio dependence for wave speed s_2

Tables 5.1(c) & (d) Fit of the Aspect Ratio Dependence
of the Wave Speed to Equation 5.2

time delay. Such a set of vectors, if properly chosen will span the space in which the attractor was reconstructed. The first thing done after obtaining the time series was to find the appropriate time delay for reconstructing the attractor. As discussed in chapter 2, this involved calculating the mutual information or mutual redundancy (a generalization of mutual information).

The mutual redundancy computed for one of my data sets appears in Figure 5.7 . The computer code used for these computations was kindly provided by Mr. Andrew Fraser of the Center for Nonlinear Dynamics at the University of Texas at Austin. It can be seen that there were several minima in the numbers. It is usually advisable to use the first or second minimum since otherwise the attractor gets folded upon itself and it becomes difficult to extract information. The ideal delay depended on the Reynolds number and aspect ratio and was chosen accordingly (Fraser, to be published; Fraser, Swinney, 1986).

Having chosen the time delay one can reconstruct the attractor. For the figures that follow, the phase space dimension was obviously limited to three so the projections of the attractors could be presented in two-dimensions. Higher dimensional attractors were reconstructed for the dimension calculations. The software reconstructed the attractors by simply taking the first element in each of the time delay vectors as the first location on the attractor. The following points were generated by then taking the second points of the vectors, then the third points and so forth. If the attractor was embedded in three dimensions it was plotted. Additionally, Poincaré sections are presented for these attractors. Lines are drawn to show where the sections are taken.

Figures 5.8 (a) and (b) show the attractor reconstructed for $R/R_c = 11$ and an aspect ratio of 22.33 with an associated Poincaré section. At this Reynolds number the attractor should be a torus. That this is so is seen in the figure. The thickness of the Poincaré section is due to experimental noise. Ideally, the torus surface should be a 2-dimensional sheet. From this thickness one can derive a value for the rms fluctuation of the noise and compare it to the values previously calculated in the experimental section. This value was about 3.7% or slightly less than 5 bits. This value is about that estimated in the next section, which was 3%.

Now one can consider the evolution of the attractor and an associated Poincaré section with Reynolds number. Figures 5.8(a)-(j) show the attractor and a Poincaré

Figure 5.7 A graph of the mutual redundancy verses time delay for the time series ccc133. The time delay ranged from 5 to 25 sampling intervals and the embedding dimension was 3. The sampling interval was (0.0249 $T_{i)}$. The aspect ratio was 27.19 and R/R_c = 15. The radius ratio was 0.862.

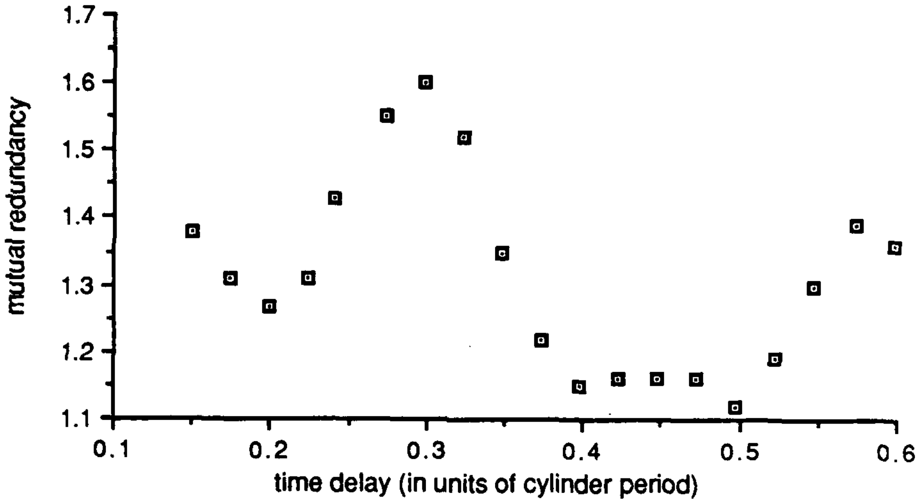

Figure 5.7 Mutual reduncancy vs. time delay

Figures 5.8(a)-(j) Attractors and Poincaré sections for an aspect ratio of 22.33. These figures show the reconstructed attractors and an associated Poincaré section as a function of Reynolds' number. Figures 5.8(a) and (b) are for $R/R_c = 11$. Figures 5.8(c) and (d) are for $R/R_c = 12$. Figures 5.8(e) and (f) are for $R/R_c = 13$. Figures 5.8(g) and (h) are for $R/R_c = 14$. Figures 5.8(i) and (j) are for $R/R_c = 15$. The radius ratio was 0.862. These figures were derived from the same data sets as the associated time series in Figure 5.1 and frequency spectra in Figure 5.2. The attractors were constructed in three dimension, of which these pictures represent a two dimensional projection. The designated lines on the attractors show where the Poincaré section were taken.

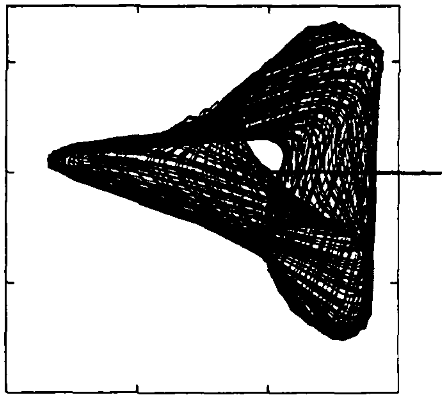

(a) R/R_c = 11, aspect ratio = 22.3

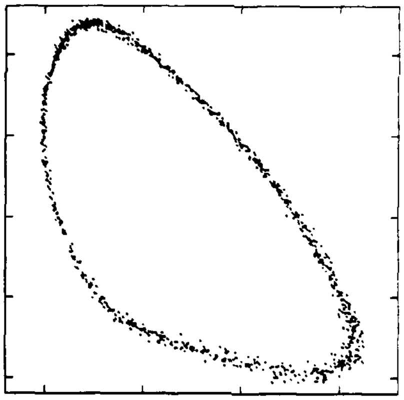

(b) R/R_c = 11, aspect ratio = 22.3

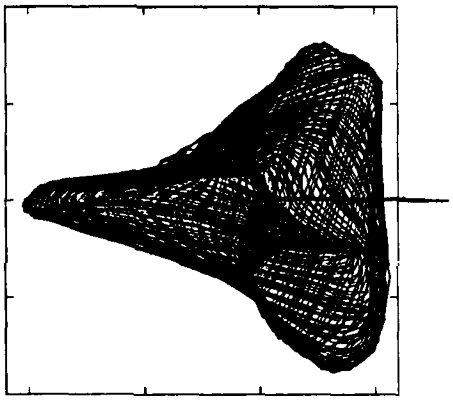

(c) R/R_c = 12, aspect ratio = 22.3

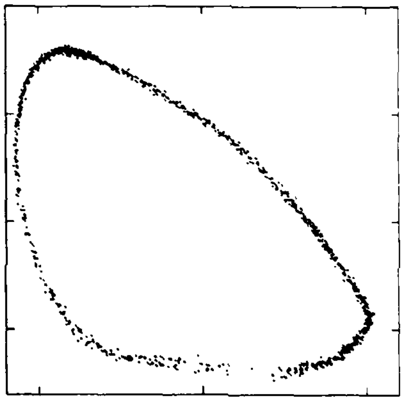

(d) R/R_c = 12, aspect ratio = 22.3

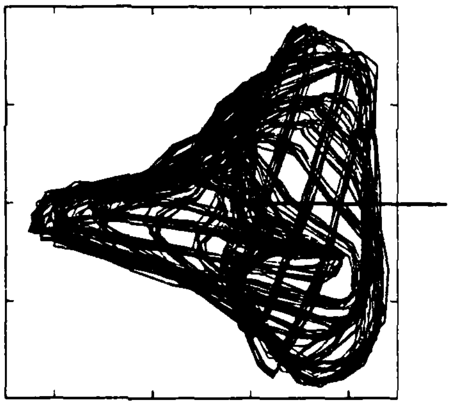

(e) R/R_c = 13, aspect ratio = 22.3

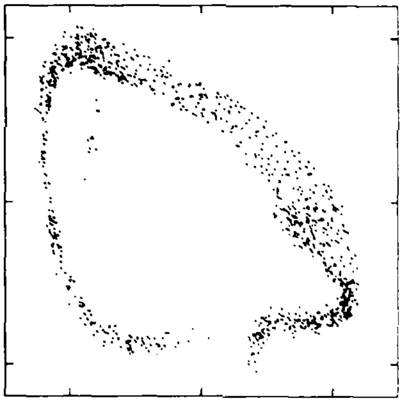

(f) R/R_c = 13, aspect ratio = 22.3

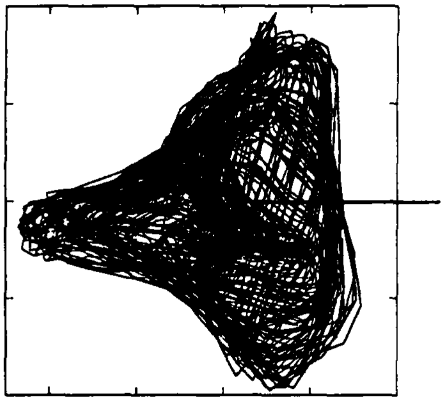
(g) R/R_c = 14, aspect ratio = 22.3

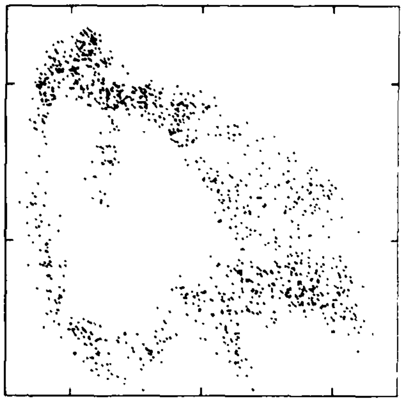
(h) R/R_c = 14, aspect ratio = 22.3

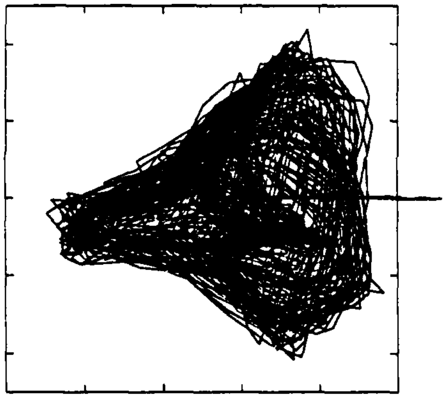
(i) R/R_c = 15, aspect ratio = 22.3

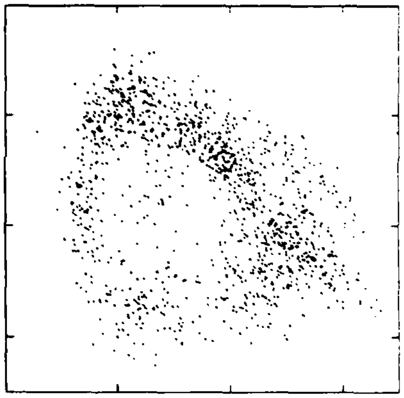
(j) R/R_c = 15, aspect ratio = 22.3

section for an aspect ratio of 22.33 and Reynolds numbers of R/R_c = 11, 12, 13, 14, 15. From these it will be noticed that between R/R_c = 12 and 13 the torus begins to get slightly fuzzy. At R/R_c = 14 the attractor becomes more ill defined and the Poincaré section thicker. As the Reynolds number increases to R/R_c= 15 the attractor gets very fuzzy and the Poincaré section becomes very thick. It certainly only vaguely resembles the former torus. This is the qualitative behavior of a torus as the system becomes weakly turbulent (Brandstater, 1987). It is unfortunate that the resolution of the system was not sufficient to show the folding on the attractor for weakly turbulent flow.

A similar sequence of figures is shown for an aspect ratio of 34.48 in figure 5.9(a)-(j). The sequence looks very similar to that for the smaller aspect ratio, though the attractor is slightly rotated in phase space. The conclusion reached from this observation is that the reconstructed attractor does not have an aspect ratio dependence. This would suggest that the computed dimension will not have this dependence either. The investigation of this expectation is the subject of the next section.

5.2.4 Dimension Determination

In spite of the implications of the frequency spectra and the appearance of the time series, it still has not been shown that the system made a transition to chaotic flow. In order to prove that, it must be demonstrated that either the system had at least one positive Lyapunov exponent or that the attractor dimension increased monotonically as the Reynolds number increased and was fractal. Actually, showing the dimension was fractal is not necessary if the frequency spectrum was obtainable. If the dimension was small and the spectrum was broad (perhaps with peaks) then it was chaotic. If it were noisy, then the dimension would have appeared to have been that of the embedding dimension. The only other choice would have been quasi-periodic flow but that would have been ruled out by examining the spectrum.

A plot of the attractor dimension calculated by the Grassberger-Procaccia algorithm for aspect ratio 19.90 and Reynolds numbers R/R_c = 11, 12, 13, 14 and 15 appears in figure 5.10. Clearly the dimension was small. The spectra, as mentioned above, showed peaks due to the fact the flow was on a torus, but the background noise implied that it was wrinkled (fractal). Thus the flow was chaotic.

Figures 5.9(a)-(j). Attractors and Poincaré sections for an aspect ratio of 34.48. These figures show the reconstructed attractors and an associated Poincaré section as a function of Reynolds' number. Figures 5.9(a) and (b) are for $R/R_c = 11$. Figures 5.9(c) and (d) are for $R/R_c = 12$. Figures 5.9(e) and (f) are for $R/R_c = 13$. Figures 5.9(g) and (h) are for $R/R_c = 14$. Figures 5.9(i) and (j) are for $R/R_c = 15$. The radius ratio was 0.862. The attractors were constructed in three dimension, of which these pictures represent a two dimensional projection. The designated lines on the attractors show where the Poincaré section were taken.

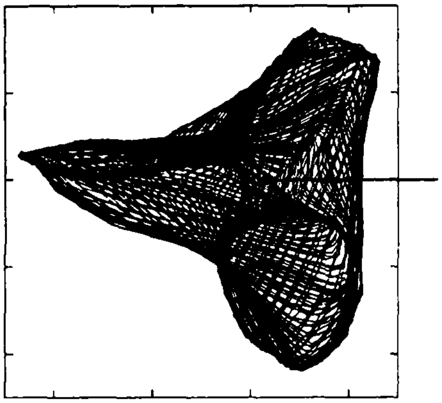

(a) $R/R_c = 11$, aspect ratio = 34.48

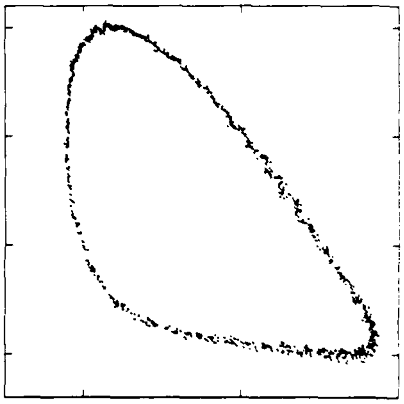

(b) $R/R_c = 11$, aspect ratio = 34.48

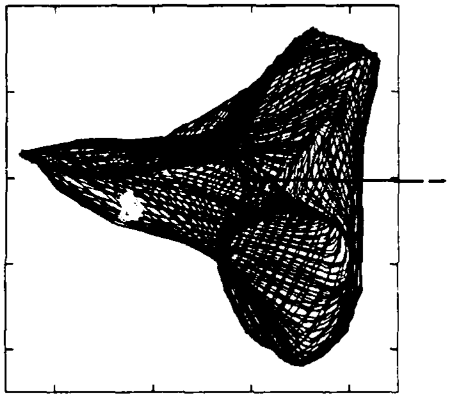

(c) $R/R_c = 12$, aspect ratio = 34.48

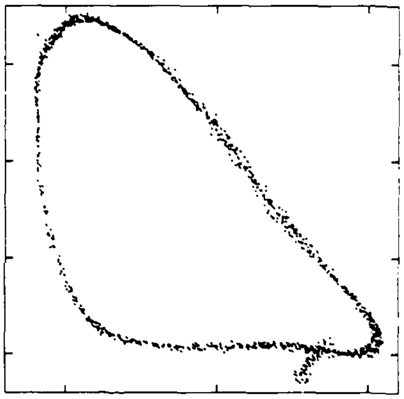

(d) $R/R_c = 12$, aspect ratio = 34.48

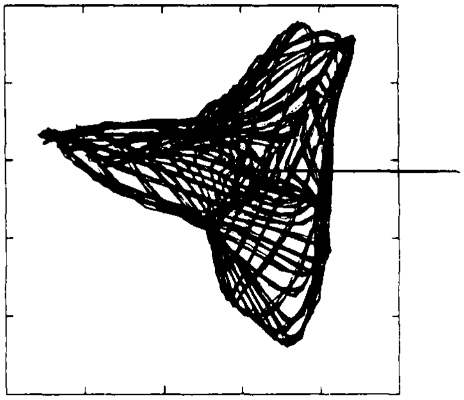

(e) $R/R_c = 13$, aspect ratio = 34.48

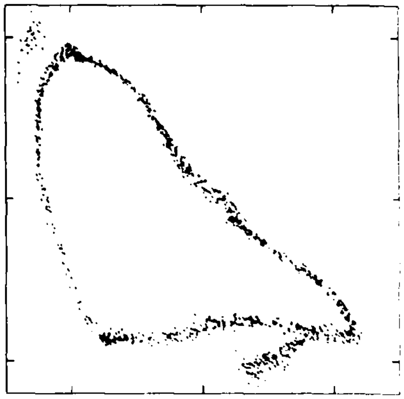

(f) $R/R_c = 13$, aspect ratio = 34.48

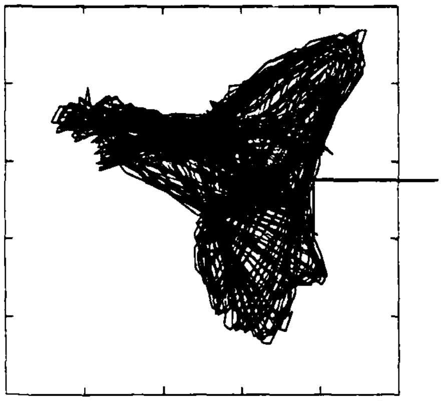

(g) R/R_c = 14, aspect ratio = 34.48

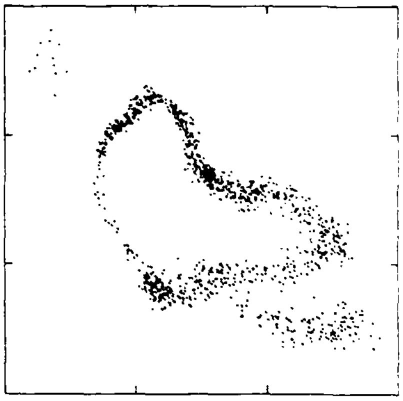

(h) R/R_c = 14, aspect ratio = 34.48

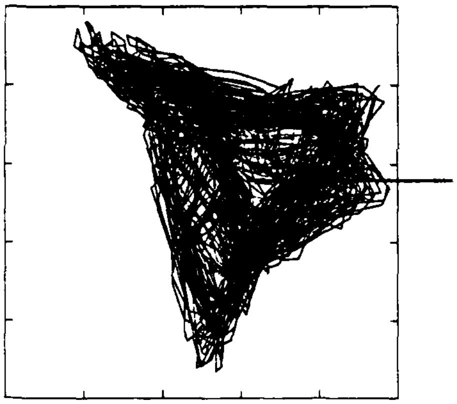

(i) R/R_c = 15, aspect ratio = 34.48

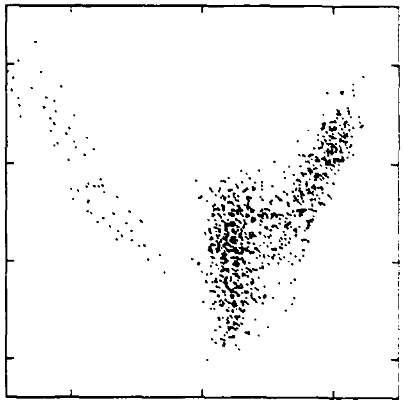

(j) R/R_c = 15, aspect ratio = 34.48

Figure 5.10 Grassberger-Procaccia dimension verses Reynolds number. The hollow squares are my data and the filled diamonds are from Dr. Brandstater's dissertation (Brandstater, 1984). For my data the aspect ratio was 19.90 and the radius ratio 0.862. For Dr. Brandstater's data the aspect ratio was 20 and the radius ratio was .875.

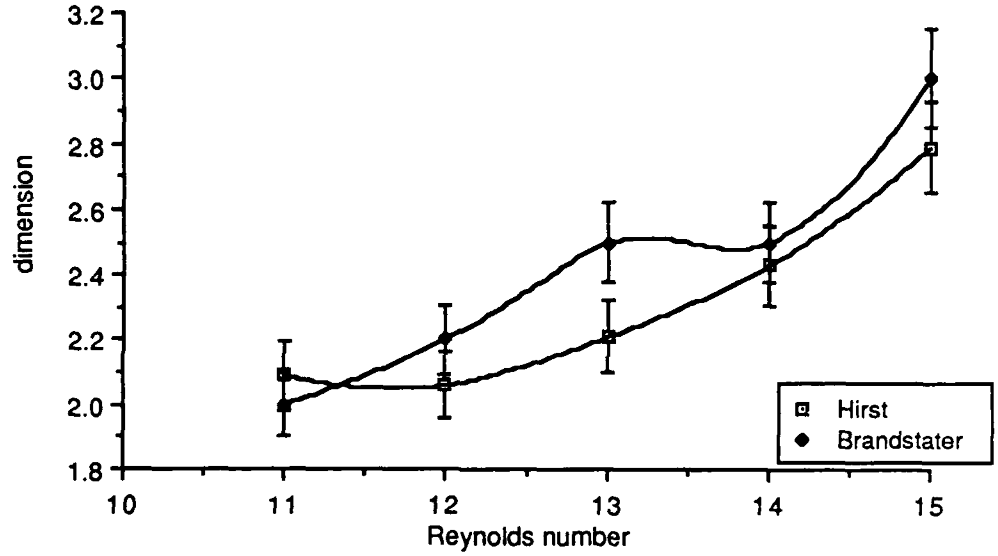

Figure 5.10 Attractor dimension vs aspect ratio

Plotted on the same graph are the results of Dr. Brandstater. It should be pointed out that the radius ratios of the two systems are different and this can make a difference in the observed flows. For Dr. Brandstater's experiment the radius ratio was a/b = .875 and for my experiment it was a/b = .862 for a percent difference of about 1.5%. Nevertheless, the trend in the curves is similar and have almost quantitative agreement. This confirmed Dr. Brandstater's observation of a transition to low-dimensional chaos.

The above results verified that the experimental technique used gave qualitatively similar results when compared with previous experiments. Once certain of that, the experimental part of the study of the aspect ratio dependence of the attractor dimension was begun. Since the Grassberger-Procaccia algorithm increasingly underestimates the attractor dimension as the dimension increases, the Badii-Politi dimension as well as the Grassberger-Procaccia correlation dimension was calculated (Kostelich, Swinney, 1987).

The results of the calculations of the Badii-Politi dimension for the aspect ratio study are shown in Figure 5.11. To within the error in the ability to determine the attractor dimension, the curves for each integer value of R/R_c were flat. So, there was no measurable aspect ratio dependence. The source of the fluctuations in the dimension with aspect ratio is not known. However, since the aspect ratio increases by 75% across the graph, it does not seem reasonable that the fluctuations would be due only to an increase in the system volume. The error bars represent the consistency of the algorithm to determine the attractor dimension from an attractor of known dimension using different samples. The consistency of the dimension calculated from the experimental data for this experiment tended to be better than this error (±5%). For a Reynolds number of $R/R_c = 11$, the mean fluctuation in the data was about 1% in 10 samples. For a Reynolds number of $R/R_c = 13$, the mean fluctuation was about 4% in 10 samples. A graph of the Grassberger-Procaccia dimension with aspect ratio is given in figure 5.12. It shows similar behavior as the Badii-Politi dimension.

A plot of the Reynolds number dependence of the attractor dimension calculated by the Badii-Politi algorithm is shown in Figure 5.13. The dimensions given in this figure are averaged over the aspect ratio values. Since the curves showed little dependence with aspect ratio, they were averaged for all aspect ratios

Figure 5.11 Badii-Politi dimension versus aspect ratio. The hollow squares with a center dot represent $R/R_C = 11$, the filled diamonds represent $R/R_C = 12$, the filled squares represent $R/R_C = 13$, the hollow diamonds represent $R/R_C = 14$, and the stars represent $R/R_C = 15$. The radius ratio is 0.862. Since the dimension determinations are no better than to within 10%, there is no evident trend with aspect ratio. This error represents the consistency with which the various algorithms may determine the dimension of attractors whose dimension is known independently of these algorithms. The consistency in the dimension determined from several independent experimental data sets is somewhat better than this.

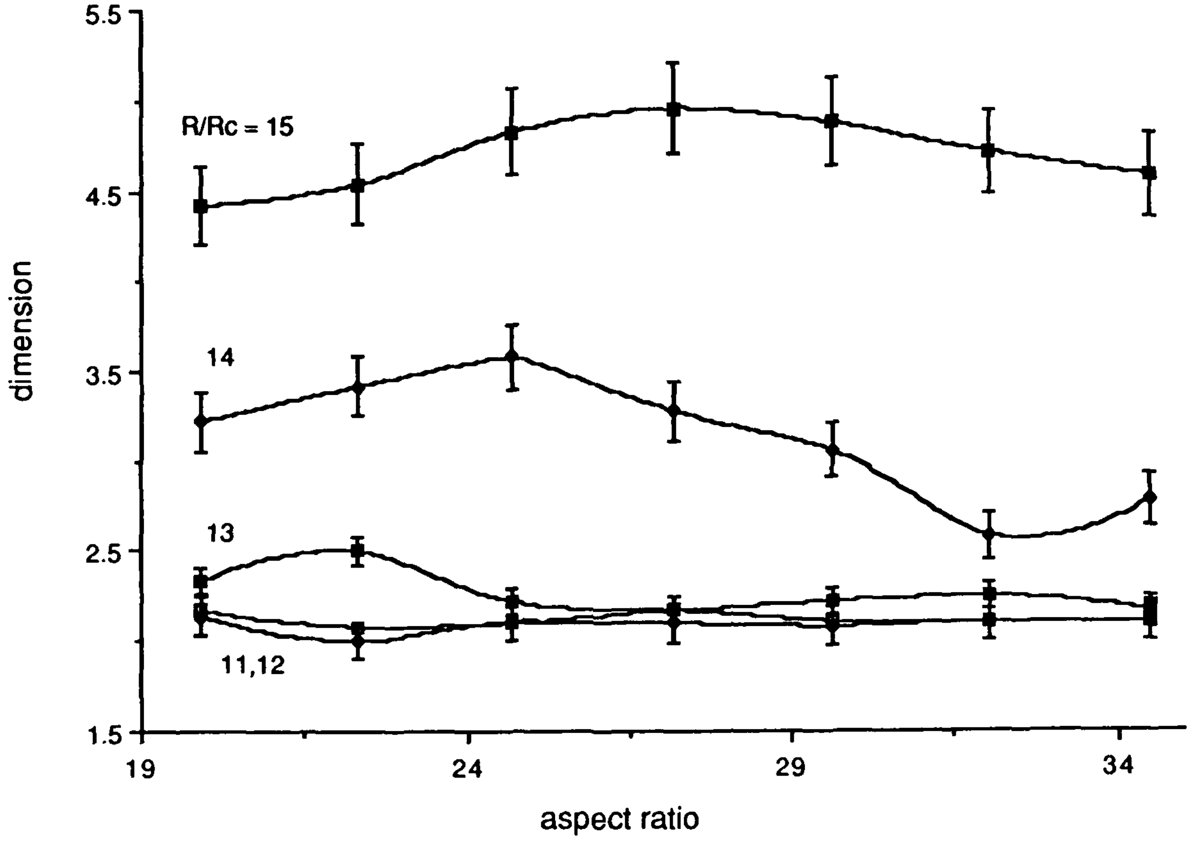

Figure 5.11 Badii-Politi dimension vs aspect ratio

Figure 5.12 Grassberger-Procaccia dimension verses aspect ratio. The hollow squares with a center dot represents $R/R_c = 11$, the filled diamond represents $R/R_c = 12$, the filled square represents $R/R_c = 13$, the hollow diamond represents $R/R_c = 14$, and the star represents $R/R_c = 15$. The radius ratio is 0.862. Since the dimension determinations are no better than to within 10%, there is no evident trend with aspect ratio. This error represents the consistency with which the various algorithms may determine the dimension of attractors whose dimension is known independently of these algorithms. The consistency in the dimension determined from several independent experimental data sets is somewhat better than this.

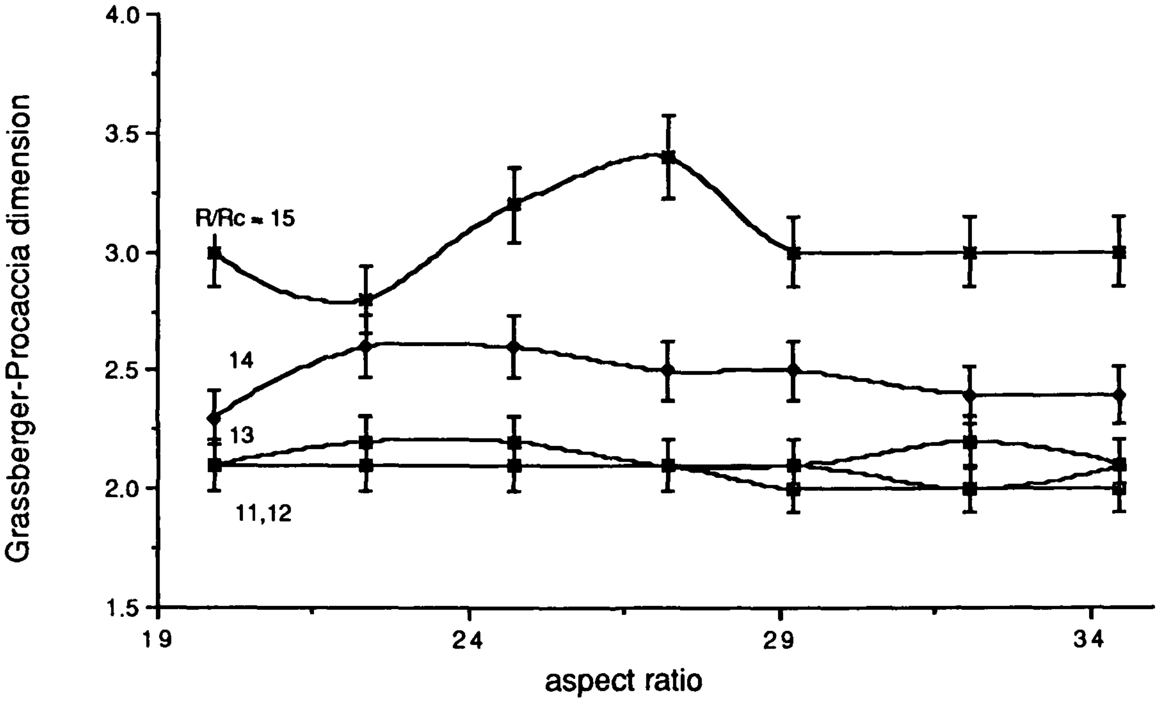

Figure 5.12 Grassberger-Procaccia dimension vs. aspect ratio

Figure 5.13 Badii-Politi dimension and Grassberger-Procaccia dimension verses Reynolds number. The filled diamonds are the Badii-Politi dimension and the hollow squares are the Grassberger-Procaccia dimension. Each point is an average over all the dimensions calculated for the range of aspect ratios at a given Reynolds number. The radius ratio is 0.862. The underestimate of the Grassberger-Procaccia algorithm is clearly shown at the higher Reynolds numbers.

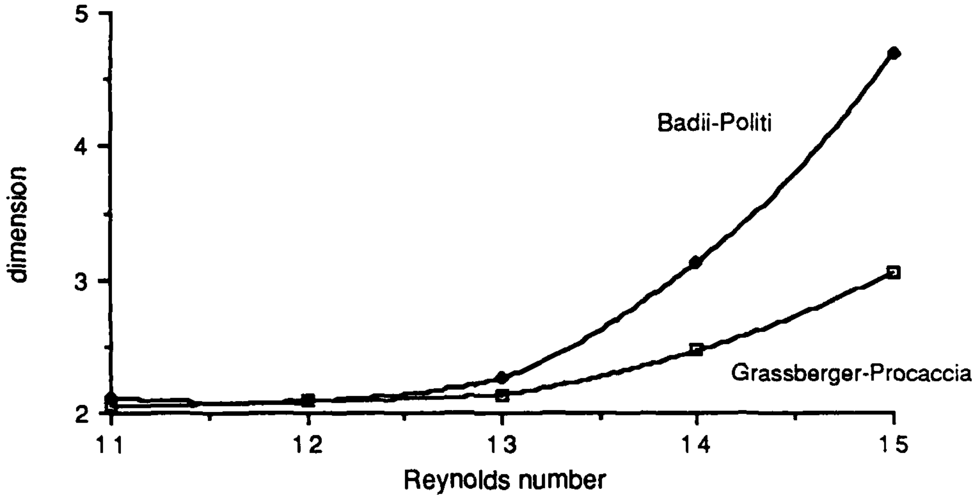

Figure 5.13 Dimension vs Reynolds number

and the averaged dimension plotted as a function of Reynolds number. Also on this figure are plotted the results of the Grassberger-Procaccia algorithm. It is obvious that the Badii-Politi dimension increased much more quickly with Reynolds number than the Grassberger-Procaccia dimension. A study of the behavior of both the Grassberger-Procaccia and the Badii-Politi computation with dimension for various systems has been done by Kostelich and Swinney (1987). The results of this study imply that the Badii-Politi algorithm gives the better estimate of attractor dimension for embedding dimensions greater than 2. Thus, though the Grassberger-Procaccia estimate I obtained verified that my results are similar to Brandstater (Brandstater, et. al., 1983(a)) the Badii-Politi estimate was used for a better value of the attractor dimension.

The contribution of experimental scatter in the data to the error in the time series was easy to determine from elementary statistics. For Taylor vortex flow the standard deviation for 20,000 points averaged over 3 minutes for a range of Reynolds numbers ($139.1 \leq R \leq 154.0$) was .005 cm/sec. The radial component of the velocity at those Reynolds number was about 0.322 cm/sec. Thus the error was about 3%. As was shown in chapter 3, the error grows proportionally with Reynolds number if it is primarily due to phase noise (ambiguity bandwidth). So the error at the higher Reynolds numbers should also be about 3%. Another way of looking at this is to say the signal-to-noise ratio was about 5 bits. From this it probably would be assumed that a fairly accurate estimate of the dimension was possible. Such was not the case.

An estimate of the error in the dimension calculation could not be obtained from the velocity error in the data. There is presently no technique which permits such a calculation. The error estimate quoted here was based on comparing dimensions calculated analytically with dimensions calculated by the Grassberger-Procaccia or Badii-Politi algorithms for the Lorenz, Henon-Heiles or the Mackey-Glass attractors (Kostelich, Swinney, 1987). This error in the dimension determination for a given algorithm (Badii-Politi or Grassberger-Procaccia)was estimated to be about ± 5 percent. The two different algorithms do not agree within this error. As pointed out above, the Badii-Politi algorithm appears to be the more accurate. This still is not a very satisfying way to do this. A quantitative measure of the error calculated in the process of determining the attractor dimension needs to be developed.

5.2.5 Lyapunov Exponents

The largest positive Lyapunov exponent for the flow was calculated from the time series by the Wolf method as outlined in chapter 2. These graphs of the Lyapunov exponents should be understood qualitatively only. The signal to noise for my data was about 5 bits. To be reliable quantitatively the Lyapunov exponents should be calculated from data with a signal to noise of at least from 6 to 8 bits (Wolf et al., 1985). Nevertheless, the results of the calculations will exhibit the qualitative behavior for the appropriate criteria for choosing a value for the exponent. The results are presented in figure 5.14 as a function of Reynolds number at an aspect ratio of 22.3 (squares). The Lyapunov exponent is definitely positive when $R/R_c = 13$ which indicates that the flow has become chaotic. The indicated exponent continues to increase with Reynolds number. In figure 5.14 the Lyapunov exponents for an aspect ratio of 34.5 are also plotted (diamonds). The same criteria were used to choose the exponents for both sets of data and the parameters for the calculations were the same. In spite of the fact the absolute values of the exponents may not be reliable, quantitative differences in the exponents should reflect a difference in behavior for the two data sets. There is no significant difference between the Lyapunov exponents for the two aspect ratios. This supports the results of the dimension calculation.

5.3 Summary of Results

The goal of this experiment was to investigate the aspect ratio dependence of the attractor dimension in Taylor-Couette flow. In this process other observations were made of various quantities as a function of aspect ratio. The wavespeeds monotonically increased with aspect ratio and approached an asymptote. The ratio of the wavespeeds, s_2/s_1, also increased monotonically and seemed to have approached a limit asymptotically. The frequency spectra showed an increase in the population of the higher harmonics with aspect ratio for a given Reynolds number for the lowest three aspect ratios. For aspect ratios larger than 24.8 the number of harmonics remained constant. It would appear the increase is only due to the finite length of the flow becoming less important as the aspect ratio increases. Thus it

Figure 5.14 The largest Lyapunov exponent verses Reynolds number for an aspect ratio of 22.3 (squares) and an aspect ratio of 34.5 (diamonds). The Lyapunov exponent increases monotonically with Reynolds number in both cases. The Lyapunov exponents become definitely positive at $R/R_c = 13$, indicating a transition to chaotic flow in agreement with the dimension and power spectra evidence. There is no indication of an aspect ratio dependence. The discrepancy at $R/R_c = 13$ is the largest that was observed. Most of the other computed values for $R/R_c = 13$ for various aspect ratios were centered around an exponent of 0.4. The Wolf algorithm was used to calculate these results. The data signal-to-noise ratio was slightly too high according to Wolf's criterion for the values of the exponents to be quantitatively accurate however the qualitative behavior should be accurate.

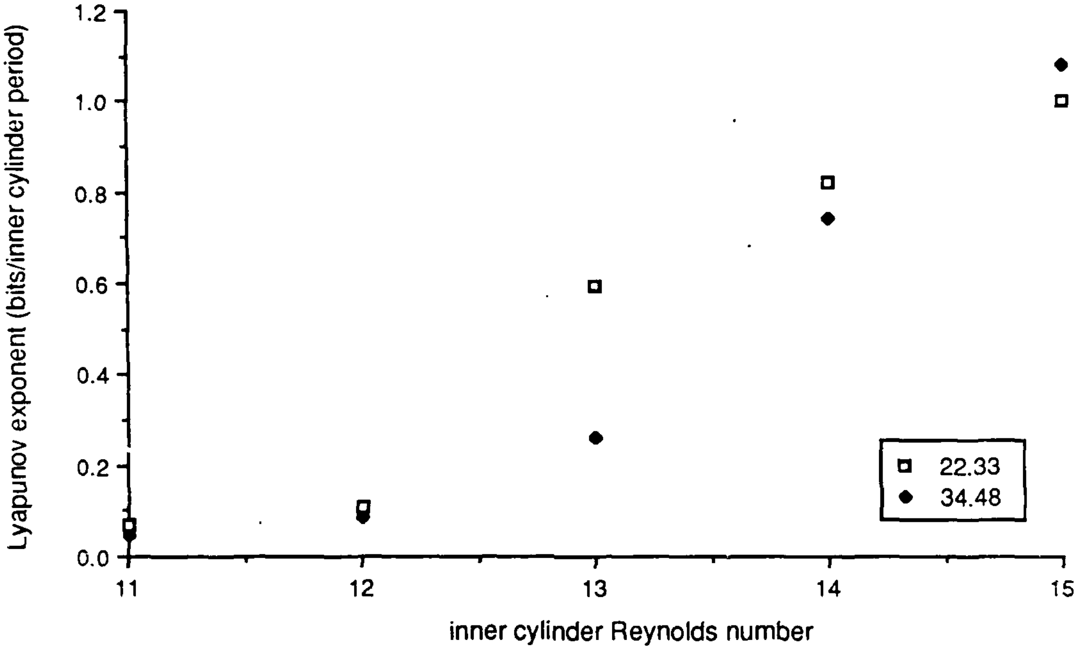

Figure 5.14 Largest Lyapunov exponent vs. Reynolds number

would appear that the flow would become independent of the aspect ratio if the aspect ratio were large enough ($\Gamma \geq 25$). The largest Lyapunov exponent was the same within the computational error for the smallest and largest aspect ratio. Finally, within the parameters of this experiment the dimension of the attractor determined from the time series did not appear to have an aspect ratio dependence.

Chapter 6 - Conclusions

The efforts of this research were directed to understanding the transition to turbulence in fluids and the application of various techniques in nonlinear dynamics to this understanding. To this end two investigations were performed. The first was a study of the primary bifurcations for counter-rotating cylinders. The results of this study were in accord with predictions of linear stability theory for the wavespeed, axial wavelength and bifurcation boundaries. As is well known, the flow that develops beyond the bifurcation from Couette flow cannot be predicted from linear stability theory. It would be interesting to continue these investigations away from bifurcation boundaries for non-linear flow behavior.

The second part of the study and the main goal of the research was the investigation of the dependence of the attractor dimension on the aspect ratio. The attractor dimension represents in some sense the number of degrees of freedom in the flow. Since the flow involves strong nonlinear interactions it is necessarily complex, but for a small driving force only a small number of degrees of freedom are excited. If the dimensions are global in the flow, does increasing the volume add degrees of freedom? As shown in chapter 5, this does not happen. The same attractor dimension occurs for an aspect ratio of 34 as for 20. It would be reasonable to ask if this continues for even larger aspect ratios. The answer to this in not known. However, since the other measured values such as wavespeed seemed to be approaching asymptotic values, it should probably be expected that if the aspect ratio were increased beyond 34 that the dimension would remain the same.

Several extensions to this research come to mind. The first would be to explore the aspect ratio dependence for different radius ratios. This would examine the importance of the influence of the confining cylinder walls in enforcing order on the system and keeping the dimension low. A second study would be of the correlation between the various vortices in the flow. If the flow were well correlated throughout, then the attractor dimension determined from a single point in the flow would be representative of the of the entire flow. If the flow were not correlated between vortices then that would imply that a single point measurement would yield a partial dimension. Therefore the dimension of the flow would be the sum of the partial dimensions.

The ultimate importance of the results of this experiment is how they advance the understanding of turbulent flow. The applications of nonlinear dynamics to this problem have shown how the complexity of turbulent flow arises, not as an artifact of noise, but as a natural part of the dynamics of the flow. Low dimensional systems may be modelled using the present techniques of determining dimension and bifurcations. Highly symmetric systems like the Taylor-Couette system permit application of such techniques to experimental flows. Hopefully, these studies will reveal extensions of these methods or new techniques which will be suitable for studying and understanding the entire range of turbulent flow.

Appendix A. Experimental Parameters

HIRST SYSTEM

1. Couette hardware data

Plexiglass outer cylinder:

length = 40.32 cm

inside radius (b) = 7.704 ± 0.007 cm

minus 1" for nylon end and moveable upper boundary the maximum length for fluids is = 37.78 cm

Fluid volume = 1928 cm^3

Larger inner cylinder:

a = 6.640 ± 0.0013 cm

so with the above plexiglass cylinder

Γ = 35.6 max

a/b = .8623

$R_{critical} = 113.16$

gap = 1.064 cm

Chord length at measurement volume, perpendicular to the optical axis $(2*X_A)$ = 2.8 cm

Smaller inner cylinder:

a = 5.679 ± 0.0013 cm

so with the above plexiglass cylinder

Γ = 18.6 max

a/b = .7372

$R_{critical} = 84.16$

2. Fluid data

Cargille immersion liquid code 0195,"Orange juice"

(appears to be mostly d-limonene with some other added components)

n_D = 1.4942 @ 25^{0}C and 5893 Angstroms
Viscosity at 25.60^{0}C ≈ 1.414 cS (measured 29 Dec 86)

3. LDV Optics Data

Conversion from Doppler Frequency to Velocity in orange juice:

$\Delta f_0/v = 5.872\ \mathrm{cm}^{-1}$

with v in cm/sec and f in kilohertz.

The fringe spacing is the inverse of this: 1.703µm

For the transmitting lens (TSI type 917A):

medium	focal length	half-angle for beams with 5 cm sep. (κ)
air	12.13 cm	10.71 deg
orange juice	18.31 cm	7.141 deg

For the receiving lens (TSI type 917A):

medium	focal length	half-angle for beams with 5 cm sep. (°)
air	12.06 cm	10.80 deg
orange juice	18.21 cm	7.200 deg

The number of fringes is:

$N_{NF} = 1.27d/D = 1.27 * 50$ mm/2mm = 31.75 fringes

where D is the waist of laser beam due to the laser cavity geometry (usually given in the manual accompanying the laser) and d = beam separation.

The diameter of the probe volume is:

$$d = 31.75 \text{ fringes} * 1.703\ \mu m/\text{fringe} = 54\ \mu m$$

The length of the probe volume is, from simple geometry:

$$l = d * \cot \kappa = 431\ \mu m$$

The probe volume is an ellipse of revolution thus:

$$V = 4\pi(d/2)^2(l/2)/3 = \pi d^2 l/6 = 6.58 \times 10^{-7}\ \text{cm}^3.$$

Photomultiplier tube

Type: EMI 9863B/100,

Cathode: S-20

Maximum quantum efficiency: 20%

Quantum efficiency at 6328 Angstroms: 7%

Laser

Spectra-Physics Model 125A Helium-Neon

Wavelength: 6328 Angstroms

Beam waist @ $1/e^2$ intensity points = 2.0 mm

Beam divergence: 0.7 milliradians

Nominal power: 50 milliwatts

4. Scattering particle data:

Titanium Dioxide:

diameter $\approx 0.22\mu$

index of refraction $= n_D = 2.7$

density $= \rho = 4.0$ gm/cm^3

volume/particle $= 5.57 \times 10^{-15}$ cm^3

$Q = 3.4 \times 10^{-8}$ grams/cm^3

The number of grams/cm^3 of seeding particles needed to produce n particles/probe volume is given by:

No. of grams/ cm^3 $= n * \rho *$ volume of particle /probe volume

$$\equiv n * Q$$

where Q is the number of grams/cc for one particle/probe vol.

The probability of <u>no</u> particles being in the probe volume is:

$$\exp(-n)$$

so the probability of no particles being in the probe volume as a function of n is:

<u>No. of particles/probe vol.</u>	<u>Prob. of no particles being seen</u>
10	4.5×10^{-5}
5	6.7×10^{-3}
2	.135
1	.37

5. Tracker Calibration

Frequency (khz) = -2.752 + 27.024*Volts

Frequency limits on tracker performance:

5.53 Khz - 234 Khz (0.293 volts - 8.75 volts)

The Bragg cells were 50 khz apart so the velocity zero was at 50 khz or 1.901 volts.

GORMAN SYSTEM

1. Couette hardware data

Glass outer cylinder:

length = 36.1 cm

inside radius (b) =5.945 ± 0.002 cm

minus 1" for teflon ends and moveable upper boundary the maximum length for fluids is = 34.1 cm

Inner cylinder:

a = 4.759 ± 0.001 cm

so with the above glass cylinder

$\Gamma = 28.7$ max

$a/b = 0.8005$

$R_{critical} = 94.74$

gap = 1.186 cm

2. Fluid data

60 % Glycerine- 39 % water mixture (by volume)
with 1% Kalliroscope flakes added (mostly water)

Viscosity at 25^0C ≈ 10.48cS (measured 28 March 1986)

Appendix B. Software

IBM-PC Programs

ASPECT.C -program-changes aspect ratio

ATOD.C -subroutine-analog to digital driver

CONV.FOR - subroutine-converts binary to BCD

DAQED.FOR - subroutine-data collection header editor

DAQINI.FOR -subroutine-data collection header initializer

DAQREP.FOR - subroutine-data collection header updater

DATVAL.C -program-analog to digital measurement; averages measurements to produce one value

EDNAME.FOR - subroutine-edits namefile

FINTIM.FOR - subroutine-gets time from data file headers

FIT.FOR - program-fits data from LDV measurements and determines axial wavelength

GETTIM.FOR - subroutine-gets most recent time

GOMOT.FOR - subroutine-Compumotor driver

GTNAME.FOR - subroutine-updates data set name to latest version

HIRST.FOR - program-Compumotor driver executive program

HSTEST.C - program-C program to test high speed a-to-d acquistion

INITAL.C - subroutine-initializes registers in Burr-Brown PCI boards

IOTEST.C - program-test the reading and writing of Burr-Brown digital I-O

LATOD.C - subroutine-a-to-d driver for Burr-Brown a-to-d board

LOOK.FOR - program-allows examination of data files

OPTICAL.C - program-controls vertical position of LDV optics

PPLOT.FOR - subroutine-allows ploting of data in data files on PC

REPLY.FOR - subroutine-converts a binary header string to the appropriate data type

REYNOL.FOR - subroutine-calculates Reynolds number from velocity data

STAINI.FOR - subroutine-initialized status file header of data file

STAREP.FOR - subroutine-status file header updater
STATED.FOR -subroutine-status file header editor
SYNDATA.FOR - program-synthetic data file generator for debugging
TATOD.C - subroutine-a-to-d time series data collection subroutine
TEMP.FOR - program-returned temperature from thermistor in bath
THERM.FOR - subroutine-returned temperature from thermistor in bath
TIME.C - subroutine- determined time from system clock
TIMSER.FOR - program-time series data collection executive program
VISCO.FOR - subroutine -determined viscosity from temperature data
WAIT.C - subroutine-digital software delay program
WRTBIT.C - subroutine-writes a bit to Burr-Brown digital IO
WRTBYT.C - subroutine-writes a byte to Burr-Brown digital IO
_MOTORC.ASM - subroutine-Slo-Syn stepper motor driver

Ridge Programs

Ridge Shell Files:

DOCONVIF - Integer to floating point conversion shell file
DOCORRDIM - Correlation dimension shell file
DOFFT - Fast Fourier transform shell file
DOLOOP - Mutual information shell file
DOPHASE - Phase portrait shell file
DOPONSEC - Poincare section shell file
DOSERIES - Time series shell file
FETISH-Lyapunov exponent shell file

Appendix C. Primary instability data

Parameters:

a= 4.759 cm b=5.945 cm d=1.186 cm h=34.1 cm

$\Gamma = 28.7$

States obtained by incrementing inner cylinder speed unless other wise noted

(i.e., a comment followed by Ro means the outer cylinder was incremented)

Date	Temp.°C	Outer Freq. (hz)	Inner Freq.(hz)	Comments
5 OCT 85	Fluid composition: 60% Glycerine, 40% water then 2% kaliroscope			
	24.8	-0.000	.282	COUETTE-TVF
	25.0	-.150	.324	C-TVF
	25.0	-.200	.360	C-TVF
8 OCT 85	?	-.25	.391	C-SPIRALS
	?	-.225	.375	C-TVF
	25.6	-.24	.385	C-SPIRALS
11 OCT 85	25.0	-.24	.398	C-SPIRALS
	?	-.2325	.380	C-SPIRALS
	?	-.235	.382	C-SPIRALS
	?	-.2377	.385	C-SPIRALS
	?	-.2362	.3830	C-SPIRALS
	?	-.237	.383	C-SPIRALS
	?	-.3998	.4671	C-SPIRALS
14 OCT 85	25.0	-.300	.4216	C-SPIRALS
	?	-.2603	.3975	C-SPIRALS
	26.0	-.2701	.4034	C-SPIRALS
	?	-.255	.3923	C-SPIRALS
	25.5	-.2648	.3997	C-SPIRALS
	24.9	-.270	.406	C-SPIRALS
21 OCT 85	25.0	-.2603	.3982	C-SPIRALS
22 OCT 85	25.2	-.2453	.3876	C-SPIRALS
	25.2	-.2625	.3979	C-SPIRALS
23 OCT 85	26	-.2400	.3802	C-SPIRALS
24 OCT 85	24.8	-.310	.4303	C-SPIRALS
	24.8	-.3188	.4320	C-SPIRALS
	24.1	-.312	.4308	C-SPIRALS
	24.6	-.310	.4292	C-SPIRALS
	24.7	-.3089	.4283	C-SPIRALS

24.9	-.3083	.4284	C-SPIRALS		
	24.8	-.3090	.4284	C-SPIRALS	

4 NOV 85 <u>HEAT BATH INSTALLED</u>
(the temperature will be noted only at the top of columns or it if changed)

4 NOV 85	25.87	-0.000	.2655	C-TAYLOR

8 NOV 85 <u>NEW SOLUTION- 0.7 % KALLIROSCOPE</u>
60 % Glycerine, 40 % water

9 NOV 85	25.00	-0.000	.2168	C-TVF	
11 NOV 85		-0.000	.2168	C-TVF	
		-.1875	.3008	C-SPIRALS	
		-.1838	.2993	C-TVF	
		-.18525	.3000	C-TVF	
		-.1860	.3000	C-TVF	<u>TRANSITION</u>
		-.18675	.30075	C-SPIRAL	<u>TRANSITION</u>
		-.2283	.32625	C-M=1 (?)	SPIRALS
		-.23025	.32775	C-M=1 (?)	IDENTIFIED
		-.2310	.3285	C-M=1 (?)	BY EYE
		-.23175	.32925	C-M=1 (?)	M=?
		-.2315	.330	C-M=1 (?)	DOUBTFUL
	24.96	-.23625	.3315	C-M=1 (?)	
12 NOV 85	25.00	-.2400	.333	C-M=1 (?)	
		-.23775	.33225	C-M=1 (?)	
		-.2370	.3315	C-M=1 (?)	
		-.24375	.3345	C-M=1 (?)	
		-.2475	.33675	C-M=1 (?)	
		-.3375	.37875	C-M=1 (?)	
	25.01	-.4125	.4140	C-MIXED (M=1,2)(?)	
	25.00	-.225	.32475	C-SPIRALS	
		-.240	.333	C-SPIRALS	
		-.200	.3105	C-SPIRALS	
		-.2325	.330	C-SPIRALS	

13 NOV 85 The m value for the spirals now identified by laser

24.99	-.5325	.46725	C-M=3 SPIRALS
	-.450	.4320	C-M=2
25.00	-.36975	.39375	C-M=2
	-.330	.3765	C-M=2
	-.300	.3615	C-M=2

		-.270	.348	C-M=2	
		-.24975	.339	C-M=2	
14 NOV 85		-.2295	.339	C-M=1	
		-.23925	.333	C-M=2	
		-.2340	.3300	C-M=1	
		-.23775	.33225	C-M=2	
		-.23625	.33150	C-M=1	<u>TRANSITION</u>
		-.2370	.3315	C-M=2	<u>TRANSITION</u>
		-.4875	.44925	C-M=2	
		-.570	.4815	C-M=3	
		-.50025	.4545	C-M=2	
		-.510	.45825	C-M=3	
15 NOV 85		-.50475	.45675	C-M=2	
		-.5070	.45750	C-M=2	
		-.5085	.4575	C-M=2	
		-.50925	.45825	C-M=2	
		-.510	.459	C-M=2	
		-.51075	.45975	C-M=2	
		-.5115	.45975	C-M=2	
		-.51375	.4605	C-M=2	
		-.51975	.46275	C-M=3	
	25.01	-.51675	.46125	C-M=3	
16 NOV 85	25.00	-.51525	.46125	C-M=2	
		-.5160	.46125	C-M=2	
		-.51675	.46125	C-M=2	
		-.51825	.4620	**C-OSCILLATES M=2,3**	
		-.53325	.468	C-M=3	
		-.525	.465	C-M=3	
		-.51975	.46275	**C-OSCILLATES M=2,3**	
		-.5325	.46725	C-M=3	
18 NOV 85		-0.000	.21750	C-TVF	
		-.1845	.300	C-TVF	
		-.1875	.30225	C-M=1	
		-.19125	.3045	C-M=1	
20 NOV 85		-.19275	.30525	C-M=1	
21 NOV 85		-.19275	.30525	C-M=1	
22 NOV 85		-.2370	.3330	C-M=1	
		-.2385	.33375	C-M=2	
29 NOV 85		-.18675	.30225	C-M=1	
30 NOV 85		-.18675	.3015	C-M=1	
		-.18525	.30075	C-M=1	

12 DEC 85 Changed fluid: 60 % glycerine, 39 % water, 1 % kalliroscope

30 DEC 85	25.00	-0.000	.28125	C-TVF
31 DEC 85	25.01	-.2445	.3930	C-M=1

		-.2400	.3900	C-TVF
		-.2438	.3923	C-TVF
		-.2445	.3930	C-M=1
3 JAN 86	25.00	-.2445	.3945	C-TVF

The Reynolds' number was recorded from here on. The frequencies were "recomputed" from: $f_0 = R_0 * .00237609$, $f_1 = R_1 * .00296824$ which incorporate the valueof the critical Reynolds' number used to determine the viscosity (hence Reynolds' number) used in computing the values recorded in the notebook.

Until mentioned otherwise the transitions listed below are at the secondary bifurcation near the first codimension 2 point and so "S" means M=1 spirals.

6 JAN 86	25.00	-.2369	.39596	S-TVF Ro
		-.24806	.39596	TVF-S Ro
		-.25115	.39596	S-C R,
7 JAN 86		-.23476	.39299	S-TVF Ro
8 JAN 86		-.24367	.39299	TVF-S Ro
		-.23547	.39436	S-TVF Ro
		-.24593	.39436	TVF-S Ro
		-.23918	.39745	S-TVF Ro
		-.24901	.39745	TVF-S Ro
		-.25353	.39745	S-C Ro
		-.25258	.39745	C-S Ro
9 JAN 86		-.24141	.39893	S-TVF Ro
		-.25044	.39893	TVF-S Ro
10 JAN 86		-.24291	.40042	S-TVF Ro
		-.25187	.40042	TVF-S Ro
11JAN 86		-.25709	.40042	S-C Ro
		-.25709	.40042	C-S Ro
		-.24450	.40190	S-TVF Ro
		-.24450	.39360	TVF-S
13 JAN 86		-.24450	.40190	S-TVF
14 JAN 86		-.25353	.40190	TVF-S Ro
		-.24664	.40338	S-TVF Ro
15 JAN 86		-.25567	.40338	TVF-S Ro
		-.23238	.39300	S-TVF Ro
		-.24355	.39300	TVF-S Ro
17 JAN 86		-.24450	.39300	C-S
19 JAN 86		-.24141	.39300	S-TVF
20 JAN 86	25.02	-.25115	.39745	C-S Ro
21 JAN 86	25.00	-.26089	.40338	C-S Ro
		-.26089	.40338	C-S
		-.25709	.40101	C-S
		-.25709	.41437	C-TVF
		-.25187	.39804	C-S

	25.05	-.25187	.41080	S-TVF
22 JAN 86	25.00	-.25187	.40042	TVF-S
		-.24830	.40635	S-TVF
		-.24830	.39656	TVF-S
		-.24355	.40249	TVF-S
24 JAN 86		-.23024	.39151	S-TVF Ro
25 JAN 86		-.24664	.39448	C-S
		-.24664	.40398	S-TVF
		-.24664	.39507	TVF-S
27 JAN 86		-.24121	.39240	C-S
		-0.000	.28350	C-TVF

8 FEB 86 new mixture: 60 % glycerine, 39 % water, 1 % kalliroscope
Recompute frequency from recorded Reynolds' numbers using:

$$f_0 = R_0 * .0023182$$

$$f_1 = R_1 * .0028959$$

11 MAR 86	25.00	-0.000	.2745	C-TVF
		-.23854	.38313	C-S
12 MAR 86		-.23854	.38313	C-S
17 MAR 86		-0.000	.2745	C-TVF
		-.23785	.38255	C-S
20 MAR 86		-0.000	.275	C-TVF
		-.23625	.38111	C-S
		-.23553	.38024	C-S
		-.23484	.38024	C-S
		-.23391	.37937	C-S
		-.23321	.37937	C-TVF
21 MAR 86		-.28955	.41412	C-M=1
		-.29186	.41557	C-M=1
		-.29395	.41615	C-M=1
		-.29696	.41933	C-M=1
		-.29859	.41991	C-M=1
22 MAR 86		-.29998	.41991	C-M=1
		-.30067	.42078	C-M=1
		-.30137	.42136	C-M=1
		-.30230	.42136	C-M=2
		-.23182	.37879	C-TVF

28 MAR 86 changed aspect ratio $h = 33.425$ cm $\Gamma = 28.183$

5 APR 86		.23623	-.38169	C-M=1

Appendix D. Definition of Symbols

A variety of symbols are used throughout this dissertation. These quantites have definitions that may differ from other areas of physics or engineering and so are defined here in order to reduce the possibility of confusion.

a	inner cylinder radius.
b	outer cylinder radius.
d	size of gap between cylinders: $d = b-a$ also used for dimension.The usage is clear from context.
f_i	inner cylinder frequency - rotation speed of inner cylinder in cycles per second.
f_o	outer cylinder frequency - rotation speed of outer cylinder in cycles per second.
k	normalized wavenumber, $2\pi d/\lambda$. This is the integer number of wavelengths in a characteristic length.
L	axial length of fluid between the cylinders.
R_c	critical Reynolds number. The inner cylinder Reynolds number at which the flow makes the transition from Couette flow to Taylor vortex flow.
R_i	inner cylinder Reynolds number. This is defined as: $R_i = \frac{2\pi f_i a d}{\nu}$
R_o	outer cylinder Reynolds number. This is defined as: $R_o = \frac{2\pi f_o b d}{\nu}$
T_i	period of inner cylinder
Γ	aspect ratio, the ratio of the axial length of fluid to gap size: $\Gamma = L/d$

λ	axial wavelength In this dissertation this is the normalized axial wavelength which is the width of two vortices divided by the gap size. d; or, bifurcation parameter, usage clear from context
λ_i	Lyapunov exponent
ν	kinematic viscosity

Bibliography

Adrain, R. J.,"Laser Velocimetry" in **Fluid Mechanics Measurements** edited by R. J. Goldstein (Hemisphere Publishing Corporation, New York, 1983).

Aomar Ait Aider,"Séquences Transitoires en Écoulement de Couette Taylor: Influence du Rapport D'Aspect", Ph. D. Dissertation (Institut National Polytechnique de Lorraine, 1983).

A. Aitta, G. Ahlers and D. Cannell,"Tricritical phenomena in rotating Couette-Taylor flow", Phys Rev Letts **54** 673 (1985).

A. Arneodo, G. Grasseau and E. Kostelich,"Fractal Dimensions of f(α) Spectrum of the Henon Attractor", to be published.

R. Badii. and A. Politi,"Statistical Description of Chaotic Attractors: The Dimension Function", J Stat Phys **40**, 725 (1985).

H. Bai-Lin, **Chaos** (World Scientific Publishers, Singapore, 1984).

G. K. Batchelor,"An Introduction to Fluid Mechanics", (Cambridge University Press, New York, 1967) pg. 195.

T. Berland, T. Jossang and J. Feder," An experimental study of the connection between the hydrodynamic and phase-transition descriptions of the Couette-Taylor instability", (Institute of Physics Report Series, University of Oslo, Norway, Report 86-12, 1986).

M. Born and E. Wolf, **Principles of Optics**, 5th Edition (Pergamon Press, New York, 1974).

A. Brandstäter, J. Swift, H. Swinney and A. Wolf, "A Strange Attractor in a Couette-Taylor Experiment", in **Turbulence and Chaotic Phenomena in Fluids**, Proceedings of the IUTAM Symposium (Kyoto), edited by T. Tatsumi (North-Holland, Amsterdam, 1983).

A. Brandstäter, J. Swift, H. Swinney, A. Wolf, J. Farmer, E. Yen and J. Crutchfield, "Low Dimensional Chaos in a Hydrodynamic System", Phys Rev Letts **51**, 1442 (1983(a)).

A. Brandstäter, "Low Dimensional Chaos in a Hydrodynamic System", Ph. D. Dissertation (Christian-Albrechts-Universität, Kiel, 1984).

A. Brandstater and H.L. Swinney,"Strange attractors in weakly turbulent Couette-Taylor flow", Phys Rev A 35 2207 (1987).

P. Chossat and G. Iooss,"Primary and Secondary Bifurcations in the Couette-Taylor Problem", Jap. J Appl Math 2 37 (1985).

D. Coles,"Transition in circular Couette flow", J Fluid Mech **21**, 385 (1965).

I. Currie,"Fundamental Mechanics of Fluids", (McGraw-Hill, New York, 1974) pg. 229.

Y. DeMay and G. Iooss,"Calcul des solutions bifurquees pour le problème de Couette-Taylor avec les deux cylindres en rotation", J. Mec. theor. applique Numero special 1984, p. 193.

R. C. DiPrima and R. N. Grannick, "A Non-linear investigation of the stability of flow between counter-rotating cylinders" in **IUTAM-Symposium of Instability of Continuous Systems** ed. by H. Leipholz (Springer-Verlag, Berlin, 1971).

R. Donnelly, K. Park, R. Shaw and R. Walden, "Early Non-periodic Transitions in Couette Flow", Phys Rev Letts **44**, 987 (1980).

L. Drain, **The Laser Doppler Technique** (John Wiley and Sons, New York, 1980).

J-P. Eckmann and D. Ruelle,"Ergodic Theory of Chaos", Rev Mod Phys **57**, 617 (1985).

R. Engstrom, **Photomultiplier Handbook** (RCA, Solid State Division, Electro Optics and Devices, Lancaster, Pennsylvania, 1980).

J. Farmer, E. Ott and J. Yorke, "The Dimension of Chaotic Attractors", Physica 7D, **153** (1983).

A. Fraser," Information and Entropy of Strange Attractors", to be published.

A. Fraser and H. L. Swinney," Independent coordinates for strange attractors from mutual information", Phys Rev A **33**, 1134 (1986).

C. Foias, O. P. Manley, R. Temam and Y. M. Treve,"Number of modes governing two-dimensional viscous, incompressible flows", Phys Rev Letts **50**, 1031

(1983).

C. Foias, O. P. Manley and R. Temam,"Physical estimates of the number of degrees of freedom in free convection", Phys Fluids **29**, 3101 (1986).

M. Golubitsky and D. G. Schaeffer, **Singularities and Groups in Bifurcation Theory, Vol 1** (Springer-Verlag, Berlin, 1984).

M. Golubitsky and Ian Stewart, "Symmetry and Stability in Taylor-Couette Flow, preprint.

P. Grassberger and I. Procaccia, "Characterization of Strange Attractors", Phys Rev Letts **50**, 346 (1983).

H. Greenside, A. Wolf, J. Swift and T. Pignataro," Impracticality of a box-counting algorithm for calculating the dimensionality of strange attractors", Phys Rev A **25**, 3453 (1982).

J. Guckenheimer and P. Holmes,"Nonlinear Oscillations, Dynamical Systems and Bifurcations of Vector Fields" (Springer-Verlag,New York, 1983).

H. G. E. Hentschel and I. Procaccia," The infinite number of generalized dimensions of fractals and strange attractors", Physica **8D**, 435 (1983).

M. Hirsch and S. Smale, **Differential Equations, Dynamical Systems and Linear Algebra** (Academic Press, New York, 1974).

Hydrodynamic Instabilities and the Transition to Turbulence, edited by J. Gollub and H. Swinney (Springer-Verlag, New York, 1981).

IBM PC-DOS 3.10 Manual.

IBM PC-AT Technical Reference Manual.

J. D. Jackson, **Classical Electrodynamics**, 2nd Edition (John Wiley and Sons, New York, 1975).

G. King, Y. Li, W. Lee, H. Swinney and P. Marcus,"Wave speeds in wavy Taylor-vortex flow", J Fluid Mech **141**, 365 (1984).

E. Kostelich, and H. Swinney,"Practical Considerations in Estimating Dimension from Time Series Data", in **Chaos and Related Nonlinear Phenomena** edited by I. Procaccia and M. Shapiro (Plenum, New York, 1987).

E. Krueger, A. Gross and R. C. DiPrima, "On the relative importance of Taylor-vortex and non-axisymmetric modes in flow between rotating cylinders ", J Fluid Mech **24**, 521 (1966).

T. Kurz and G. Meyer-Kress,"Dimension density - an intensive measure of chaos in spatially extended turbulent systems", preprint.

L. D. Landau and E. M. Lifshitz, **Fluid Mechanics** (Pergamon Press, New York, 1959).

W. F. Langford, R. Tagg, E. Kostelich, H.L.Swinney and M. Golubitsky,"Primary Instabilites and Bicriticality in Flow between Counterrotating Cylinders", to be published.

B. B. Mandelbrot, **The Fractal Geometry of Nature** (W. H. Freeman, San Francisco, 1983).

P. Matisse and M. Gorman, "Neutrally bouyant anisotropic particles for flow visualization",Phys Fluids **27**, 759 (1984).

A. Papoulis, **Probability, Random Variables, and Stochastic Processes**, 2nd Edition (McGraw-Hill, New York, 1984).

PLL Tracker TRK 85 manual, Insititute of Applied Physics, D-2300, Kiel, West Germany.

Y. Pomeau, A. Pumir and Pelce, "Intrinsic Stochasticity with Many Degrees of freedom", J Stat Mech **37**, 39 (1984).

W. Press, B. Flannery, S. Teukolsky, and W. Vettering, **Numerical Recipes: The Art of Scientific Computing** (Cambridge University Press, New York, 1986).

D. Rand,"Dynamics and symmetry. Predictions for modulated waves in rotating fluids", Arch Rat Mech Anal **79**, 1 (1981).

L. Reichl,"A Modern Course in Statistical Mechanics", University of Texas Press Austin, Texas, 1980).

D. Ruelle, "Charateristic Exponents for a Viscous Fluid Subjected to Time Dependent Forces", Commun Math Phys **93**, 285 (1984).

D. Ruelle, "Large Volume Limit of the Distribution of Characteristic Exponents in Turbulence", Commun Math Phys **87**, 287 (1982).

O.Savas, "On flow visulaization using reflective flakes", J Fluid Mech **152**, 235 (1985).

H. G. Schuster, **Deterministic Chaos** (Physik-Verlag, Weinheim, West

Germany, 1984).

D. Sigeti and W. Horsthemke, "High-frequency power spectra for systems subject to noise", Phys Rev A **35** 2276 (1987).

H. Snyder, " Stability of Rotating Couette Flow. I. Asymetric Waveforms", Phys Fluids **11**, 728 (1968).

H. Snyder, "Stability of Rotating Couette Flow. II. Comparisons with Numerical Results.", Phys Fluids **11**, 1599 (1968(a)).

H. Snyder, "Waveforms in Rotating Couette Flow", Int. J. Non-Linear Mech **5**, 659 (1970).

H. Stanley,"Introduction to Phase Transitions and Critical Phenomena" (Oxford University Press, New York, 1971).

J. Swift and P. Hohenberg,"Hydrodynamic fluctuations at the convective instability",Phys Rev A **15**, 319 (1977).

Takens, F.,"Detecting strange attractors in turbulance" in **Lecture Notes in Mathematics 898** , edited by D. Rand and L. S. Young (Springer, Berlin, 1981).

G. I. Taylor, "Stability of a viscous liquid contained between two rotating cylinders", Phil Trans R Soc Lond **A223**, 289 (1923).

J. Theiler, "Spurious dimensions from correlation algorithms applied to limited time series data", Phys Rev A **34**, (1984).

J. M. T. Thompson, and H. B. Stewart, **Nonlinear Dynamics and Chaos** (John Wiley, New York, 1986).

D. J. Tritton, **Physical Fluid Dynamics** (Van Nostrand Reinhold, New York, 1977)

J. Vastano and E. Kostelich," Comparison of algorithms for determining Lyapunov exponents from experimental data", in **Entropies and Dimensions** edited by G. Meyer-Kress (Springer-Verlag, New York, 1986).

A. Wolf, J. Swift, H. L. Swinney and J. Vastano, "Determining Lyapunov exponents from a time series", Physica **16D**, 285 (1985).

VITA

Donald Allen Hirst [redacted]he son of Keene Harold Hirst and Frances Miranda Hirst. After completing his work at Colonial High School in Orlando, Florida in 1970, he entered the University of Central Florida in Orlando, Florida. He graduated with a B.S. in physics in 1973. He then attended the University of Georgia until April of 1978 when he went to work at Martin-Marietta Aerospace in Orlando, Florida as an electro-optics engineer. He joined the United States Air Force in October 1979 when he went to Officers Training School in San Antonio, Texas. He received a commission as a second lieutenant in the United States Air Force on 23 January 1980. Employed as a physicist at the Atmospheric Electromagnetic Hazards Group of the Air Force Wright Aeronautical Laboratory at Wright-Patterson Air Force Base, Ohio, he found time to finish his masters and graduated from the University of Georgia with an M.S. in physics. The title of his thesis was "Resonant Raman Scattering in 1,4 Dibromonaphthalene". In August 1983 he entered the Graduate School of The University of Texas at Austin. He was then assigned to the Geophysics Research Division of the Air Force Technical Application Center at Patrick Air Force Base in Florida in January 1987.

[redacted]

This dissertation was typed by Donald A. Hirst